Pinning Effekte
kolumnarer Schwerionenspuren
in
Kuprat-Supraleiter Dünnschichten

Dissertation
zur Erlangung des Grades
Doktor der Naturwissenschaften (Dr. rer. nat.)
am Fachbereich Physik
der Johannes Gutenberg-Universität Mainz

von
Michael Basset
geb. in Nastätten

universität⊗ mainz

Mainz, 2001
D 77

Gutachter:
Zweit-Gutachter:

Tag der mündlichen Prüfung: 07.12.2001

Pinning Effects
of
Columnar Heavy Ion Tracks
in
Cuprate Superconductor Thin Films

Ph.D. thesis
by
Michael Basset

uniuer
sität⊗
mainz

Mainz, Germany 2001

Für Margot, Uli und Judith

Contents

List of Figures

List of Tables

Introduction

Many results in the field of solid state physics have shown that it is not always the perfectness that makes it interesting to study the physical properties of a material. Distortions of the intrinsic structure yield strain effects, supplementary scattering mechanisms of conduction electrons, magnetic domain wall effects or other very interesting physical phenomena. Effects of disorder appear to be particularly acute in the oxidic compounds of high-temperature superconductors (HTSCs). After the discovery of this class of material in 1986 [1], many other HTSC compounds – of which $YBa_2Cu_3O_{7-x}$ [2] and $Bi_2Sr_2Ca_{n-1}Cu_nO_{2n+4}$ with $n = 1, 2, 3$ [3] are the most studied systems – have been found and show a common feature. Magnetic flux lines (or vortices) tend to be pinned by defects where the superconducting order parameter is locally suppressed. Independent from their individual properties, different defect structures reduce the dissipative motion of flux lines in the presence of external driving forces yielding a rich structure of the (H, T)-phase diagram. Due to the interaction between vortices and defects the periodic arrangement of the flux lines is disturbed and long range correlations of the vortex lattice are lost. The transition from a flux liquid at high temperatures to a collectively pinned vortex-glass or vortex-solid can be described by a continuous phase transition that is predicted within the framework of the vortex-glass model [4,5]. This ansatz is based on universal scaling arguments that describe the critical behavior of length and time scales in the presence of randomly distributed point disorder.

Pinning properties can be optimized by introducing artificial defects that trap the individual vortex lines all along their linear dimensions while simultaneously destroying a minimal volume fraction of the superconducting material itself. This is recently realized by the creation of antidots using electron beam lithography in order to study vortex dynamics and matching effects under the influence of regular arrays of artificial defects [6]. From the technological point of view the generation of heavy ion induced columnar defects is the most effective method to achieve this aim. This correlated disorder generates large increases in the critical current densities and an expansion of the irreversibility regime [7]. Columnar tracks also represent a sensitive probe for the intrinsic structure of the flux lines [8,9]. While vortices in $YBa_2Cu_3O_{7-x}$ show a three dimensional and linelike

1

behavior resulting in a confinement of the flux lines along the columnar defects, the higher anisotropy in $Bi_2Sr_2CaCu_2O_{8+\delta}$ yields a two dimensional character. In this case the flux lines break up into aligned pancake vortices [10] coupled by electromagnetic interaction and the Josephson-effect.

Compared to point disorder, the dynamics of flux lines pinned by columnar defects can be mapped onto the problem of bosonic particles in two dimensions [11]. This mapping predicts a low temperature Bose-glass phase, with vortices localized on columnar pins, separated by a sharp transition from an entangled liquid of delocalized lines. As in the case of the vortex-glass ansatz this phase transition can be described in terms of scaling relations. A scaling analysis of experimentally obtained current-voltage characteristics is often used to extract the critical exponents of this phase transitions.

Aim of the present work was the investigation of the columnar heavy ion track induced collective pinning mechanisms in HTSC thin films with the use of electronic transport measurements. Based on previous results on unirradiated samples revealing a lack of universality if the probed measurement window is expanded [12], Bose-glass scaling analysis of the current-voltage characteristics were carried out for $YBa_2Cu_3O_{7-x}$ thin films containing different densities of columnar defects. A systematic analysis of the dependencies of the critical exponents on external magnetic field, temperature and the accessible measurement window was performed in order to verify the theoretical predictions as well as the universality of the critical behavior of the Bose-glass transition.

Apart from this fundamental investigations the dynamic behavior of flux lines in confined strong pinning environments was in the focus of interest. $YBa_2Cu_3O_{7-x}$ single crystals with unidirected twin boundaries represent such geometric arrangements where a nearly defect-free superconductor is disturbed by nearly equidistantly spaced parallel pinning planes. Studies of the flux line dynamics in such systems showed that the motion of vortices is directed along the twin planes. However, the existence of twin boundaries in HTSCs is limited to the $YBa_2Cu_3O_{7-x}$ system. A more general and much more flexible method to generate any confined strong pinning geometry is the introduction of columnar defects. Therefore, new irradiation techniques allowing to create irradiation patterns with sharp interfaces separating strong and weak pinning regions are introduced. For the interpretation of the experimental results the following central questions arise: How strong is the influence of of pinned vortices on the flux lines that are not affected by a correlated pinning potential, and what is the length scale of this vortex-vortex interaction? A model describing the hydrodynamical interaction between a Bose-glass and a vortex liquid [13] was applied in order to analyze the vortex dynamics in this geometric pinning arrangement. Inspired by the occurring correlations between pinned and free flux lines, measurements of the electric field profile in a

weak pinning channel embedded in a strong pinning environment were realized for the first time. Such experiments allow to estimate the length scale of vortex-vortex interactions.

The first chapter of this work gives a comprehensive summary of the theoretical basis of the Bose-glass model. It points out the role of disorder in general and the influence of correlated disorder in particular. The introduction of the vortex-glass model is followed by a detailed discussion of the Bose-glass theory, including various creep mechanisms in the presence of columnar defects.

Sample preparation as well as the heavy ion irradiation process are described in chapter 2. In addition to the thin film deposition, the characterization and the photolithographic preparation of the measurement structures are briefly discussed. The creation of columnar defects is subjected to some requirements for the projectile ions that generate the defects as well as for the target material. These conditions and the experimental set up of the beamlines used for the heavy ion irradiation are illustrated.

Experimental results for $YBa_2Cu_3O_{7-x}$ thin films obtained with long measurement bridges are analyzed in a first part which consists of the third chapter. After a short introduction of the experimental methods and the sample preparation, the effects of columnar defects on the superconducting properties are discussed. The central point of this chapter consists of the analysis of the current-voltage characteristics within the framework of the Bose-glass model. Supplementary to a detailed scaling analysis the current dependence of the activation energy gives information about the different mechanisms of vortex dynamics in the irradiated sample. From the sum of these results one can draw conclusions about the existence of the Bose-glass transition.

Vortex dynamics in confined geometries form the second part of this work. Chapter 4 concentrates on experiments on Hall-structures that are irradiated with a lateral periodic resolution. Investigations of the anisotropic transport properties of these structures were performed and compared with similar experiments carried out on $YBa_2Cu_3O_{7-x}$ single crystals with unidirected twins. The use of two additional test bridges allowed to determine in parallel the resistivities of the irradiated and unirradiated parts as well as the respective current-voltage characteristics. These measurements provided the input parameters for numerical simulations of the electric potential distribution within the Hall-structure. The experimental results were interpreted in the framework of a hydrodynamical interaction between a Bose-glass phase and a vortex liquid.

Chapter 5 describes the first experimental realization of a Bose-glass contact. In this geometry a single weak pinning channel is sandwiched between two strong pinning environments. The local variation of the electric field in the vicinity of the interface between strong and weak pinning regions is a measure for the strength of

the interaction between pinned and free flux lines. The required complex sample preparation as well as first results on $Bi_2Sr_2CaCu_2O_{8+\delta}$ thin films are described in order to point out the perspectives of this new generation of experiments.

Another effect of heavy ion irradiation will be discussed in the sixth and last chapter. The existence of a flux flow instability in HTSCs at high current densities could be shown. In $YBa_2Cu_3O_{7-x}$this phenomenon reveals a clear correlation to the low dissipative vortex-glass phase. In addition, the question of quasiparticle heating is closely connected to the vortex instability. For this reason the heat propagation properties in the normal state of pristine and irradiated $YBa_2Cu_3O_{7-x}$ thin films are investigated. It is shown that columnar defects influence this non-superconducting properties which is important in the context of the vortex instability.

The various experiments presented in this work demonstrate that the use of heavy ion induced columnar defects is a very powerful tool for the investigation of vortex dynamics in HTSCs. Especially with regard to the recently discovered new superconductor MgB_2 [14], the use of correlated defects in the way exerted here is a helpful medium for a better understanding of the vortex dynamics in these materials and to investigate positional and orientational correlations as well as the nature of phase transitions.

Chapter 1

Correlated Disorder

The characteristic property of type-II superconductors is that an externally applied magnetic field H can partially penetrate into the material in form of magnetic flux lines or vortices, each carrying a magnetic flux quantum

$$\Phi_0 = \frac{h}{2e} = 2.07 \cdot 10^{-15} \text{ Tm}^2 \,, \tag{1.1}$$

provided that $H_{c1} < H < H_{c2}$. Supercurrents concentrate the magnetic flux towards the centers of the vortex cores where the superconducting order parameter Ψ is locally suppressed. The structure of a vortex is described in detail in Ref. [15].

When an external current density $\mathbf{J}$ is applied to an array of many flux lines, the vortices start to move under the action of a Lorentz-force density

$$\mathbf{f}_L = \mathbf{J} \times \mathbf{B} \,, \tag{1.2}$$

or the Lorentz-force per unit length for a single vortex $\mathbf{f}_L = \Phi_0 \mathbf{J} \times \mathbf{n}$, with $\mathbf{n}$ denoting the unit vector along the flux line. Within a perfectly homogeneous system this driving Lorentz-force is only counteracted by a viscous force $\mathbf{f}_\eta = -\eta \mathbf{v}$ with the viscous drag coefficient η resulting in a steady state velocity $\mathbf{v} = \mathbf{J} \times \mathbf{B} / \eta$. The dissipation leads to the appearance of a finite electric field $\mathbf{E}$ as a consequence of the vortex motion, $\mathbf{E} = \mathbf{B} \times \mathbf{v}$. Since both $\mathbf{J}$ and $\mathbf{E}$ run parallel, the power $P = (\mathbf{J} \times \mathbf{B})^2 / \eta$ is dissipated in the sample and the superconducting property of dissipation free current flow is lost.

In order to recover this property, the flux lines have to be pinned such that the vortex velocity disappears in spite of $\mathbf{F}_L \neq 0$. In this case the driving Lorentz-force is counteracted by a pinning force $\mathbf{F}_{\text{pin}}$.

1.1 Defects in Superconducting Systems

From these considerations it is obvious that the dynamics of flux lines in type-II superconductors is closely connected to the characteristics of the pinning force. The "required" pinning potentials are generated by different kinds of disorder and will be discussed in the following.

Atomic defects, in particular oxygen vacancies and structural point defects represent the family of uncorrelated defects. This **random point disorder**[1] defines the static properties of the vortex system. The long range ordered triangular vortex lattice is destroyed due to this random collection of pinning sites which can be described within the framework of the collective pinning theory [16]. Flux lines tend to move towards pinning sites to take advantage of the opportunity to lower their energy, but at the expense of increasing the elastic energy of the flux-line lattice (FLL) by deforming it. This competition between elastic energy $\mathcal{E}_{el}$ and pinning energy $\mathcal{E}_{pin}$ leads to an equilibrium flux-line configuration that can be described in terms of a correlation volume V_c within which the FLL is topologically inert.

But beside random point disorder two other kinds of disorder can be distinguished. **Thermal fluctuations** are the most obvious types of disorder that affect the dynamic properties. Vortices can perform thermally activated motions [17,18] or the vortex-solid can be transformed in a vortex liquid phase due to large thermal fluctuations. **Quantum fluctuations** are very similar to their thermal counterpart. They can affect superconductivity via fluctuations of the magnitude of the order parameter as well as its phase. These fluctuations induce a quantum motion of vortices (quantum creep).

However, the collective pinning theory does not take explicitly into account the interplay between randomly distributed point disorder and thermal fluctuations. Especially in case of HTSCs which are characterized by a transition into the superconducting state at relatively high temperatures, the pinned flux lines are subjected to strong thermal fluctuations yielding excitations of the vortices out of their pinning sites. Therefore the classical Anderson-Kim flux-creep picture in which the current dependence of the activation energy U near the critical current density J_c is generally described by $U(J) = U_0 \left[1 - (J/J_c)\right]^\alpha$, with $\alpha \leq 1$, must be modified. If thermal fluctuations are included in the energy balance between $\mathcal{E}_{el}$ and $\mathcal{E}_{pin}$ established above in the context of the theory of collective pinning, it turns out that its pinning barriers diverge as $U(J) \approx U_0 (J_c/J)^\mu$ in the limit of a

---

[1]In literature, the family of these defects is often named *quenched disorder*. But in this work one has to distinguish between uncorrelated, randomly distributed point defects and correlated defects (e.g. columnar defects). Both forms of defects represent configurations of quenched disorder in HTSC with noticeable differences in their pinning properties. Therefore it is necessary to avoid the term *quenched* in this context.
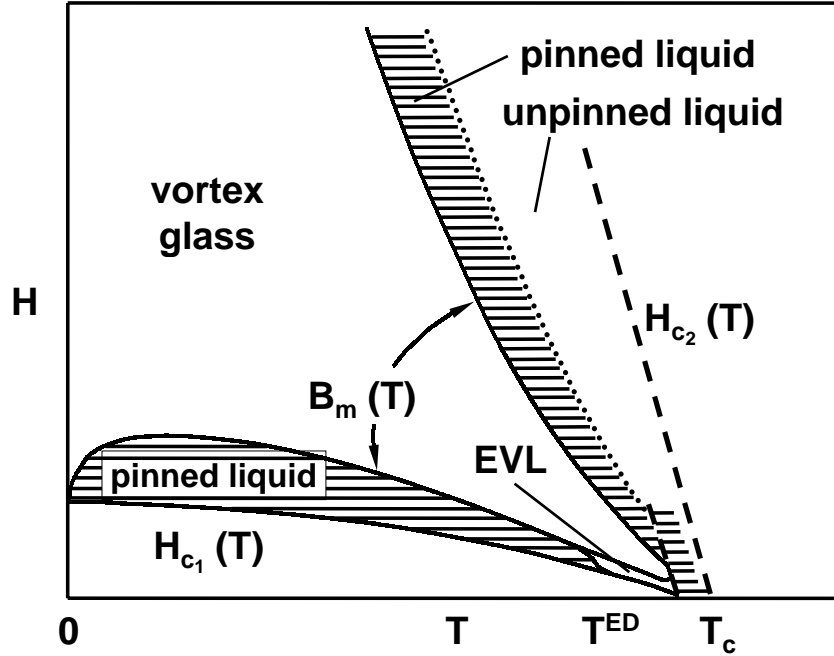
Figure 1.1: *Schematic representation of the (H, T)-phase diagram including effects of thermal fluctuations and pinning taken from [19].*

vanishing current density [15,19]. For temperatures below the transition temperature[2] T_m the vortex system is then in a vortex-glass phase that is characterized by a vanishing linear resistance

$$E \propto \exp\left[-\frac{U_0}{k_B T}\left(\frac{J_c}{J}\right)^{\mu}\right],\tag{1.3}$$

with the barrier height U_0 and the glassy exponent $\mu \leq 1$.

Thus the dynamics of vortices is drastically changed in the presence of randomly distributed point disorder and thermal fluctuations. As can be schematically seen in Fig. 1.1, the standard (H, T)-phase diagram of type-II superconductors changes in this case. The vortex lattice is replaced by a vortex-glass which is a true superconductor with $\rho(J \to 0) \to 0$. The melting line $B_m(T)$ defines the transition to the vortex liquid where two phases can be distinguished. The unpinned liquid corresponds to a flux-flow regime where the barriers are small and do not affect the vortex motion. For larger pinning barriers a thermally activated flux-flow (TAFF) regime is established [20]. This pinned vortex liquid occurs for temperatures above the melting line $(T > T_m)$ and indicates the high-

---

[2]The notation T_m is based on the fact that the vortex lattice in homogeneous superconductors melts into a vortex liquid at the melting temperature T_m. In the presence of random point disorder the vortex lattice is replaced by the vortex glass phase with an appropriate transition temperature T_m or T_G.

temperature region of the current-voltage characteristics (CVCs) that are used for the glass scaling analysis described below.

Another regime in the phase diagram of Fig. 1.1 is very interesting to mention. At low fields and low temperatures, respectively, a reentrant behavior from vortex-glass to a pinned liquid is sketched. As a consequence of decreasing field, the distance between vortices α_0 increases and eventually grows beyond the London penetration depth λ. In this region the vortex-vortex interaction is exponentially small and in consequence the shear modulus decays rapidly as $c_{66} \propto \exp(-\alpha_0/\lambda)$ leading to a loss of collective effects. Close to T_c an unpinned entangled vortex liquid (EVL) appears. Note that the width of this liquid phase is extremely narrow and that the importance of thermal fluctuations is strongly suppressed near H_{c_1}.

The main features of the disorder induced transition into a vortex-glass phase are briefly discussed in the next section. A more detailed discussion of the vortex-glass model, the appropriate scaling analysis as well as the respective experiments can be found in many publications (e.g. [19,21]). Based on the vortex-glass-model it is then possible to describe the influence of correlated disorder that has much stronger pinning properties than random point disorder.

1.2   The Vortex-Glass Model

The influence of random point disorder and thermal fluctuations on the vortex dynamics in type-II superconductors can be discussed within the framework of the vortex-glass model proposed by Fisher, Fisher and Huse (FFH) [4,5]. Following their ideas, the "true" superconductor is realized only in the vortex-glass phase because the high barriers of point disorder enable a dissipation-free transport of charge. Another question arising from the existence of this phase is if there is a well defined temperature describing the phase transition from vortex-glass to vortex liquid.
In analogy to the well understood magnetic order that occurs in spin-glasses [22], FFH made an ansatz to describe the response of the vortex system as a second order phase transition with scaling properties in the vicinity of the glass transition temperature T_{VG}. The static and dynamic features can be expressed in terms of a vortex-glass correlation length ξ and a relaxation time τ_{VG}. Both quantities diverge at T_{VG} as

$$\xi \sim |T - T_{\mathrm{VG}}|^{-\nu} \tag{1.4}$$

and

$$\tau_{\mathrm{VG}} \sim \xi^z, \tag{1.5}$$

with the universal static and dynamic critical exponents[3] ν and z, respectively.

A better understanding of the dynamic behavior of the vortex system in the vicinity of this transition is obtained considering the following three cases:

Above T_{VG} the system is expected to be in the liquid state. In the presence of currents, vortex motion is observed on short time scales because flux lines move with relatively high velocities. However, a small portion of the vortex system is already in the critical state that is described by diverging ξ and τ_{VG}. These regions show a slower dynamics compared to those in the liquid state.

At the transition temperature the extension of this critical region is infinite. The whole system is in this critical state of intermediate dynamical behavior.

Below T_{VG} the averaged motion occurs on a long time scale. A vortex-glass is established over large length scales whereas the system is still in the critical state with a faster dynamical behavior at small scales.

The dynamic properties of the vortex system are sketched schematically in terms of the nonlinear CVCs in the vicinity of the vortex-glass transition in Fig. 1.2.

Experimentally determined CVCs are used to perform a scaling analysis within the framework of the vortex-glass ansatz. Electric field and current density should scale as $E \propto 1/(\mathrm{length} \times \mathrm{time})$ and $J \propto 1/(\mathrm{length})^{D-1}$, where D is the spatial dimension. These assumptions yield a scaling function of the nonlinear conductivity [23]

$$E(J) \approx J\xi^{D-2-z}\mathcal{E}_\pm(J\xi^{D-1}\phi_0/k_B T). \tag{1.6}$$

In a scaled E-J representation all isotherms of the CVCs will collapse onto two branches that are separated by the transition temperature T_{VG}, if the critical exponents z and ν are appropriate. Early experiments on laser ablated epitaxial YBa$_2$Cu$_3$O$_{7-\mathrm{x}}$ thin films [24] give hints for the existence of a transition into a vortex-glass phase. This transition is continuous and the critical exponents determined from this experiment are $z \approx 4.8$ and $\nu \approx 1.7$.

A summary of various vortex-glass-scaling experiments based on electric transport measurements [25] seems to prove existence of a vortex-glass phase, but experiments carried out on microtwinned YBa$_2$Cu$_3$O$_{7-\mathrm{x}}$ single crystals using SQUID picovoltometry [26] show first limits of the universality of the underlying ansatz. In both types of experiment a characteristic length scale over which the current affects thermal distributions can be extracted from the crossover cur-

---

[3]In order to avoid confusions, ξ denotes the correlation length in vortex-glass case, whereas the correlation lengths for the Bose-glass transition are symbolized with $l_\perp$ and $l_\parallel$ respectively. Other quantities like transition temperature or relaxation time are indicated with VG (vortex-glass) or BG (Bose-glass) respectively.
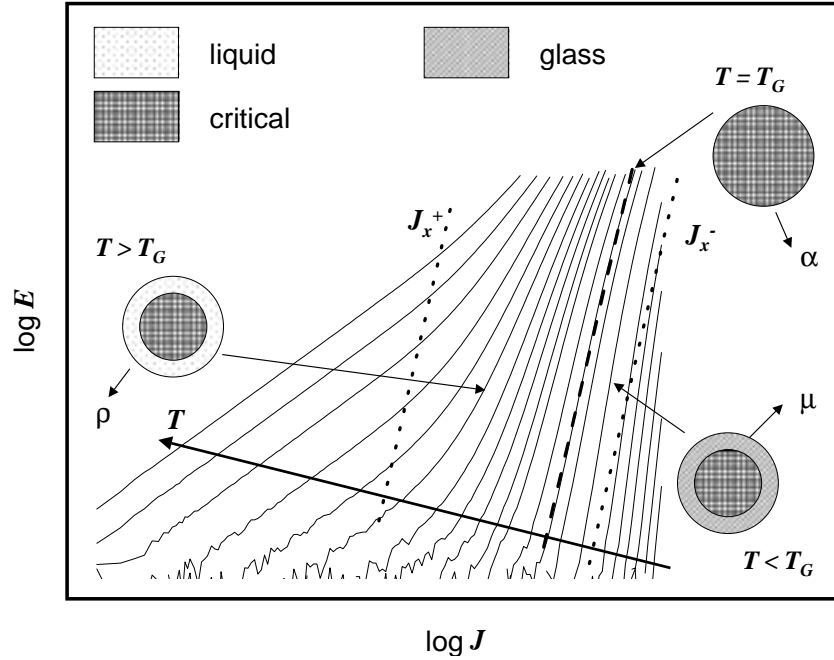
Figure 1.2:   *Interpretation of measured CVCs within the framework of the glass model, taking thermal as well as random point disorder into account. The plot schematically contains all the relevant information on the dynamic response of the vortex system, e.g. the vortex-glass scaling laws for $E(J)$, the resistivity $\rho(T)$, the crossover current densities $J_x^{\pm}(T)$ (see section 1.3), as well as the vortex-glass exponent μ. At the vortex-glass transition temperature T_{VG} the characteristic is algebraic, $E \propto J^{\alpha}$, with $\alpha = (z+1)/(D-1)$. Above T_{VG} the system is a liquid over large distances, with $\rho \propto (T - T_{\mathrm{VG}})^{\nu(z+2-D)}$, and critical at small distances. Below T_{VG} a glassy response at large distances, $E \propto \exp[-(J_c/J)^{\mu}]$, and again a critical behavior at small distances is observed.*

rent density[4]. In the latter case this length scale differs by more than one order of magnitude from the results obtained with electric transport measurements on thin films. Three possible explanations are given in this context: a worse accuracy in the scaling analysis near the linear response regime, a different scaling function for crystals as opposed to films, or a failure of the vortex-glass hypothesis. Another important question arising from the E-J scaling analysis is the influence of the range that can be probed by the different experiments [27]. Voss-de Haan *et al.* [12] showed that the critical scaling depends on the electric field range in $YBa_2Cu_3O_{7-x}$ thin films. A high value of the dynamic exponent ($z \geq 9$) was observed which drastically decreased if the scaled electric field range is reduced. The same work confirmed this unexpected result by other analyzing methods. Thus, it remains an open question to prove unambiguously the existence of the

---

[4]The crossover current density $J_x^{\pm}$ will be discussed in detail within the context of the Bose-glass scaling ansatz in section 1.3.4

vortex-glass phase transition. Other criteria in order to enhance the significance of the scaling analysis [28] and other methods are necessary to solve this problem.

These facts raise doubts about the vortex-glass model introduced by FFH and to point out alternative models that can describe the CVCs illustrated in Fig. 1.2. A model combining thermally activated motion of flux lines, viscous flow at high current densities and a distribution of activation energies can reproduce the characteristic features of the CVCs [29]. Another approach [30] describes the nonlinearities of the CVCs within the framework of the flux creep model assuming a nonlinear current dependence of the activation energy. Finally the approach used by Jensen and Minnhagen [31] interprets the CVCs in terms of thermally activated vortex unbinding.

Up to now only the effects of uncorrelated point disorder were discussed. Additional effects appear if the defects are correlated as in the case of columnar defects. This will be discussed in the following.

1.3   The Bose-Glass Model

Collective pinning mechanisms and their influence on the dynamics of vortices as discussed in the previous section change strongly if correlated disorder is taken into account. Due to a coherent superposition of pinning centers the pinning force density $\mathbf{f}_{\text{Pin}}$ is remarkably amplified in this case. While uncorrelated point-like defects only act on a small volume of a flux line, correlated disorder pins a vortex more effectively over an extended length scale, provided that flux lines and columnar defects are aligned.

After the introduction of the main types of correlated disorder, the discussion concentrates on the Bose-glass model in this section. The key ideas of the concept introduced by Nelson and Vinokur [11,32,33] are illustrated and the glass scaling analysis is explicitly explained. In addition, the relevant behavior of the activation energy is discussed. A comparison between vortex-glass and Bose-glass model will conclude this section.

1.3.1   Types of Correlated Disorder

There are different types of correlated disorder occurring in HTSC systems. In $YBa_2Cu_3O_{7-x}$, twin boundaries form one class of correlated defects. The influence of these two-dimensional twinning planes will be mentioned in chapter 4. Screw dislocations produced in thin films during growth [34] are a second type of correlated pinning centers. In contrast to these growth induced defects, this work deals with artificially introduced heavy ion induced columnar defects which represent the third family of correlated disorder. They show the most effective pinning properties and are also technologically relevant. Linear tracks of damaged

material [35] then introduce strongly correlated disorder into HTSC systems. At low magnetic fields such that the intervortex distance

$$a_0 \equiv \sqrt{\frac{\Phi_0}{B}} = \frac{450}{\sqrt{B \ [\text{T}]}} \ \text{Å} \tag{1.7}$$

is much larger than the mean distance d_r between the tracks, each vortex is individually pinned by one columnar defect. The localization of the vortices is repealed with increasing temperature due to a delocalization induced by thermal fluctuations.

1.3.2   Basic Assumptions

Inspired by the vortex-glass scenario of FFH, Nelson and Vinokur proposed a theory known as the Bose-glass model [11,32,33]. For a magnetic field aligned parallel to the correlated defects the flux lines will be attracted by these defects. Given a sufficient thermal energy, vortices move from one columnar pin to another in an unconfined diffusive path, allowing them to respond to the Lorentz-force induced by external currents, giving linear resistance. At low temperatures all flux lines are localized in the vicinity of a few columnar defects (cf. Fig. 1.3) and the vortex system is in the Bose-glass phase. The linear resistance in this state is zero.

The model starts with the classical free energy F_N for N fluxons in a sample of thickness L, defined by their trajectories $\{\mathbf{r}_j(z)\}$ as they traverse a sample with columnar pins and magnetic field both oriented along the z axis that is perpendicular to the CuO_2 planes,

$$
\begin{aligned}
F_N &= \frac{1}{2} \tilde{\epsilon}_1 \sum_{j=1}^{N} \int_0^L \left| \frac{d\mathbf{r}_j(z)}{dz} \right|^2 dz \\
&+ \frac{1}{2} \sum_{i \neq j} \int_0^L V(|\mathbf{r}_i(z) - \mathbf{r}_j(z)|) dz \\
&+ \sum_i \int_0^L V_D(\mathbf{r}_i(z)) dz.
\end{aligned}
\tag{1.8}
$$

This free energy contains three terms, each integrated over the fluxon length. The first term represents the increase of elastic energy, where $\tilde{\epsilon}_1$ is the local tilt modulus. The interaction between vortices is described using the interaction potential $V(|\mathbf{r}_i(z) - \mathbf{r}_j(z)|)$ in the second term. Finally, the third term contains an expression for a pinning potential $V_D(\mathbf{r}(z))$. It is modeled by a random array of identical cylindrical traps of average spacing d_r, effective radius

$$b_0 = \max(r_r, \sqrt{2}\,\xi_{ab}), \tag{1.9}$$

and a potential-well depth ϵ_r. Here r_r is the radius of the columnar pins and ξ_{ab} is the superconducting coherence length in the ab plane.

Analogy to 2D bosons

Using the formal correspondence between the partition functions of a system of directed lines and a system of two-dimensional Bose particles in the Feynman path representation [36,37], one can replace z by an imaginary time so that the first term of 1.8 becomes a kinetic-energy term, the interaction term represents a time dependent interaction between particles in the xy plane and the third remains an attractive potential energy centered on the position of the defects in the xy plane. Thus the classical statistical mechanics of the flux lines in three dimensions is equivalent to the quantum mechanics of interacting bosons in two dimensions with a random static potential $V_D(\mathbf{r})$.

With the use of this mapping formalism one can distinguish three characteristic vortex phases. At high temperatures an entangled flux liquid is found. In this phase the vortices are delocalized and able to hop freely from one columnar defect to another as they cross the sample. The diffusion of the flux lines is described via a large-scale diffusion constant $D_R \propto T$.

Lowering the temperature leads to a sharp phase transition into the Bose-glass phase at T_{BG}. Each vortex is localized at one or more columnar pins. This phase is characterized by an infinite tilt modulus c_{44}, since the correlated disorder keeps localized vortices from following a tilt in the external field. Additionally the phase is stable over a finite range of tipping angles away from the direction parallel to the correlated defects. Delocalization occurs for vortex densities and temperatures for which the localization tubes shown in Fig. 1.3 overlap for neighboring flux lines. When T_{BG} is approached, the localization length $l_\perp$ diverges as

$$l_\perp \sim |T - T_{\mathrm{BG}}|^{-\nu_\perp}, \tag{1.10}$$

with the critical exponent $\nu_\perp \geq 1$ [38]. As sketched in Fig. 1.3(a) there also exists a correlation length along the, z axis,

$$l_\parallel = l_\perp^2 / D_0, \tag{1.11}$$

which is the distance along z it takes a flux line to diffuse across a tube of diameter of the localization length. The diffusion constant D_0 is valid only for short
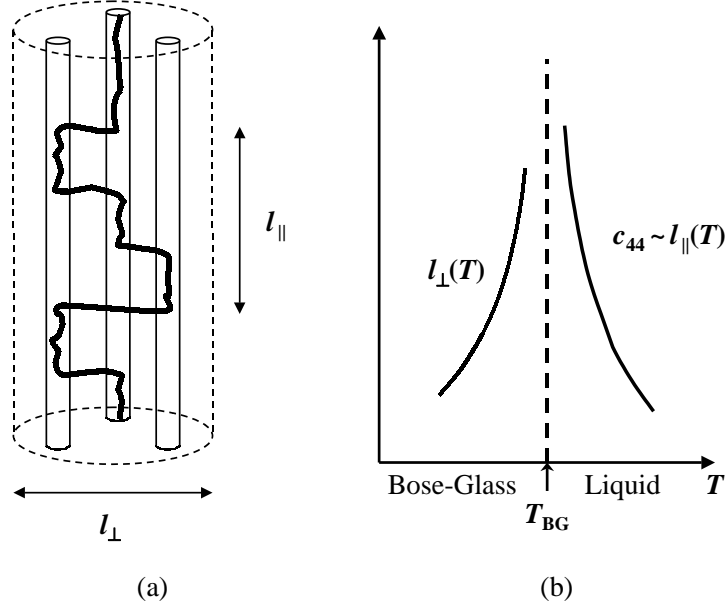
Figure 1.3:   *Length scales near the Bose-glass transition. (a) Flux-line (black line) wandering in a tube of size $l_\perp(T)$ containing several columnar defects (aligned tubes). The parallel correlation length $l_\parallel$ is the distance along z it takes a flux line to diffuse across a tube of diameter of the localization length $l_\parallel$. (b) Divergence of the characteristic length scales and the tilt modulus at T_{BG} [32].*

distances. The diffusion on large scales D_R vanishes in the glass phase. The simplest scaling hypothesis is that D_0 remains finite at T_{BG}, so that

$$l_\parallel \sim |T - T_{\mathrm{BG}}|^{-\nu_\parallel} \tag{1.12}$$

with $\nu_\parallel = 2\nu_\perp \equiv 2\nu'$.

   Finally the theory also predicts a Mott insulator phase at low temperatures. In this phase the vortex density matches exactly the density of columnar defects. The flux lines are again localized due to the pinning potentials as well as due to interactions with neighboring lines. As a result the magnetic field is locked at the *matching field* $B = B_\phi \equiv n_{\mathrm{CD}}\phi_0$ over a range of external magnetic inductions H within this phase. Here, n_{CD} is the areal density of columnar defects and ϕ_0 is the elementary flux quantum described by Eq. (1.1). Flux motion in this regime is highly nonlinear and resembles transport in the Meissner phase. Another important feature of this phase is that both, the tilt modulus c_{44} and the compression modulus c_{11} are infinite. However, it is difficult to access this phase experimentally due to extremely long relaxation times.

The three vortex phases arising from the introduction of correlated disorder are
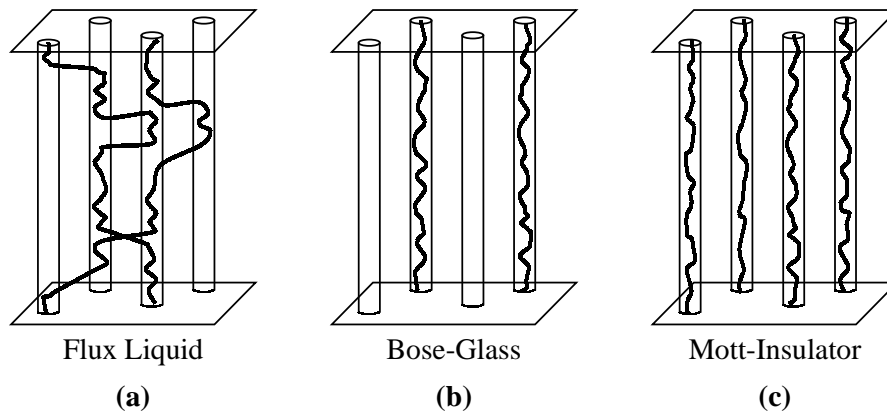
Figure 1.4: *Schematic illustration of flux lines attracted by columnar defects in the (a) flux liquid, (b) Bose-glass, and (c) Mott insulator phases [11].*

schematically illustrated in Fig. 1.4.

Beside these consequences for the (H, T)-phase diagram the analogy to 2D bosons is very helpful for the description of the physics of flux lines in the vicinity of columnar pins. If a single vortex is considered near a single defect, the problem can be transferred to a quantum particle in a cylindrical potential. The localization length $l_\perp$ is like the Bohr radius of an isolated "atom" consisting of one columnar defect and one flux line. An analogue to the H_2^+ molecule emerges if the case of a vortex line able to hop between two columnar pins is treated [32]. In the presence of many columnar defects a tight binding model can be applied. The vortices are allowed to hop between a randomly distributed array of defect sites with the constraint that each fluxon has to spend most of that time in the vicinity of the pinning site. Table 1.1 shows how the quantities must be translated in order to map the vortex problem to the 2D-boson analogy.

Table 1.1: *Boson analogy applied to vortex transport. The term ϵ_0 in the pair potential is the contribution to the pinning potential revealing from neighboring vortices. K_0 represents the zeroth-order Hankel function of imaginary argument. Table taken from [32].*

Charged				Pair		Electric	
bosons	Mass	$\hbar$	$\beta\hbar$	potential	Charge	field	Current
Vortices	$\tilde{\epsilon}_1$	$k_B T$	L	$2\epsilon_0 K_0(r/\lambda_{ab})$	ϕ_0	$\hat{\mathbf{z}} \times \mathbf{J}$	E

The vortex dynamics of the Bose-glass at low temperatures can be described within the framework of this mapping procedure. Applying an external current density $\mathbf{J}$ transverse to the field direction yields an additional Lorentz-term in the free energy of the vortex system described by Eq. (1.8)

$$\delta F_N = -\mathbf{f}_L \cdot \sum_{j=1}^{N} \int_0^L \mathbf{r}_j(z)dz, \tag{1.13}$$

with the Lorentz-force per unit length $\mathbf{f}_L = \phi_0 \mathbf{J} \times \hat{\mathbf{z}}$. This additional contribution enforces the vortex to leave locally the potential well over a finite segment. These vortex excitations in the limit of low current densities are typical for the Bose-glass as well as for the vortex-glass phase and are characterized through diverging barriers as $J \longrightarrow 0$, in contrast to above mentioned TAFF models.

1.3.3   Creep and Activation Energy

The Lorentz-force induced excitations of the flux lines in the presence of columnar defects are different, depending on the strength of $\mathbf{f}_L$ and thus on the current with respect to characteristic values. The dependences are of the form

$$J_i \approx U_0/\phi_0 d_i, \tag{1.14}$$

with the vortex binding energy per unit length U_0 and a characteristic length scale d_i depending on the excitation process. There are three main vortex loop excitations that describe the creep of a single vortex.

Vortex Loop Excitations - Single Vortex Creep

The first mechanism is the tunneling process via **half loops**. Therefore an intermediate current regime $J_1 < J < J_c$, with $d_1 = d$, the average spacing between unoccupied pins, and $d_c = b_0$ (cf. Eq. (1.9)), respectively is considered. In this current range adjacent columnar defects can be ignored and this case can be treated as the problem of a single vortex in a single columnar defect. Figure 1.5(a) illustrates how the flux line escapes from its position in form of a half-loop configuration. The electric field that is generated by this kind of tunneling is

$$E \approx \rho_0 J \exp\left[-\frac{\mathcal{E}_k}{k_B T}\left(\frac{J_1}{J}\right)\right], \tag{1.15}$$

with the energy $\mathcal{E}_k = \sqrt{\tilde{\epsilon}_1 U_0}d$. A similar result was found in other works [39].

The thermally activated **double kink** configuration appears for smaller current densities $J < J_1$. One segment of the vortex is thrown onto a neighboring columnar defect as shown in Fig. 1.5(b). This mechanism is described via a nearest neighbor hopping conductivity for thin samples

$$E \sim \rho_0 J e^{-c_1 \mathcal{E}_k/k_B T}, \tag{1.16}$$

with a constant c_1.

If this thin sample condition is abandoned another excitation describes the vortex dynamics for $J < J_1$. In this regime the dispersion in the pinning energies is important and the tunneling probability is optimized by forming **double-superkinks** that are extended over the next track as it is illustrated in Fig. 1.5(c). After the establishment of a superkink the vortex spreads to the optimal columnar defect that has a lower energy compared to the intercostal defects. In analogy to Mott variable-range hopping of electrons between localized states in semiconductors [40] one can express the non-ohmic CVCs as

$$E \approx \rho_0 J \exp\left[-\frac{\mathcal{E}_k}{k_B T}\left(\frac{J_0}{J}\right)^{1/3}\right], \tag{1.17}$$

with $J_0 \propto 1/d^3$, implying the optimal track distance for the formation of a superkink. The influence of vortex-vortex interactions is not yet taken into account. Doing this, again in analogy to the theory of variable range hopping, changes the exponent in Eq. (1.17) from $\mu = 1/3$ to a logarithmic behavior $\mu = 1$ for all length scales.
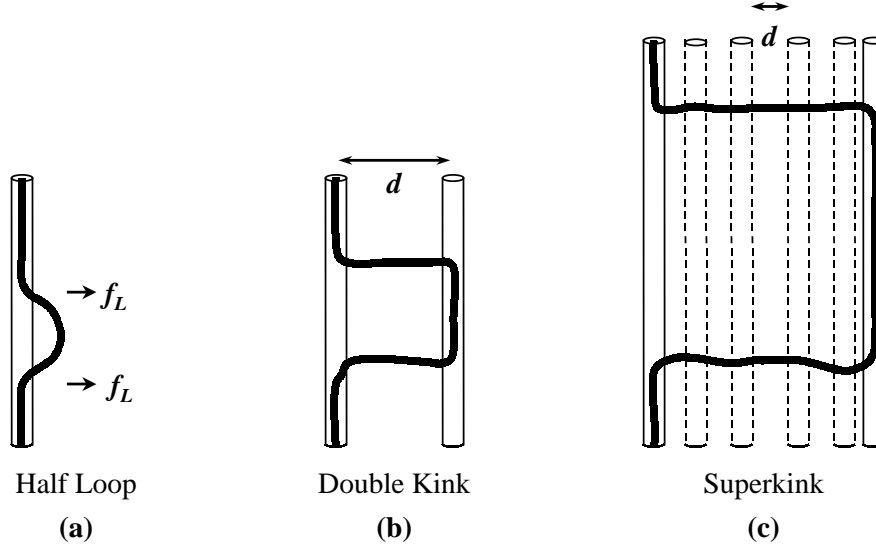
Figure 1.5: *Possible vortex excitations in the presence of columnar defects. (a) shows the half loop excitation and illustrates the Lorentz-force $\mathbf{f}_L$ that pushes the flux line out of the columnar pin. (b) shows a double kink excitation appearing in thin samples. The double-superkink configuration in (c) is required for a variable-range hopping. The vortex line segment is thrown onto the optimal low-energy pin [32]. Note that the the double kink mechanism is only valid in the thin film limit.*

Creep of Vortex Bundles

Apart from the mechanisms of single vortex creep due to loop excitations vortex bundles also show a dynamic behavior. Vortex-vortex interactions play a major role in the description of these mechanisms which implies that they are valid for higher vortex densities and thus higher magnetic fields compared to the precedent cases. Vortex bundles emerge for magnetic fields $B > B^*(T)$, where the characteristic field $B^*(T)$ indicates that the interactions must be taken into account [32]. A higher field implies that the intervortex distance a_0 decreases. The crossover from single vortex to vortex bundle dynamics is marked by the condition

$$L_z(J) = a_0, \tag{1.18}$$

where L_z is the characteristic length of the fluctuating vortex segment appearing in the single vortex creep process [19].

A vortex bundle is described by its extension along the z axis and the sizes in the direction of the bundle motion $R_\parallel$ and in the transverse direction $R_\perp > a_0$. These length scales are connected to the elastic properties of the vortex bundles which makes it difficult to describe the creep mechanisms in a simple way due to their nontrivial dispersive behavior [41]. References [19] and [32] give a compact overview of the different possible cases. The relevant CVCs or current dependencies of the activation energy will be pointed out below.

Two creep mechanisms are characteristic in the presence of columnar defects, acting on length scales in the order of the transverse bundle size $R_\perp$ in the limit of small current densities.

Plastic Creep
Unpinned vortices that are trapped *between* pinned vortices will move before the depinning of the pinned vortices occurs. The correlation between adjacent flux lines is lost and the vortex system is subjected to plastic deformations. The balance between the Lorentz-force and elastic forces of the unpinned flux lines defines the critical current for this creep mechanism for temperatures $T < T_1$. In this temperature regime the bundle motion is thermally activated and takes place via jumps over the plastic barriers U_{Pl}. The jumping distance is in the order of a_0 and is set by the distance of metastable states *between* the tracks. An estimation magnetic field dependence of the activation energy yields $U_{\text{Pl}} \propto B^{3/4}$.

Collective Creep
The above discussed mechanism of plastic creep is no longer valid if the transverse size of the vortex bundle exceeds the mean distance between tracks, e.g. $R_\perp > d_r$. In this collective creep regime the whole vortex bundle moves to the

next metastable state. This can again be understood as a hopping mechanism which depends on the applied current and selects the most favorable hopping distance and the optimal size of vortex bundles and therefore determines the creep activation energy. In contrast to the plastic creep mechanism, higher temperatures $(T > T_1)$ are required and the relevant balance of forces is established between the Lorentz-force and the deformation energy of the bundle in order to obtain the critical current. Again the quantum mechanical analogy is used to map the problem of classical creep in the presence of columnar defects onto the quantum mechanical tunneling of a 2D pancake vortex lattice through point disorder. The optimal jump for 2D creep can be obtained with the aid of scaling arguments leading to a general expression for the current dependence of the activation energy

$$U(J) \propto U_0(B^2) \left(\frac{J_b}{J}\right)^\mu, \tag{1.19}$$

where J_b is the bundle size related characteristic current density and the exponent $\mu = \mu(u, s)$ depends on the on the hopping distance u and the dispersion s of the elastic constants.

Beside this creep mechanisms on small length scales the vortex bundle motion on large scales is described in analogy to the variable range hopping transport as described in the picture of superkink excitations described by Eq. (1.17) in the limit $J \longrightarrow 0$.

1.3.4   Scaling Analysis

The transition into the Bose-glass phase is described by scaling laws that are similar to the relations presented in section 1.2. One basic assumption in this context is that the scaling behavior of the electric field E and the current density J is related to the critical properties of the "in-plane vector potential" near the transition $\mathbf{A}_\perp \sim 1/l \perp (T)$. Assuming that the relaxation time scales in analogy to Eq. (1.5) as

$$\tau_{\mathrm{BG}} \sim l_\perp^{z'}. \tag{1.20}$$

This leads to the scaling function

$$l_\perp^{z'+1} E \approx F_\pm(Jl_\parallel l_\perp \phi_0/k_B T). \tag{1.21}$$

Here, the $\pm$ subscripts distinguish the scaling function above and below T_{BG}. The argument $Jl_\parallel l_\perp \phi_0/k_B T$ is the work done by the Lorentz-force to move a critical

fluctuation (extending a distance $l_\parallel$ along the z-axis) a distance $l_\perp$ divided by the thermal energy $k_B T$. For $D = 3$ this can be converted in the same form as Eq. (1.6). Using Eq. (1.11), division by $l_\perp^3 J$ and defining a new scaling function $\mathcal{E}'_\pm$ yields

$$E(J) \approx J l_\perp^{2-z'} \mathcal{E}'_\pm (J l_\perp^3 \phi_0 / k_B T). \qquad (1.22)$$

The critical exponents for this Bose-glass scaling are estimated from numerical simulations [42–44] to be $\nu' \approx 1$ and $z' \approx (7 \pm 2)$.

Several properties of the CVCs that are characteristic for temperatures near the Bose-glass transition can be derived from these scaling laws. Above T_{BG} the resistivity vanishes as

$$\rho \propto (T - T_{\mathrm{BG}})^{\nu'(z'-2)} \qquad (1.23)$$

on approaching the transition temperature. At T_{BG} the Bose-glass correlation length $l_\perp$ grows to infinity. As E and J must have finite values, $l_\perp$ has to cancel out in Eq. (1.21) and the scaling function $\mathcal{E}'_\pm(x)$ should be proportional to x^α. At T_{BG}, the electric field thus depends on the current density according to a power law

$$E \propto J^\alpha = J^{(z'+1)/3}. \qquad (1.24)$$

Both regimes are illustrated in Fig. 1.2 where the characteristic features of the CVCs in the case of a vortex-glass transition are shown in a double-logarithmic plot. Even if there are differences in the physical interpretation of both glass phases, this schematic representation of the CVCs is also valid in the Bose-glass case.

The third property of the CVCs below the transition temperature has been already discussed. Equation (1.17) describes the nonlinear $E(J)$-behavior in the glass phase.

Scaling Analysis

The evaluation of experimentally obtained CVCs in the framework of the Bose-glass scaling theory requires some transformations of Eq. (1.22). Using the scaling law for $l_\perp$ described by Eq. (1.10), two scaled expressions for the electric field $(E/J)_{\mathrm{sc}}$ and current density J_{sc} are obtained.

$$\left(\frac{E}{J}\right)_{\text{sc}} \equiv \frac{E}{J} |T - T_{\text{BG}}|^{\nu'(2-z')} \tag{1.25}$$

and

$$J_{\text{sc}} \equiv \frac{J}{T} |T - T_{\text{BG}}|^{-3\nu'} . \tag{1.26}$$

Using these quantities with the appropriate exponents ν' and z', the CVCs for different temperatures at a fixed external magnetic field should collapse onto two branches that are separated by T_{BG}. The scaling procedure is identical to the scaling analysis in the case of a vortex-glass transition [24,12], even if there are physical and mathematical differences between both models. This point will be discussed below.

Other methods can be applied to determine the characteristic quantities of the Bose-glass transition. A Vogel-Fulcher analysis [45–48] can be carried out in order to test the scaling behavior of the resistivity above T_{BG}, but this method was not used in this work and is only mentioned for the sake of completeness. Based on the investigations of long measurement [21,12] bridges in $YBa_2Cu_3O_{7-x}$ thin films the critical exponents and the glass temperature can also be obtained using the method of *crossover current densities*. As illustrated in Fig. 1.2 the crossover current density $J_x^{\pm}$ separates the critical region at large current densities from the noncritical glassy (below T_{BG}, J_x^{-}) or the flux liquid (above T_{BG}, J_x^{+}) regime at low current densities

$$J_x^{\pm} \propto \left(l_{\perp} l_{\parallel}\right)^{-1} \propto |T - T_{\text{BG}}|^{3\nu'} . \tag{1.27}$$

With this relation it is possible to find an expression for the current dependence of the crossover field E_x^{+}. Using Eq. (1.23), one finds that

$$E_x^{+} \propto \left(J_x^{+}\right)^{(z'+1)/3} \propto \left(J_x^{+}\right)^{\alpha} , \tag{1.28}$$

which has the same $E(J)$-dependence as the CVC at T_{BG} and is thus parallel to the glass line. The slope $\alpha = (z' + 1)/3$ yields the dynamic exponent z' and facilitates the Bose-glass scaling analysis. However, it will be shown in chapter 3 that the latter method only can be applied if the CVCs are measured with a high electric field sensitivity.

1.3.5 Comparison of Models

The scaling hypothesis of the Bose-glass model in Eq. (1.22) shows a strong resemblance to the scaling properties in the vortex-glass case of Eq. (1.6). But

aside from this obvious mathematical analogy there are some physical differences between the two models that will be discussed in the following.

Physical Differences

The discussion of the physical differences between vortex-glass and Bose-glass is related to the properties of the defects. In the vortex-glass phase the flux lines are only marginally pinned in 3D. Thus, the competition between the uncorrelated pinning forces and the thermal fluctuations yield an exponential vanishing of the critical current density. On the other hand, correlated disorder competes more efficiently with thermal fluctuations, resulting in a weaker algebraic decay of the critical current density with increasing temperature. A further difference between uncorrelated and correlated disorder is that in the former case the statistical mechanics of the vortex is characterized by line wandering, whereas in the latter case the characteristic feature is localization. A consequence of this varying dynamic behavior is that the critical exponents characterizing the glass transition are different. Due to the much more pronounced localization in the presence of columnar defects the static critical behavior is weaker. The columnar track influences the flux line much stronger than a random disorder environment and thus the extension of the critical state diverges not as strong as in the vortex-glass case. The localization of vortices near a columnar defect is also responsible for the dynamic response of the vortex system. It happens much faster and therefore the Bose-glass relaxation time τ_{BG} diverges shorter time scales compared to τ_{VG}.

Another important difference between vortex-glass and Bose-glass is the response of the respective system to tilted magnetic fields. Except for anisotropic effects associated to the CuO_2 planes [49–52], the effect of point disorder should be independent of the angle between the applied magnetic field and the crystallographic orientation of the sample. In contrast to this behavior the correlated disorder of columnar defects will be turned off as the applied magnetic field is tilted away from the direction of the columnar tracks, which is in accordance with the predictions of the scaling theory [32]. With this assumption it should be possible to distinguish between the Bose-glass and a vortex-glass phase using angle dependent scaling analysis.

Mathematical Differences

Table 1.2 shows a comparison between both models for the 3-dimensional case from the mathematical point of view. The representation of the CVCs shown in Fig. 1.2 is valid for both models and differs only in the critical exponents. It is thus a universal illustration of the nonlinear behavior below, at and above the glass transition temperature T_G as well as of the crossover current densities that can also be described in both pictures. Two expressions that can be extracted by

Table 1.2: *Comparison between vortex-glass and Bose-glass scaling for $D = 3$ dimensions*

	Vortex-Glass	**Bose-Glass**
Scaling Function	$E(J) \approx J\xi^{1-z}\mathcal{E}_{\pm}(J\xi^2\phi_0/k_BT)$	$E(J) \approx Jl_{\perp}^{2-z'}\mathcal{E}'_{\pm}(Jl_{\perp}^3\phi_0/k_BT)$
CVCs $T > T_G$ $T = T_G$ $T < T_G$	$\rho \propto (T - T_{\mathrm{VG}})^{\nu(z-1)}$ $E \propto J^{\frac{z+1}{2}}$ $E \propto \exp\left[-\left(\frac{J_0}{J}\right)^{\mu}\right], \mu \leq 1$	$\rho \propto (T - T_{\mathrm{BG}})^{\nu'(z'-1)}$ $E \propto J^{\frac{z'+1}{3}}$ $E \propto \exp\left[-\left(\frac{J_0}{J}\right)^{\mu}\right], \mu = \frac{1}{3}, 1$
Scaled Quantities	$\left(\frac{E}{J}\right)_{\mathrm{sc}} \equiv \frac{E}{J}\,\lvert T - T_{\mathrm{VG}}\rvert^{\nu(1-z)}$ $J_{\mathrm{sc}} \equiv \frac{J}{T}\,\lvert T - T_{\mathrm{VG}}\rvert^{-2\nu}$	$\left(\frac{E}{J}\right)_{\mathrm{sc}} \equiv \frac{E}{J}\,\lvert T - T_{\mathrm{BG}}\rvert^{\nu'(2-z')}$ $J_{\mathrm{sc}} \equiv \frac{J}{T}\,\lvert T - T_{\mathrm{BG}}\rvert^{-3\nu'}$
Crossover Current	$J_x^{\pm} \propto \lvert T - T_{\mathrm{VG}}\rvert^{2\nu}$	$J_x^{\pm} \propto \lvert T - T_{\mathrm{BG}}\rvert^{3\nu'}$

comparing Eq. (1.6) and Eq. (1.22) show the mathematical relation between the dynamic and static critical exponents of both models.

$$\nu' = \frac{2}{3}\nu, \qquad (1.29)$$

and

$$z' = \frac{1}{2}(3z + 1). \qquad (1.30)$$

Using these relations it is possible to perform in parallel a Bose-glass and a vortex-glass scaling analysis. As will be shown below the vortex-glass scaling analysis is applicable for the CVCs of irradiated samples and magnetic fields exceeding the matching field $(B > B_\phi)$ determined by the irradiation dose.

1.4 Interface Effects

In the context of the Bose-glass transition it is interesting to ask which effects appear at an interface between strong correlated and weak uncorrelated pinning. Due to enhanced pinning forces in systems with correlated disorder, higher current densities, magnetic fields or temperatures are necessary to induce the glass
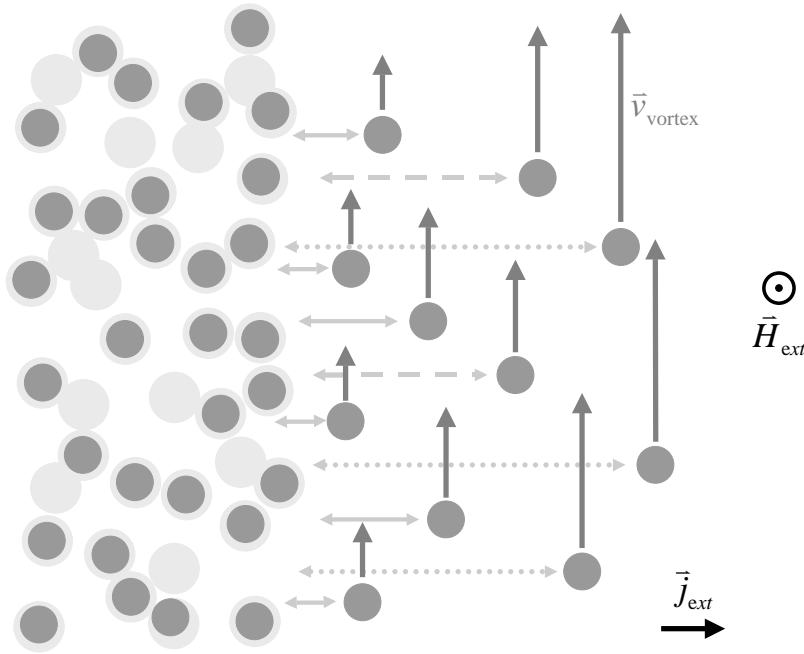
Figure 1.6:   *Vortex motion at interfaces between strong and weak pinning regions. The light gray circles represent the columnar defects, whereas the dark circles are flux lines. The interface between strong and weak pinning regions is assumed to be sharp and the motion of the unpinned vortices is strongly influenced by the pinned ones. The strength of this interaction is illustrated by horizontal arrows and decays with the distance. Thus, free vortices near the interface will execute a slower motion compared to flux lines further away from the interface. In this example the magnetic field is $B = 0.74B_\phi$.*

to liquid transition compared to systems containing only random point disorder. In consequence and as illustrated in Fig. 1.2, vortices in a strong pinning environment can be in the glass phase whereas simultaneously flux lines in weak pinning regions are still in a flux liquid phase. As schematically sketched in Fig. 1.6, the pinned vortices will interact with the "free" flux lines at such an interface yielding a decreased vortex velocity $\mathbf{v}_{vortex}$ near the interface. This can be interpreted as a freezing of weakly pinned flux lines due to vortex-vortex interactions. Experiments on $NbN : Nb_3Ge$ thin films [53] and $Bi_2Sr_2CaCu_2O_{8+\delta}$ single crystals [54] with periodic arrays of strong and weak pinning channels have shown that the freezing of the vortex lattice is indeed induced by the strong pinning regions.

In contrast to periodic arrangements the case of only one weak pinning channel sandwiched between two strong pinning regions is theoretically discussed and linked to the Bose-glass transition [13,55]. This hydrodynamic approach describes the viscous flow of the vortex liquid in the weak pinning channel near T_{BG}. In this *Bose-glass contact* geometry the vortex flow shows a velocity profile. The induced electric field depends on the viscous length δ, channel width L, current
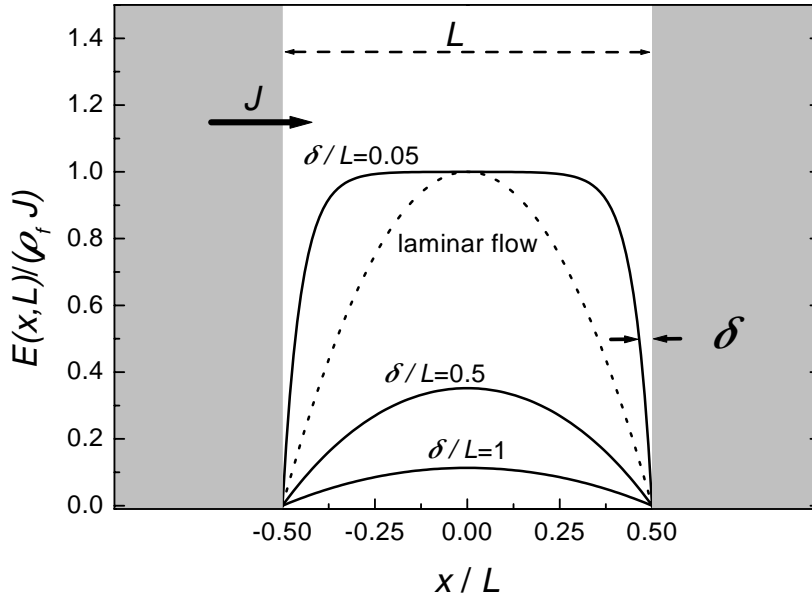
Figure 1.7: *Electric field profile of a Bose-glass contact described by Eq. (1.31) for three different ratios δ/L. The gray regions represent the strong pinning regions. For comparison, the dotted line shows the laminar flow profile $v(x, L)$ for a viscous liquid between to parallel plates.*

density J, bulk resistance ρ_f and is given by

$$E(x, L) = \rho_f J \left[1 - \frac{\cosh(x/\delta)}{\cosh(L/2\delta)} \right]. \tag{1.31}$$

This profile is shown in Fig. 1.7 for different (δ/L)-ratios and a homogeneous current density. The viscous length δ is a measure for the strength of the interaction between the pinned vortices in the strong pinning regions and the unpinned flux lines in the channel. It can be shown that this length is equal to the Bose-glass localization length $l_{\perp}$.

It is worth to mention that this flow profile is different to the parabolic behavior of a laminar flow of a liquid between two parallel plates [56], where the velocity profile is of the form

$$v(x, L) \propto 1 - \left(\frac{2x}{L} \right)^2. \tag{1.32}$$

For comparison this profile is added in Fig. 1.7 in order to visualize this difference. The interface effects are much more pronounced in the case of the vortex fluid indicating the strong vortex-vortex interactions.

However, there are also some common characteristics between these two pictures. Both dynamics depend on the shear viscosity η. A high viscosity in the flow picture means that the velocity $v \propto 1/\eta$ is decreased. In the vortex picture the shear viscosity diverges as

$$\eta \propto |T - T_{\mathrm{BG}}|^{-\nu' z'} , \tag{1.33}$$

on approaching the Bose-glass transition from temperatures $T > T_{\mathrm{BG}}$.

Alternatively it is possible to realize a *Bose-glass contact* using the Corbino disk geometry [57,58]. In such experiments the current is injected at the center and removed at the perimeter of a disk in order to induce a radial current density that decays with $1/r$. For flux lines parallel to the disk axis this current then induces an azimuthal Lorentz-force falling off as $1/r$. This method enables to measure directly the in-plane vortex-vortex velocity correlations and the interface effects at the boundary between pinning for a suitably irradiated geometry.

The discussion of the *Bose-glass contact* shows the relevance of experiments realizing correlated defects in a confined geometry. One way to obtain this is a patterned heavy ion irradiation of thin film structures that will be described in chapter 4.

But nevertheless it is necessary to continue homogeneous heavy ion irradiation with regard to other interesting phenomena. The technologically relevant pinning efficiency of columnar defects can be enhanced by the introduction of *splayed columnar defects* [59]. In this configuration the columnar tracks are not oriented parallel to the crystallographic c-axis, but have an angular spread. This would pin vortex kink pairs and reduce hopping by reducing the number of parallel pinning sites. Apart from the creation of splayed columnar defects with the use of a nuclear fission process [60], these pinning arrangements can be generated in a much more controlled way with swift heavy ions.

Chapter 2

Sample Preparation

This chapter is intended to give a summary of the relevant processes of thin film preparation. The deposition, characterization and the generation of microstructures for $YBa_2Cu_3O_{7-x}$ as well as for $Bi_2Sr_2CaCu_2O_{8+\delta}$ thin films will be reviewed. The heavy ion irradiation is another essential part of the sample preparation. The formation of columnar defects in HTSCs and the used accelerator facilities will also be mentioned.

2.1 Thin Film Preparation

2.1.1 DC Sputtering

Epitaxial $Bi_2Sr_2CaCu_2O_{8+\delta}$ and $YBa_2Cu_3O_{7-x}$ thin films investigated in this work were prepared by dc sputtering. This method is technologically most relevant and is based on a gas discharge between a grounded anode and a cathode representing the HTSC target with a negative potential. Electrons are accelerated away from the cathode and ionize the atoms of a gas atmosphere with a pressure of approximately 3 hPa. The positively charged ions are attracted by the cathode and their impinging on the target knocks out atoms that can diffuse onto a heated substrate. Modified sputtering techniques allow to prepare a variety of thin film systems [61]. The preparation of dielectric thin films by using a high frequency electric field (rf-sputtering) [62] or the deposition of metallic Co/Pt heterostructures in an Ar atmosphere using the magnetron sputtering technique [63] are only two examples.

Three different sputtering chambers, constructed by Jakob [64], Wagner [65] and Frey [66], respectively, were used to obtain epitaxial high quality thin films of the different HTSC compounds on $SrTiO_3$ substrates[1] [67,68]. A detailed

---

[1]also other substrates like MgO or $LaAlO_3$ with better thermal and dielectric properties can be used

description of the complete deposition procedures can be found in the respective references [64–68]. The optimized deposition parameters used in this work are summarized in appendix A.

In this context it is important to note that the preparation of the target is one of the key points in order to obtain high quality $Bi_2Sr_2CaCu_2O_{8+\delta}$ thin films.

2.1.2 Characterization

The structural quality of the thin films was analyzed using X-ray diffractometry (XRD) and microscopic methods. The diffractograms measured in Bragg-Brentano geometry show c-axis growth and the rocking curves of the (0 0 ℓ)-reflexes with the highest intensity [(0 0 10) for $Bi_2Sr_2CaCu_2O_{8+\delta}$ and (0 0 5) for $YBa_2Cu_3O_{7-x}$] have full widths at half maximum $\Delta\omega \approx 0.35°$ indicating good epitaxial growth. The in-plane orientation of the samples was verified in a four cycle diffractometer [69].

In addition, the surface morphology was investigated with scanning electron microscopy (SEM) and atomic force microscopy (AFM). Both methods indicate smooth and homogeneous surfaces comparable to the results obtained earlier [67,68].

2.1.3 Measurement Structures

All measurements reported in this work are based on the electronic transport in the thin films and were carried out in the standard four-probe technique. Well defined geometries were required in order to measure the CVCs or the resistivities The various structures used in this work will be introduced in the respective chapters.

Three main steps were necessary for the preparation of these measurement structures. First, gold or silver pads were evaporated through appropriate metal masks and diffused into the films in order to provide low ohmic contacts. These contacts avoid heating effects and allow to carry out measurements at high current densities. Second, the films were patterned using standard photolithography and chemical wet etching in order to obtain the different microstructures. The use of this method allowed to generate microbridges with minimal widths of $\approx 10~\mu$m. In a third step the patterned samples were mounted on suitable sample holders and connected with the measurement circuit.
Appendix A gives a review of necessary all the steps and the parameters used for the patterning of the different HTSCs, respectively.

2.2 Swift Heavy Ions in Matter

Beside the preparation of high quality HTSC thin films the creation of columnar defects is necessary for a successful investigation of vortex dynamics in the presence of correlated disorder. The columnar tracks are induced by swift heavy ion irradiation of the samples.

The interaction between the accelerated ions (projectile) and the HTSC material (target) determines the structural properties of the defects, whether they will be pointlike or columnar. The basic causes for the ion deceleration in matter are the nuclear S_n and electronic energy loss S_e. The moderation of the swift ions in the energy regime which is relevant for this work is mainly based on their Coulomb-interaction with the target atoms.

In the case of nuclear energy loss, elastic collisions between the projectile ions and the target atoms contribute to the energy transfer. Depending on the transferred kinetic energy, the target atoms are displaced towards interstitial positions or, for higher energies, will cause a displacement of further target atoms resulting in a defect cascade. However, this cascades only have very small dimensions compared to those of a columnar defect which should have a length of the order of at least the film thickness. If the masses of projectile and target nuclei are comparable, the momentum transfer to the target atom lead to distinct changes in velocity and direction of the projectile. This effect is known as straggling because it yields an energy and angle distribution of an initially monoenergetic and quasi parallel beam and is a statistic process.

Collective inelastic interactions between the projectile ion and the electron shell of the target atoms determine the electronic energy loss S_e. The energy is transferred to bound electrons of the target atoms leading to excitations and/or ionizations of target atoms.

The formation of columnar defects can only be achieved if the electronic energy loss exceeds a threshold value of 25 keV/nm in $YBa_2Cu_3O_{7-x}$ and 20 keV/nm in $Bi_2Sr_2CaCu_2O_{8+\delta}$, respectively [70]. Therefore only heavy ions with atomic numbers $Z > 50$ with sufficiently large kinetic energies are appropriate candidates. The dependence of the energy losses from the initial ion energies as well as from the ranges of the projectiles was calculated with the TRIM[2] program developed by Biersack *et al.* [71] and Ziegler *et al.* [72]. Based on experimental results and theoretical calculations the path of a projectile ion through the target is simulated using Monte–Carlo calculations. With this method it is possible to visualize the ion trajectory and to calculate straggling effects. However, the TRIM program does not take into account the crystalline structure of the target material. For compound targets, as in the case of the HTSCs, the calculations are carried out on the base of a stoichiometric weighting of the different target compounds.

---

[2]TRansport of Ions in Matter

Figure 2.1 shows the dependence of the electronic and nuclear energy losses for different ions in $YBa_2Cu_3O_{7-x}$ over a large kinetic energy range. They are characterized by a peaked structure and the respective maxima occur on different energy scales and are shifted to higher values of the kinetic energy with increasing atomic number of the projectile. In addition, the energy losses for projectile ions with $Z < 50$ (e.g. carbon) are negligible and the nuclear energy losses of the illustrated ions are reduced by a factor 6 compared to the maxima in S_e. This pronounced peaks of S_e can be explained by the fact that the velocity of the projectiles corresponds to that of the electrons surrounding the target nuclei at such high kinetic energies. Therefore the most effective interaction between projectile ions and target atoms is guaranteed, yielding a high energy transfer to the electronic system of the target.

The threshold value for the creation of columnar defects in $YBa_2Cu_3O_{7-x}$, indicated by a dashed line, is exceeded only for S_e of the heavy ions. The nuclear energy loss in the kinetic energy range close to the maxima of S_e is negligible.

However, the columnar tracks must be formed over the whole thickness of
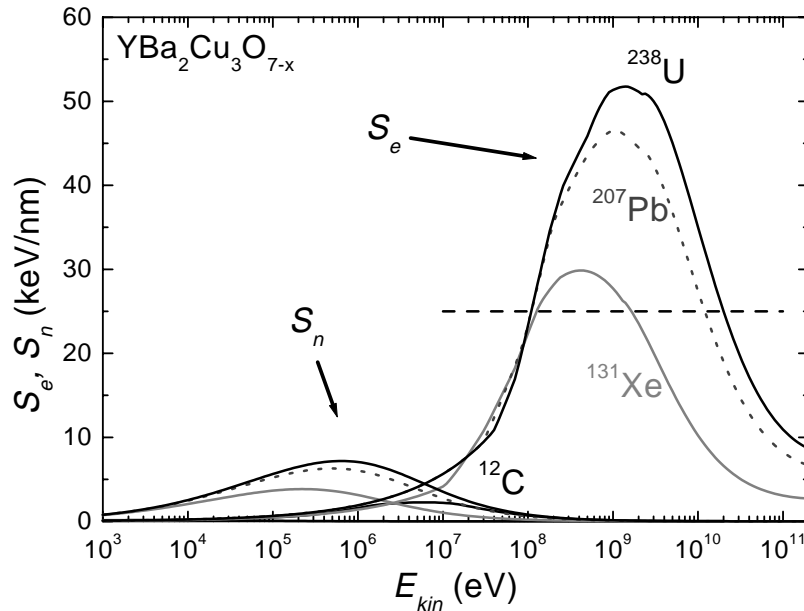
Figure 2.1:   *Dependence of S_e and S_n on the kinetic energy in $YBa_2Cu_3O_{7-x}$ for ^{12}C, ^{131}Xe, ^{207}Pb and ^{238}U resulting from TRIM calculations. The dominating energy loss is of electronic nature and exceeds S_n by a factor 6. The threshold necessary to create columnar defects in $YBa_2Cu_3O_{7-x}$, indicated by the dashed line is only achieved with S_e for the heavy ions. The curves for ^{12}C show that this ion is not useful for the creation of columnar defects. The maximum of S_e for $E_{kin} \approx 10^7$ eV is in the range of 2.5 keV/nm and S_n is not visible on this scale.*
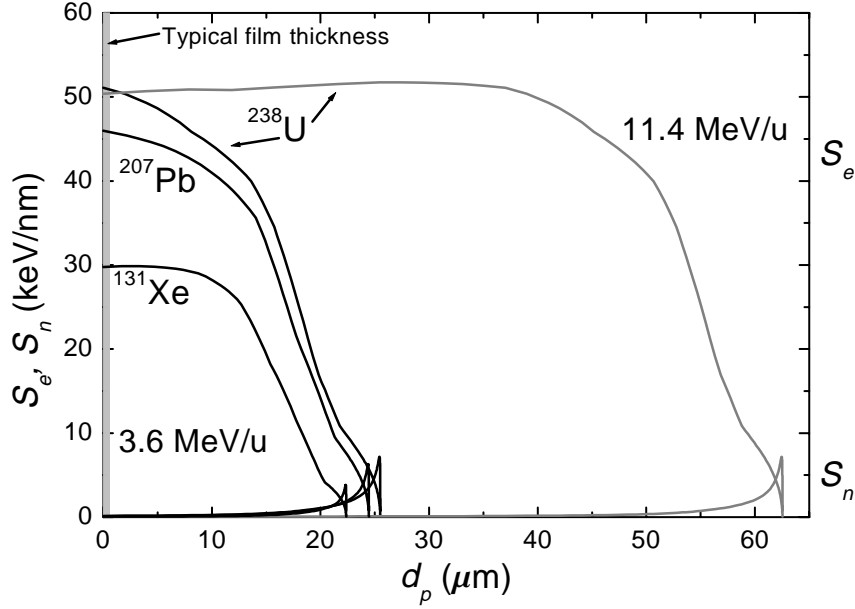
Figure 2.2: *Dependence of the energy losses from the projected ion range for different ion energies (3.6 MeV/u for U, Xe and Pb; 11.4 MeV/u for U) in* $YBa_2Cu_3O_{7-x}$. *For ranges compared to the film thickness (indicated with a gray bar) the electronic energy loss is nearly constant and exceeds the threshold value which is required for the creation of columnar defects, whereas the nuclear energy loss is negligible in this range.*

the thin films and thus the threshold for S_e must be exceeded over a range of approximately $r = 0.4$ μm. If the irradiation is carried out under an angle of $45°$ with respect to the c-axis of the film this range is scaled up to $r \approx 0.6$ μm. In Fig. 2.2 the dependence of the nuclear and electronic energy losses is plotted against the projected range d_p for different ions used in this work. The electronic energy loss of these ions is constant for penetration depths of the order of the typical film thickness which is indicated by a gray bar for $d_p < 1$ μm. Thus, the formation of columnar defects is guaranteed over the whole sample thickness even in the case of a tilted irradiation. Depending on the initial energy of the ions, d_p can achieve more than 60 μm. The TRIM based results show that the nuclear energy loss S_n can be neglected over the whole range except for a very sharp peak at the end of the projectile trajectory where whole nuclear energy is deposited. For light ions like ^{12}C which have a small electronic energy loss, this peak is the main contribution to the total energy loss. In consequence, nearly the whole energy of these ions is deposited within a small volume element whose coordinates depend on the initial ion energy. This is the key idea behind the application of such ions for the tumor therapy at the GSI [73].

The TRIM calculations for $Bi_2Sr_2CaCu_2O_{8+\delta}$ were carried out in an earlier

work [49] and led qualitatively to the same results as for $YBa_2Cu_3O_{7-x}$, illustrated in Figs. 2.1 and 2.2. However, the TRIM program does not contain assumptions about the character of the projectile-target interaction. Currently, two models are considered to describe the possible conversion of electronic excitations into a local destruction of the crystalline structure, resulting in the formation of columnar tacks.

The Coulomb Explosion Model

Due to the ionization of target atoms by the interaction between their electron shells and the passing projectile ion, a long cylinder of positively charged ions exists along the projectile trajectory for times shorter than the response time of the conduction electrons in the target. A repulsive Coulomb interaction between these ionized atoms yield a radial explosion in this cylinder [74,75]. The effect of ionization is directly related to the electronic energy loss and this model indicates that threshold effects may exist.

However, the time scale required to sustain this irregular charge distribution before a re-neutralization takes place depends on the mobility and the number of electrons in the target material. This model holds very well for insulators [76] which have a low electron mobility, but runs into problems for irradiation effects in metals with a high electron mobility.

The Thermal Spike Model

Based on the electron-phonon coupling, the energy deposited in the electronic system of the target material is transferred to the phononic system. This energy transfer yields high temperatures in the vicinity of the projectile. Therefore the target material melts inside a cylindrical volume along the trajectory of the projectile ion. A very rapid cooling of these regions avoids a re-crystallization and causes the formation of amorphous tracks. This thermal spike model was applied to explain the formation of heavy ion induced columnar tracks in $YBa_2Cu_3O_{7-x}$ and $Bi_2Sr_2CaCu_2O_{8+\delta}$ thin films and bulk samples [77]. The thermal conductivity of the target material is an essential parameter for the size and the shape of the defects.

The structure of the columnar defects can be studied using transmission electron microscopy (TEM). Such images show tracks with a diameter of ≈ 10 nm in $Bi_2Sr_2CaCu_2O_{8+\delta}$ thin films irradiated with 1.404 GeV ^{238}U ions, corresponding to an energy per nucleus of 5.9 MeV/u [35]. This is comparable to the order of magnitude of the superconducting coherence length of this material in the crystallographic *ab*-plane. Analog investigations show that the track diameter for irradiated $YBa_2Cu_3O_{7-x}$ thin films also fits very well to its ξ_{ab} [78,79].

2.3 Heavy Ion Irradiation at the GSI

The ions and energies required for the formation of columnar defects can only be provided by a few heavy ion accelerator facilities worldwide. The irradiation experiments presented in this work were carried out at the *Gesellschaft für Schwerionenforschung*, GSI in Darmstadt. This facility provides a variety of heavy ions, from the hydrogen ^{1}H up to the heaviest ions like uranium ^{238}U with kinetic energies per mass between 1.4 MeV/u and 2.0 GeV/u. In order achieve this large bandwidth of ions and kinetic energies, the heavy ion accelerator facility of the GSI consists of two essential parts, the UNILAC[3] and the SIS[4] with subsequent fragment separator (FRS) and experimental storage ring (ESR). The previous section showed that the creation of columnar defects requires the exceeding of a HTSC compound specific track formation threshold. Ions with $Z > 50$ accelerated by the UNILAC fulfil this condition and the use of the SIS was not necessary for the irradiation of the HTSC thin films in this work

A schematic illustration of the UNILAC part is shown in Fig. 2.3. For the formation of the columnar defects, ions are injected with 1.4 MeV/u into the Alvarez section with the use of a high charge state injector (HLI[5]) or the Penning source that is followed by a Wideröe structure. Together with single gap resonators, the Alvarez section is used to increase the kinetic ion energies and to achieve a continuous energy variation up to approximately 13 MeV/u. A detailed overview of the of the UNILAC as well as the technical details are found in References [80] and [81]. Since 1999, the Wideröe structure was replaced by a high current injector HSI[6] [82,83] in order to improve the beam characteristics with respect to the ion injection into the SIS.

The entire beam line must be operated in a vacuum of at least 10^{-6} hPa (UNILAC) or even in ultra high vacuum for higher ion energies in order to avoid intensity losses due to interactions between the ions and residual gas atoms. The provided ion beam has an intrinsic time structure with a pulse length of approximately 5 ms, superimposed to a macro structure with a maximum frequency of 50 Hz. The ion beam is guided to the appropriate beam line using magnetic lenses.

Two beam lines in the experimental hall which directly joins the UNILAC facilities were used for the irradiation of the $Bi_2Sr_2CaCu_2O_{8+\delta}$ and $YBa_2Cu_3O_{7-x}$ thin films. At beamline Z5 all standard irradiations were performed, whereas the Microprobe of beam line X0 was used in order to realize patterned irradiations with a resolution in the μm-range (cf. section 4.5).

---

[3]UNIversal Linear ACcelerator
[4]SchwerIonenSynchrotron
[5]HochLadungsInjektor
[6]HochStromInjektor
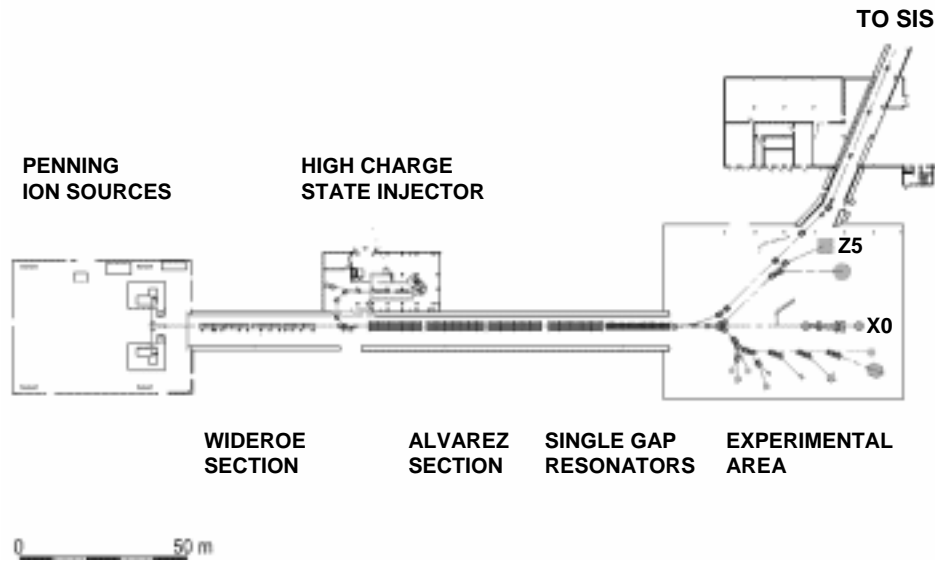
Figure 2.3:   *Schematic representation of the UNILAC structure consisting of four sections that are explained in the text. The irradiations of the samples took place at the beam areas Z5 (standard irradiation) and X0 (microprobe). In 1999, the Wideröe section was replaced by the HSI.*

2.3.1   Standard Irradiation

Heavy ion irradiations were mainly performed at the Z5 branch of the UNILAC experimental hall. During several years this beamline was adapted to the requirements of heavy ion irradiation of HTSCs [49,84], which are a homogeneous intensity distribution for a large beam spot, a detailed beam analysis and a vacuum system that enables to load different samples and glass substrates rapidly. The term "standard" in this context means that the whole sample can be irradiated homogeneously. Only the use of metal masks limits the irradiated area as will be described in detail in chapter 4.

Figure 2.4 shows the experimental set-up of the Z5 branch in the UNILAC experimental hall. The gate valve separates accelerator and experimental area and can be understood as a part of the vacuum protection system of the accelerator facility. Behind this valve the experimentalists are responsible for the experimental set-up including the vacuum of the beam tube. A Faraday cup is placed behind the gate valve in order to measure the ion beam current which gives a first information about the beam intensity. Position, shape and extension of the ion beam can also be analyzed using a wire grid. By defocusing the ion beam the required homogeneity of the beam intensity is obtained. A circular aperture assures that the beam spot has a diameter of approximately 30 mm.

The beam characteristics are checked using different analyzers. Two fluorescent screens allow to evaluate the intensity distribution of the spot behind the aperture with the help of a triggered flash-camera. A first tuning of the ion beam was carried out using the aluminum sinter ceramic (ALSINT) screen which is very resistive against the irradiation and enables adjust the beam profile by taking many subsequent pictures. A precise analysis of the lateral beam intensity distribution is carried out using a very sensitive chromium-oxide screen. Therefore a fast chopper selects only one single macro pulse that irradiates the screen. Such a snapshot is shown in Fig. 2.5, proving that the ion distribution is very homogeneous in the second inner circle which represents an area of 12.5 cm^2. The variation of the intensity outside this area is irrelevant because the position of the 10×10 mm^2 large samples is in the center of the beam axis. It is indicated by the cross in the center of the snapshot. These images were repeatedly taken during the irradiations in order to ensure homogeneous beam properties. Alternatively, it is possible to scan the beam spot with a scan-scintillator in order to determine the beam homogeneity. During these adjustments the sample remains in the idle position of the load lock in order not to irradiate the samples by accident.

Apart from the homogeneity of the ion beam the direct measurement of the ion dose is necessary in order to determine the matching field defined in section 1.3. During the irradiation these measurements are performed by two detectors. The Online-scintillator consists of a 100 μm thick NE102A scintillator foil that is
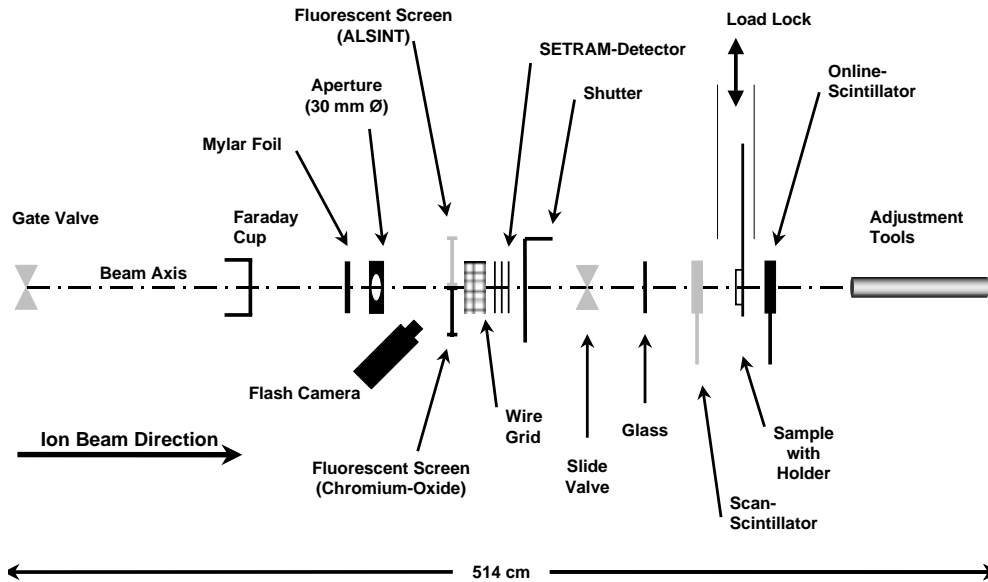
Figure 2.4: *Experimental set-up at beamline Z5 for the standard irradiation. The explanation of the diverse components is given in the text.*
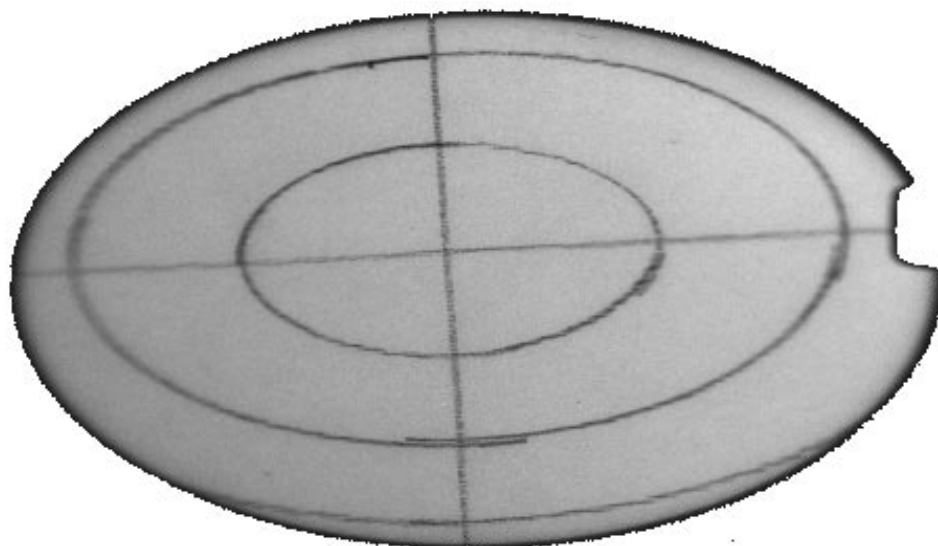
Figure 2.5:   *Intensity distribution of the ion beam using a chromium-oxide*
fluorescent screen. The circles have radii of 10 mm, 20 mm *and* 30 mm,
respectively. The cross in the center of the circles represents the position of
the beam axis. An analysis of the intensity profile in the inner circle reveals a
maximal change of less that 10%.

placed behind a high precision pinhole with an area of 7.85×10^{-5} cm^2 (100 μm
diameter). It is positioned directly above the sample at a distance of 2 mm
(7 mm from the beam axis). This detector counts each ion provided that the ion
frequency does not exceed 500 kHz. The validation of the set-up of this scintillator
is made by irradiating a glass substrate with a low ion dose ($\approx 4 \times 10^6$ ions/cm^2).
After etching the substrate in 18 % HF-acid the ion tracks become visible and
one can compare the number of tracks per area to the number of counts in the
Online-detector.

A SETRAM-detector is used to measure the beam intensity online in an integral
form. Secondary electrons are created in a thin carbon foil (0.1 μm, 25 μg/cm^2)
which is enclosed by two other foils where the electrons are collected. The current
is a measure for the number of ions that passed the detector. In combination with
the Online- scintillator this allows a cross-checking between the two detectors.

2.3.2   Microprobe Irradiation

The microprobe in the X0 beam line was used to carry out high resolution pat-
terned irradiation. The set-up for this irradiation technique is very different to
the equipment of the Z5 branch. Figure 2.6 gives a schematic illustration of
the irradiation principle and shows the main features of this beam line. Two
apertures and a magnetic quadrupole lens are necessary to project the desired
irradiation patterning onto the sample. Following the ion beam, the first aperture

consists of an image of the structure to be written. In general it is formed of a
$10 \times 10 \ \mu m^2$ square hole and cuts off most of the beam. Ions that passed this slot
drift through a 3 m long tube and are projected by the magnetic lens onto the
sample and the area of the first aperture is scaled down with a ratio of 8:1. A
second aperture (100 μm diameter) is placed just in front of the lens and avoids
the projection of scattered ions onto the sample. Each ion that hits the sample
is indirectly detected with a channeltron detector that is placed parallel to the
beam axis in front of the sample. It amplifies the secondary electrons that are
produced at the incidence of the ion on the target with a factor 10^9. The high
accuracy of this detector combined with a high voltage chopper allows to irradi-
ate the sample with single ions. This chopper can switch off the ion beam once
a single ion has reached the sample. A detailed description of the experimental
set-up of the microprobe as well as its applications are found in Ref. [85].

With the described procedure it is possible to irradiate a sample at a fixed
position because the microprobe cannot "write" in a scanning mode. In order to
create an irradiation pattern it is necessary to move the sample with micromanip-
ulators in the plane perpendicular to the beam axis. Such structures generated
with single ion pulses are very regular and homogeneous [86]. However, for the
irradiation patterns described in chapter 4 this procedure does not apply because
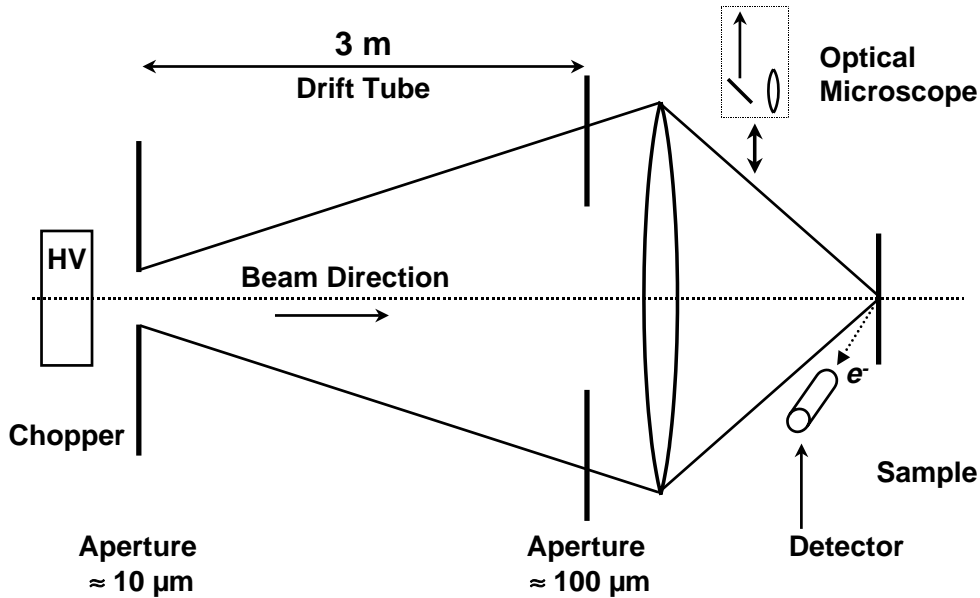
Figure 2.6: *Schematic representation of the microprobe principle. Ray
tracing is in accordance with geometrical optics. The ion lens is formed by a
quadrupole magnet. This down scaling projection allows to place one single
ion with a precision of approximately 1 μm. Drawing is not to scale.*

ion doses of 5×10^{10} ions/cm^2 are required and a very long time would be needed for the realization of such a dose. Therefore the projection aperture was modified for the HTSC microprobe experiments. The square hole was replaced by a rectangular slot ($1500 \times 100 \ \mu$m^2) to irradiate 10 μm wide and 150 μm long strong pinning channels.

Such irradiations require a good knowledge of the sample coordinates. The exact position of the sample is adjusted with the use of an optical microscope that can be moved on and removed from the beam axis. In addition, several beam characteristics are necessary for microprobe irradiations. It is clear from Fig. 2.6 that the incident beam should be parallel. This implies vacuum conditions better than 10^{-6} hPa in the whole beamline in order to avoid the scattering of the swift ions with other atoms yielding an energy loss and a deflection of the concerned ions. A high beam intensity is also required for a successful irradiation.

The use of the microprobe in this work is limited to a single experiment that is described in chapter 4 within the framework of patterned irradiation of YBa$_2$Cu$_3$O$_{7-x}$ thin films. This irradiation technique was applied to HTSCs for the first time in order to estimate the potential perspectives of this method.

Chapter 3

Vortex Dynamics in the Presence of Correlated Disorder

Measuring the electrical transport properties of HTSC thin films is a standard method to access vortex dynamics and allows to probe the predictions within the framework of the vortex-glass and Bose-glass theory described in chapter 1. Voss-de Haan *et al.* pointed out the importance of an enlarged experimentally accessible measurement window in the context of the vortex-glass scaling analysis and introduced a technique enabling to increase the electric field sensitivity using extremely long measurement bridges [12,21]. Based on these results obtained on unirradiated $YBa_2Cu_3O_{7-x}$ thin films, transport measurements were continued on the same sample after heavy ion irradiation with different ion doses to investigate vortex dynamics in the presence of correlated disorder.

This chapter will first give a motivation for the use of long measurement bridges. A discussion of the superconducting sample properties and the effects produced by columnar defects will follow. The main part of this chapter focuses on the analysis of experimentally determined current-voltage characteristics (CVCs) within the framework of the Bose-glass scaling for different ion doses, external magnetic fields and temperatures. It is pointed out that the critical scaling strongly depends on the accessible experimental window revealing deviations from the underlying theory. A study of the current dependent activation energy and some concluding remarks will terminate this chapter.

3.1 Long Measurement Bridges

A long current pulse with amplitude I is fed into and the corresponding voltage drop V across a microbridge is measured for different external magnetic fields

and temperatures[1]. The calculation of J, E and ρ then depend on the geometric properties of the samples,

An improvement of the electric field sensitivity can be achieved in increasing the sensitivity of the voltage measurement. This can be realized if the detected voltage is amplified [87] or if the voltage is measured repeatedly at the same parameters and averaged in order to increase the signal to noise ratio. Another approach to this problem can be found in taking advantage of the definition of the electric field

$$E = \frac{V}{\ell}, \tag{3.1}$$

where ℓ denotes the length of the measurement bridge, i.e. the distance between the voltage probes. A large distance thus yields a higher sensitivity in E [12] for a given voltage. Compared to bridges with conventional lengths of approximately 2 mm where the electric field sensitivity is in the order of 10^{-5} V/m, the sensitivity is by a factor 50 better for 10 cm long measurement bridges.

The preparation of these complex structures is a non-trivial work. For a given structure width, the patterned area is increased by a factor 50 or more compared to conventional measurement bridges. This requires a high homogeneity regarding the superconducting and structural properties of the samples. In addition, the patterning of the microstructure should be performed under reproducible and clean conditions in order not to obtain any "weak points" like a reduced channel width due to any dust particles on the film surface during micropatterning.

3.2 Sample Preparation

Micropatterning under clean room conditions fulfils the requirement of a homogeneous sample preparation. As the parameters for the photolithographic steps (see appendix A) depend on the environmental temperature and humidity, the constant conditions in a clean room contribute to a reproducible micropatterning.

3.2.1 Microstructure

The structure used in this case is shown in Fig. 3.1. The 109 mm long and 50 μm wide measurement bridge has a spiral form. The thickness of this $YBa_2Cu_3O_{7-x}$ film denoted Y 12 10 98, is 400 nm [12]. Four gold pads, two in the middle and two outside the spiral, respectively, were contacted with 25 μm thick ultrasonically

---

[1]The length of the current pulses for these experiments is of the order of 1 s. It is also possible to perform time-resolved CVC measurements with significantly shorter current pulses as shown in chapter 6.
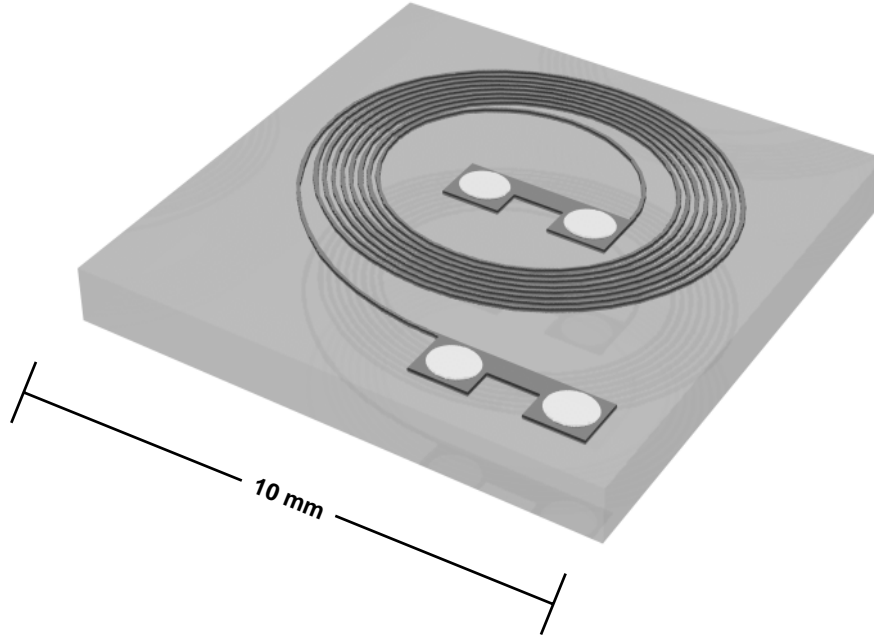
Figure 3.1: *Geometry of the long measurement bridge. The helical structure is* 109 mm *long and has a width of* 50 μm. *The structure contains two contact surfaces, each with two gold pads. The inner contacts that are close to the measurement bridge serve as voltage probe, the outer pads of each contact area is used for the feeding of the current.*

bonded aluminum wires to supply the connection to the measurement equipment and to perform measurements in an approximately standard four-probe geometry. The contacts on the inner side of the contact area close to the long spiral bridge are connected to a nanovolt meter, the outer ones to a current source.

It is worth to mention in this context that the distance ℓ between the voltage probes in this helical configuration only is limited by the width of the measurement bridge. A 20 μm wide and 690 mm long spiral was patterned and measured successfully. The generation of microstructures with dimensions below these values resulted in inhomogeneous bridges that made electronic transport measurements less meaningful.

3.2.2 Irradiation

The extended microstructure described above does not allow an irradiation technique presented in Ref. [49], where three of four identical striplines were irradiated with different ion doses and/or under different angles with respect to the crystallographic c-axis in order to measure irradiated and virgin bridges together in parallel on the same sample. Therefore the increase of the ion dose of Y 12 10 98 was performed during three independent beam times and the transport prop-

Table 3.1: *Schedule of the different irradiations for the* $YBa_2Cu_3O_{7-x}$ *film* Y 12 10 98. *The total irradiation dose was successively increased.*

Date	Ion	Total Energy	Dose	Total Dose
Dec. 1998	^{209}Bi	0.752 GeV	0.6 T	0.6 T
May 1999	^{208}Pb	0.749 GeV	1.0 T	1.6 T
Mar. 2000	^{238}U	1.142 GeV	1.4 T	3.0 T

erties were measured in between. Table 3.1 summarizes the parameters of the three subsequent irradiations which were carried out with three different ions. The complex beam time schedule and the predetermination of the kind of ion at the GSI did not allow to use the same sort for all irradiations. However, the structural differences of columnar defects generated by different ions is assumed to be marginal. The whole sample was irradiated homogeneously without covering the sample partly by any beam aperture.

3.3   Superconducting Properties

The measurements of the transport properties of the pristine thin film Y 12 10 98 were carried out in an earlier work [12,21]. They are shown here to compare the effects of irradiation with the results of the unirradiated sample. Figure 3.2 shows the temperature dependent resistive transitions in zero magnetic field after the different irradiation cycles as well as for $B_\phi = 0$ T. All measurements were performed at a fixed current density $J = 5$ A/cm^2 using a *Keithley 224* dc current source. The voltage drop was measured with a *Keithley 182* nanovolt meter.

Figure 3.2 illustrates two effects which appear with increasing ion dose. First, the normal state resistivity is increased, a fact that has been reported earlier in the context of irradiated $YBa_2Cu_3O_{7-x}$ samples [88–91] as well as for $Bi_2Sr_2CaCu_2O_{8+\delta}$ [49,92,93] and other HTSC compounds [94,95]. The relative resistivity difference for an ion dose ϕ at a fixed temperature

$$\Delta\rho(\phi, T) = \frac{\rho(\phi, T) - \rho(0, T)}{\rho(0, T)} \tag{3.2}$$

shows a parabolic dependence of the ion dose for temperatures $T > 95$ K. For higher doses this nonlinear behavior is also valid [90]. In addition, a decrease of the transition temperature T_c with increasing ion dose is observed. For ion doses exceeding the typical irradiation doses in this work by a factor 200 it is even possible to destroy superconductivity [88,95] completely. In such cases the samples show semiconducting $\rho(T)$ characteristics. In contrast to the nonlinear
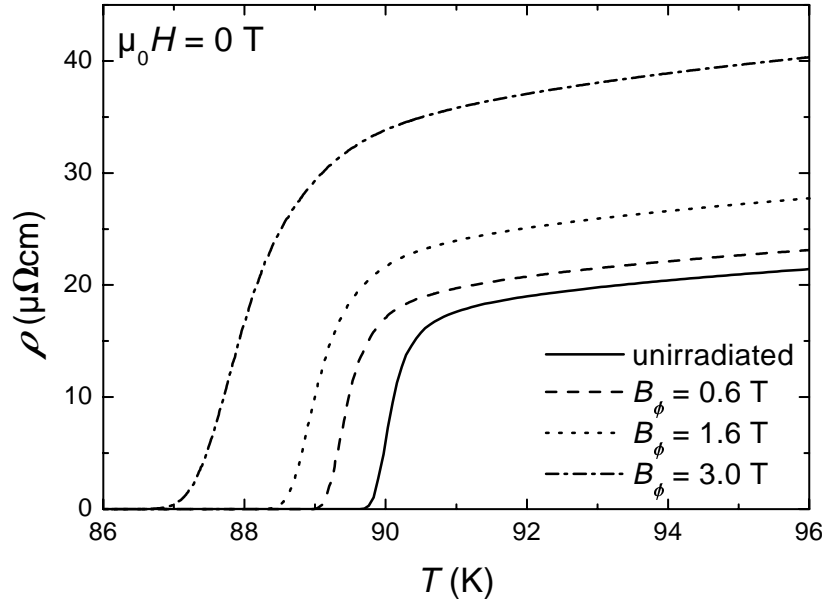
Figure 3.2: *Resistive transitions of the* $YBa_2Cu_3O_{7-x}$ *film* Y 12 10 98 *before and after irradiation in zero magnetic field. An increased ion dose yields an increase of the normal state resistivity as well as a decrease of the transition temperature.*

increase of the normal state resistivity the reduction of T_c is linear in B_ϕ within the applied fluence range as can be seen in Fig. 3.3. Associated with the reduction of T_c the width of the superconducting transition ΔT_c is broadened (cf. table 3.2).

These effects can be explained using a model based on mechanical stress considerations which does not take into account microscopic defects in detail [90]. The heavy ion tracks of amorphous $YBa_2Cu_3O_{7-x}$ increase ρ due to their poor resistivity, corresponding to the picture of insulating columns in a conducting matrix. In addition, the crystalline–amorphous transition is accompanied by a reduced density inside the columnar defect compared to the perfect crystal. As a consequence this deficit results in a volume increase. But this expansion is frustrated by the surrounding matrix and stress will develop in the vicinity of the tracks [96]. These highly anisotropic stresses (stress is mainly developed in the *ab* planes) are connected with strains of the crystallographic axes and can be measured using XRD [89].

The above mentioned and illustrated transport properties in zero magnetic field are summarized in table 3.2, where two possibilities of determining the transition temperature, the midpoint of the transition is defined by T_c and $T_c^0 \equiv T(\rho \longrightarrow 0)$ are listed. In addition, values for ΔT_c are quoted.

In addition to the determination of the superconducting properties in zero magnetic field, resistive transitions were measured for applied external magnetic
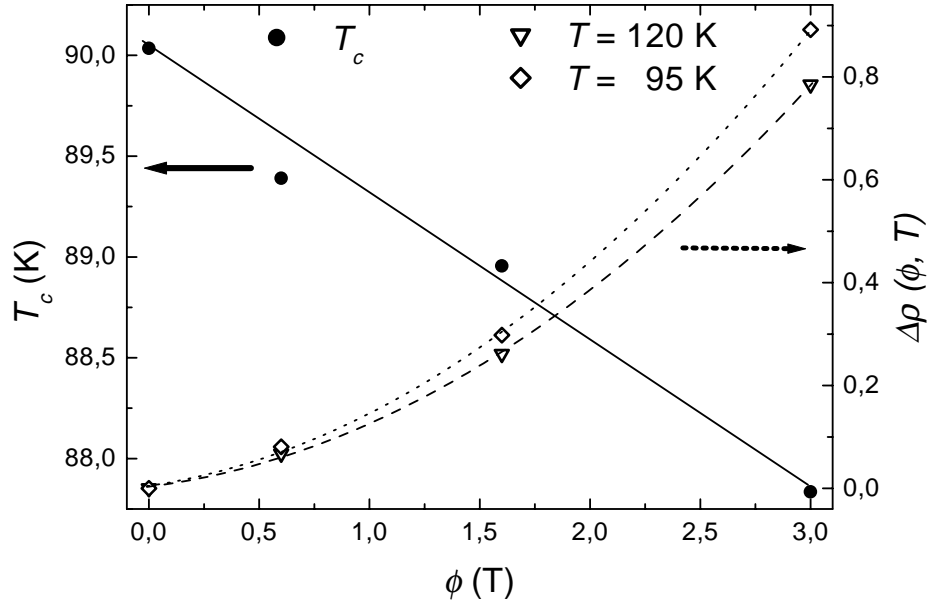
Figure 3.3:   Ion dose dependencies of the transition temperature and of
the normal state resistivity for the film Y 12 10 98. T_c is decreased linearly
with ϕ, whereas the resistivity in the normal state shows a parabolic behavior
with increasing ion dose, indicated by the additional fitted curves (dotted and
dashed line). Note that the solid line through the $T_c(B_\phi)$ data is only a guide
to the eye.

Table 3.2:   Irradiation effects for the film Y 12 10 98 on the main electrical
transport properties. Two representations of the transition temperatures are
given. The midpoint of the transition is indicated by T_c, at T_c^0 the resistance
is not measurable any more. The transition width ΔT_c is determined by the
full width at half maximum of the $\frac{d\rho(T)}{dT}$ curves.

Total Dose	0 T	0.6 T	1.6 T	3 T
$\rho_{120\ \mathrm{K}}(\mu\Omega\mathrm{cm})$	28.5	30.5	36.0	51.0
$\rho_{95\ \mathrm{K}}(\mu\Omega\mathrm{cm})$	21.0	22.7	27.2	39.7
T_c (K)	90.0	89.4	89.0	87.8
T_c^0 (K)	89.5	88.8	88.0	86.1
ΔT_c (K)	0.9	1.2	1.6	2.5

fields up to 4 T for the unirradiated sample as well as $B_\phi = 0.6$ T and $B_\phi = 1.6$ T.
In order to estimate the activation energy U_0 for different magnetic fields and ion
doses the resistivity was represented in a set of Arrhenius-plots
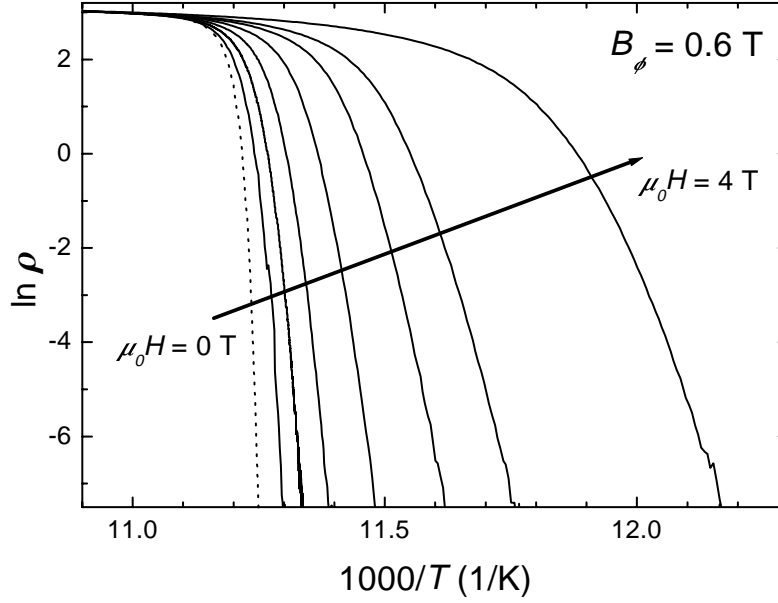
Figure 3.4: *Arrhenius plots of the resistivity data of the irradiated film* Y 12 10 98 *for* $B_\phi = 0.6$ T *and external magnetic fields* ($\mu_0 H$: 0 T, 0.1 T, 0.3 T, 0.6 T, 1.0 T, 1.5 T, 2.0 T *and* 4.0 T). *The linear slope of the resistive transitions is used to estimate the activation energies.*

$$\ln \rho(B, T) = \ln \rho_0(B) - \frac{U_0(B)}{k_B T} \tag{3.3}$$

as shown in Fig. 3.4. In this representation the slope of the linear part of the resistive transition is an approximation for the value of the activation energy ($k_B \equiv 1$), supposing a constant or linear temperature dependence[2] of the activation energy. The results of this analysis are shown in Fig. 3.5, where the activation energy is plotted against the external magnetic field on a double logarithmic scale. In particular, the curves of the irradiated samples can be divided in two regimes, separated by a characteristic field. This crossover is described by different power law behaviors

$$U \propto B^{-\alpha}, \tag{3.4}$$

 indicated by the linear fits for low magnetic fields. The corresponding exponents are indicated in Fig. 3.5 and by the line representing the power law with $\alpha = 0.5$. In the low field regime the activation energy shows a weak magnetic field

---

[2]A more detailed analysis of $U_0(T)$ [97] shows that $U_0 \propto (1 - T/T_c)^5$.
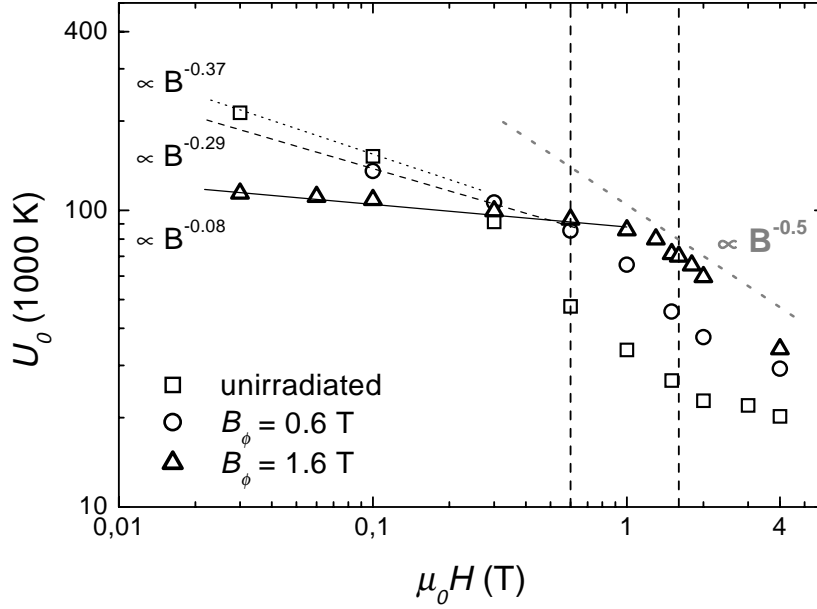
Figure 3.5:   *Double logarithmic plot of the magnetic field dependence of the activation energy. The vertical lines indicate the corresponding ion dose equivalent fields, the gray dashed line represents the $B^{-0.5}$ dependence of U_0 predicted within the framework of thermally activated motion of the vortices by plastic deformations. A weaker dependence is observed for low magnetic fields.*

dependence. The exponent α is reduced with the ion dose and for $B_\phi = 1.6$ T the activation energy is nearly field independent. For high fields. the slope of the $U_0(\mu_0 H)$ curves changes to $\alpha \approx 0.5$. This value is in agreement with earlier results [98] and is characteristic for a thermally activated motion of vortices by plastic deformations [99]. The crossover field is in the order of B_ϕ (vertical lines) for the irradiated samples. In the presence of columnar defects this change in the slope of the $U_0(\mu_0 H)$ dependence is attributed to the crossover from individual to collective vortex depinning [100]. In the unirradiated case this crossover is not pronounced, but a kink is also observed for $B \approx 0.1$ T.

Additional information is provided in the high field regime of the magnetic field dependence of the activation energy illustrated in Fig. 3.5. An enhancement of U_0 that is increased with increased ion dose is observed in the irradiated samples. For magnetic fields in the order of the ion dose equivalent field $B \approx B_\phi$ this enhancement of the activation energy is most distinct. In this regime the number of flux lines matches the number of columnar defects and vortex pinning is most effective. This result proves the strong pinning activity of heavy ion induced columnar defects which also plays an important role for the investigation of CVCs. The influence of the increased barrier height on the CVCs in the irra-

diated samples will be studied in the following section. In particular the scaling analysis of these CVCs will be the object of this discussion.

3.4 Current-Voltage Characteristics

The voltage drop across the helical structure for different magnetic fields and temperatures was measured by varying the current density over more than 7 decades. A set of isotherms for an ion dose equivalent field $B_\phi = 0.6$ T and an external magnetic field $\mu_0 H = 1.0$ T is shown in Fig. 3.6. In this representation the electric field is extended from 1 V/m to $\approx 3 \cdot 10^{-8}$ V/m. The dashed lines separate the regions of free flux flow (FFF) at high temperatures $T > T^* = 88$ K and high electric fields $E > 10^{-2}$ V/m from the different states of vortex dynamics as identified in connection with Fig. 1.2. A Bose-glass scaling analysis excludes the regions of FFF and takes into account only the CVCs below this upper bound. In this region three different regimes of the CVCs are distinguished. For tem-
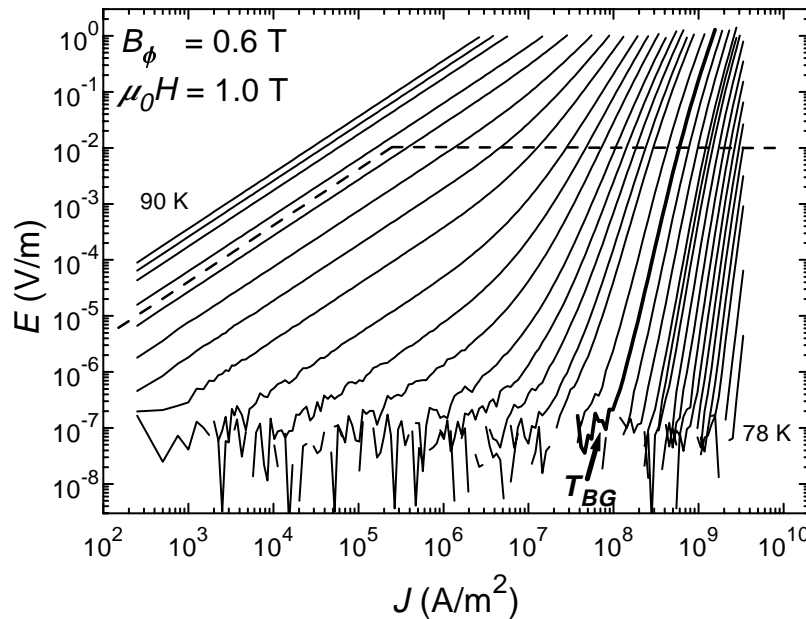
Figure 3.6: *CVCs of* Y 12 10 98 *irradiated with an ion dose equivalent field* $B_\phi = 0.6$ T *in an external magnetic field* $\mu_0 H = 1.0$ T *for temperatures between 78 K and 90 K. In this case the Bose-glass transition temperature following from a scaling analysis is* $T_{BG} = 85$ K. *The dashed lines indicate the upper bounds in* E *and* T *of the CVCs used for a Bose-glass analysis.*
(T : 78.0 K, 79.0 K, 80.0 K, 80.5 K, 81.0 K, 81.4 K, 81.8 K, 82.2 K, 82.6 K, 83.0 K, 83.4 K, 83.6 K, 83.8 K, 84.2 K, 84.6 K, 85.0 K, 85.4 K, 85.8 K, 86.0 K, 86.2 K, 86.4 K, 86.6 K, 86.8 K, 87.0 K 87.2 K, 87.4 K, 87.6 K, 87.8 K, 88.0 K, 88.2 K 88.6 K, 89.0 K, 90.0 K)

peratures $T_{BG} < T \leq T^*$ a linear $E(J)$ behavior is found for current densities $J < J_x^+$. In the limit of small current densities this thermally activated regime is characterized by a nonvanishing linear resistance. In the critical region above the crossover current density J_x^+ (see Eq. (1.27)) the isotherms show a positive curvature, followed by a negative curvature at high E indicating the FFF region. An adequate scaling ansatz of the CVCs in this regime is given by Eq. (1.23). The labeled isotherm at T_{BG} corresponds to the line which separates the CVCs at electric fields $E < 10^{-2}$ V/m with positive curvature from those with a negative one. In a double logarithmic plot this glass line is linear over the entire current range with a slope that follows from Eq. (1.24)

$$\log(E) \approx \frac{z' + 1}{3} \log(J). \tag{3.5}$$

Below T_{BG} the resistivity vanishes in the limit of small currents and the nonlinear CVCs can be described in accordance with Eqs. (1.15), (1.16) or (1.17), depending on the type of vortex loop excitation described in section 1.3

3.4.1 Bose-Glass Scaling

In order to extract the critical behavior near the Bose-glass transition from the CVCs of the sample two methods were applied in this work. First, the method of crossover current densities will be discussed. It enables to extract the Bose-glass temperature and the dynamic critical exponent. In a second step a Bose-glass analysis based on the scaling ansatz of Eq. (1.21) is also used to extract T_{BG}, z' and additionally the static critical exponent ν'. The results obtained from the crossover current method can be used as start parameters for the scaling analysis. Furthermore the reliability of the extracted scaling parameters is increased if both methods are combined.

Crossover Current Densities

The current density at which an isotherm $T > T_{BG}$ deviates from its linear $E(J)$ dependence (1.23) at low currents is defined as the crossover current density J_x^+. For currents $J > J_x^+$ the respective $E(J)$ curve asymptotically approaches the power law dependence of the glass line (1.24). The critical behavior of the crossover current is described in Eq. (1.27).

Figure 3.7 shows a set of isotherms in a magnetic field $\mu_0 H = 1.0$ T after the irradiation with $B_\phi = 1.6$ T. A criterion was introduced in order to determine the crossover field E_x^+ and J_x^+ for each isotherm

$$E_x^+\big|_{T=\text{const}} \equiv \frac{E^{\text{exp}} - E_{\text{lin}}^{\text{Fit}}}{E_{\text{lin}}^{\text{Fit}}} > 10\%, \tag{3.6}$$
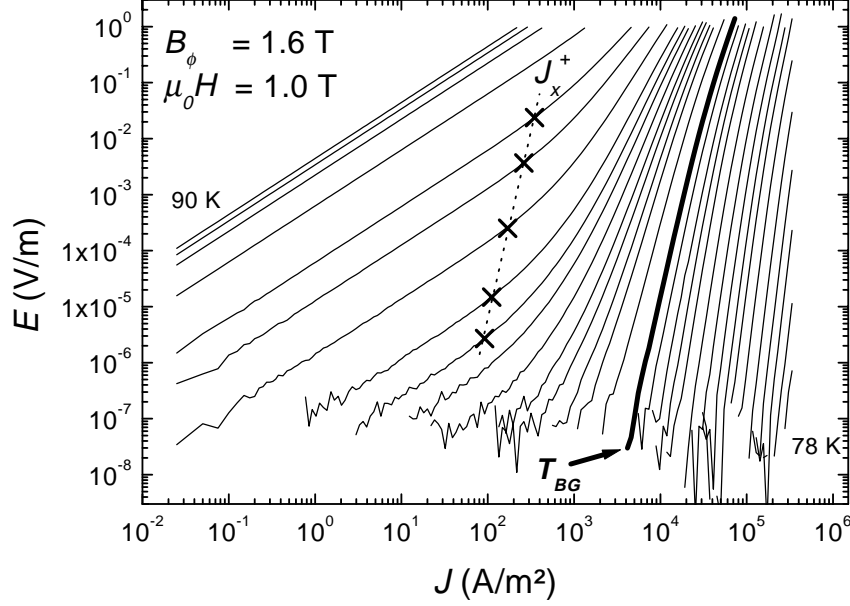
Figure 3.7: *CVCs of the sample Y 12 10 98 irradiated with $B_\phi = 1.6$ T at $\mu_0 H = 1.0$ T in a double logarithmic representation for temperatures between 78 K and 90 K. The crosses indicate the crossover current densities for the respective isotherms. The slope of the $E_x^+(J_x^+)$ line (dashed) is equal to the slope of the $E(J)$ curve at T_{BG} (bold solid line, indicated by an arrow).*
(T : 78.0 K, 79.0 K, 80.0 K, 80.8 K, 81.6 K, 82.4 K, 83.0 K, 83.4 K, 83.8 K, 84.2 K, 84.6 K, 85.0 K, 85.2 K, 85.4 K, 85.6 K, 85.8 K, 86.0 K, 86.3 K, 86.4 K, 86.5 K, 86.6 K, 86.7 K, 86.8 K, 86.9 K, 87.0 K, 87.2 K, 87.4 K, 87.6 K, 88.0 K, 88.5 K 89.0 K, 90.0 K)

where E^{exp} is the measured electric field and $E_{\mathrm{lin}}^{\mathrm{Fit}}$ is a fit of the experimentally obtained linear $E(J)$ data which is projected to higher current densities at which the upturn into the asymptotic approach to the power law dependence of the glass line already took place. The dependence of the crossover field from J_x^+ is known from Eq. (1.28) and in the double logarithmic $E(J)$ representation of Fig. 3.7 the dotted $E_x^+(J_x^+)$-line should be parallel to the isotherm at T_{BG} which is indicated by the bold solid line. It follows from Eq. (1.24) that the slope α of these lines contains the dynamic critical exponent z'. In the present example $\alpha = 6.4(1)$ yielding $z' = 18.2(3)$. The corresponding Bose-glass temperature is determined to $T_{BG} = 85.9(1)$ K.

Scaling Analysis

The in the vicinity of T_{BG} low temperature and low field regimes of the CVCs illustrated in Fig. 3.7 are also analyzed with the use of the scaling analysis described by Eq. (1.21). Therefore the electric field and current densities were converted

into the corresponding scaled quantities defined in Eqs. (1.25) and (1.26). Figure 3.8 shows the result this analysis for the indicated scaling parameters (T_{BG}, z' and ν'). Good scaling is achieved if all CVCs of the relevant regimes collapse onto two branches: all isotherms $T > T_{BG}$ on the upper branch, all isotherms $T < T_{BG}$ on the lower one. This kind of analysis only allows to evaluate the quality of the scaling and the right choice of the corresponding parameters by visual inspection. Comparing the Bose-glass temperature and the dynamic critical exponent z' resulting from the scaling analysis with the respective values obtained from the method of crossover current densities shows that both ways yield consistent results.

The obtained value for the static critical exponent is in agreement with the theoretical prediction $\nu' \simeq 1.0\pm0.1$ revealing from Monte-Carlo simulations [43] as well as with many experimental findings. However, the dynamic critical exponent $z' = 17.8 \pm 0.3$ is not compatible at all neither with theoretical predictions nor with other published experimental results. Numerical simulations of the vortex glass transition in the presence of columnar defects using a vortex loop model yield $z' = 6.0 \pm 0.5$ [101]. Scaling analysis of experimentally obtained CVCs result in values for z' between 4 and 11.3. The YBa$_2$Cu$_3$O$_{7-x}$ samples used in
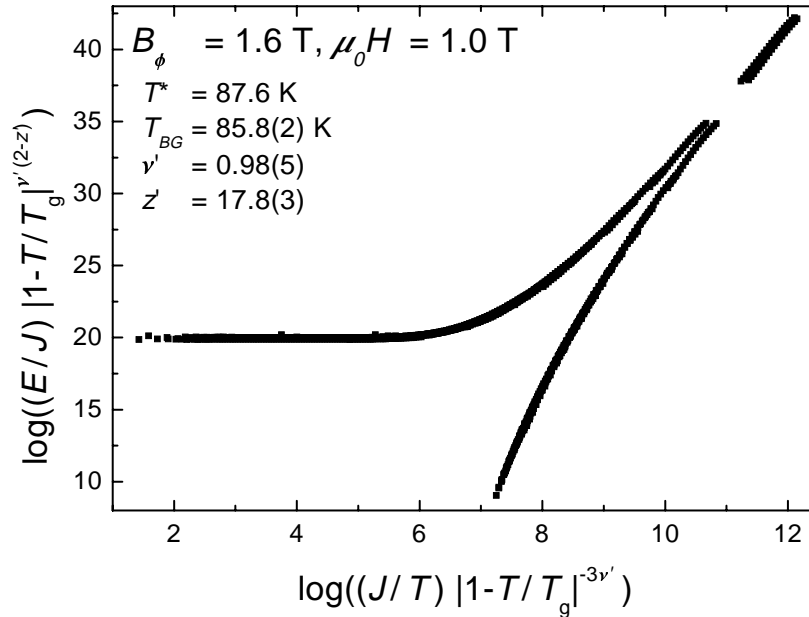
Figure 3.8:   *Bose-glass scaling of the CVCs of Y 12 10 98 with $B_\phi = 1.6$ T and $\mu_0 H = 1.0$ T. The analysis is performed for electric fields $3 \cdot 10^{-8}$ V/m $< E < 10^{-2}$ V/m. The relevant CVCs collapse onto two branches within the accuracy of the symbol size for a Bose-glass temperature $T_{BG} = 85.8(2)$ K as well as critical exponents $z' = 17.8(3)$ and $\nu' = 0.98(5)$.*
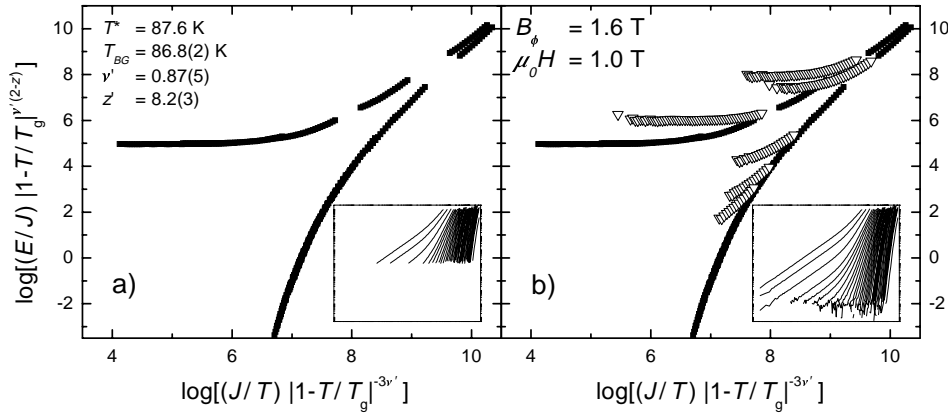
Figure 3.9: *Dependence of Bose-glass scaling analysis on the electric field range. The insets show the respective electric field ranges used for the scaling analysis.*
(a) Reduced electric field range 10^{-5} V/m $< E < 10^{-2}$ V/m: A collapse of the relevant isotherms is observed for $T_{BG} = 86.8(2)$ K, $z' = 8.2(3)$ and $\nu = 0.87(5)$, indicating together with Fig. 3.8 that the dynamic critical exponent and the Bose-glass temperature depend on the electric field range.
(b) Full electric field range $3 \cdot 10^{-8}$ V/m $< E < 10^{-2}$ V/m: The same scaling parameters as in (a), but for the extended electric field range. The additional data (open triangles) don't collapse onto the scaled curves.

these cases were twinned crystals [102], single crystals [103], melt textured and polycrystalline samples containing columnar defects [104,105] or epitaxial thin films with columnar defects [106].

For both analyzing methods of the measured CVCs the extracted z' is systematically higher compared to the results reported in the mentioned works. This observation is independent from the irradiation dose and is already known from the pristine sample, where the high dynamic exponent was attributed to the enlarged electric field range [12]. In order to check the influence of the electric field range the scaling analysis was also performed for a limited range of E. In contrast to the analysis shown in Fig. 3.8 where electric fields $3 \cdot 10^{-8}$ V/m $< E < 10^{-2}$ V/m are taken into account, the scaling analysis illustrated in Fig. 3.9(a) is restricted to a range 10^{-5} V/m $< E < 10^{-2}$ V/m. Again the scaling appears to be excellent, but compared to the full range analysis the dynamic critical exponent as well as the Bose-glass temperature have drastically changed. The glass temperature is increased by 1 K to $T_{BG} = 86.8(2)$ K, whereas z' is reduced by more than a factor 2 to $z' = 8.2(3)$. The static exponent remains unaffected of this range limitation as one would expect from the universal character of the scaling analysis. But a lack of this universality is manifested in the dependence of z' and T_{BG} from the E-range. Figure 3.9(b) underlines this observation. The data of the CVCs for $3 \cdot 10^{-8}$ V/m $< E < 10^{-5}$ V/m are added to the scaling of Fig. 3.9(a) yielding an unsatisfying result. Using the parameters obtained for the scaling of the reduced

measurement window , the additional data do not fit to the scaled curves as one would expect if the scaling ansatz is a universal one. Unfortunately the method of crossover current densities cannot be applied in the case of a limited E-range. The insets of Fig. 3.9 show that the determination of $E_x^+(J_x^+)$ line using Eq. (3.6) is not possible in this case because only a few isotherms show the crossover from a linear CVC to a asymptotic behavior.

Thus, the experimentally determined value for the dynamic critical exponent strongly depends on the electric field range chosen for the scaling analysis, as in the case of the pristine sample. The extension of the CVC measurement window leads to a lower glass transition temperature and a larger dynamic critical exponent in all cases. The reasons for this discrepancy to common results cannot be found in a reduced quality of the scaling analysis. Considering a large electric field range implies that adjacent $E(J)$ isotherms will overlap over a wide region of the scaled representation of Fig. 3.8. As a consequence the obtained parameters should be much more reliable compared to the scaling of a restricted E-range and an enlarged electric field window will sustain the power law behavior of the $E(J)$ curve at T_{BG} described by Eq. (1.24) over a wider range. In addition, a variation in one of the three parameters changes the quality of the scaling drastically as shown by Wöltgens *et al.* [107]. Finally, the scaling results presented in this work are based on two methods which yield similar scaling parameters. Due to this facts it can be assumed that the scaling procedure shown here for the large measurement window produces results of high quality and reliability.

In conclusion, the influence of the scaling parameters on the electric field range disagrees with the universality of the scaling ansatz. As the critical exponents and T_{BG} describe the transition from a liquid to a glassy state it is difficult to understand why this transition should depend on the measurement window. In order to elucidate this problem the magnetic field dependence of the critical exponents was also investigated. The above described scaling procedure as well as the crossover current density method were performed for magnetic fields 0.01 T < $\mu_0 H$ < 4 T and all irradiation doses listed in table 3.1. For $B_\phi = 1.6$ T the respective results are summarized in table 3.3. Both methods provide consistent scaling parameters and in particular the transition temperatures following from both methods are nearly equal.

The magnetic field dependence of the of the critical exponents is a further indicator for the universality of the scaling ansatz. It is shown in Fig. 3.10 for the dynamic critical exponent for the pristine sample and after the first two irradiations. Due to the mathematical equivalence between the Bose-glass and the vortex-glass model, z' represents the left axis, while the corresponding z resulting from a vortex-glass scaling analysis is shown on the right axis. Equation (1.30) connects both quantities. The magnetic field behavior of z was already discussed by Voss-de Haan *et al.* [12,21]. One should expect that z is independent of the

Table 3.3: *Analysis of the CVCs for the sample Y 12 10 98 for $B_\phi = 1.6$ T. Critical exponents and the Bose-glass temperature were obtained using the scaling ansatz (1.21) and the method of crossover currents.*

$\mu_0 H$ (T)	Scaling analysis			Crossover method	
	T_{BG} (K)	ν'	z'	T_{BG} (K)	z'
0.03	86.9(1)	0.95(1)	19.3(2)	86.9(1)	26.1(3.4)
0.06	86.8(1)	0.92(5)	19.1(3)	86.8(2)	
0.1	86.9(1)	0.90(9)	17.5(1)	86.3(2)	24.1(1.8)
0.3	86.6(1)	0.93(2)	17.4(1)	86.5(1)	18.4(1.5)
0.6	86.3(2)	0.90(9)	17.5(1)	86.1(1)	20.6(1.6)
1.0	85.8(2)	0.98(5)	17.8(3)	85.9(1)	18.2(0.3)
1.3	85.5(1)	0.99(1)	17.0(2)	85.9(1)	13.8(0.7)
1.6	85.1(1)	1.06(2)	15.8(2)	85.2(1)	14.9(0.9)
2.0	84.1(1)	1.19(4)	15.5(2)	84.4(1)	14.1(0.6)
4.0	79.7(3)	1.57(4)	14.1(2)	80.8(2)	11.7(0.4)
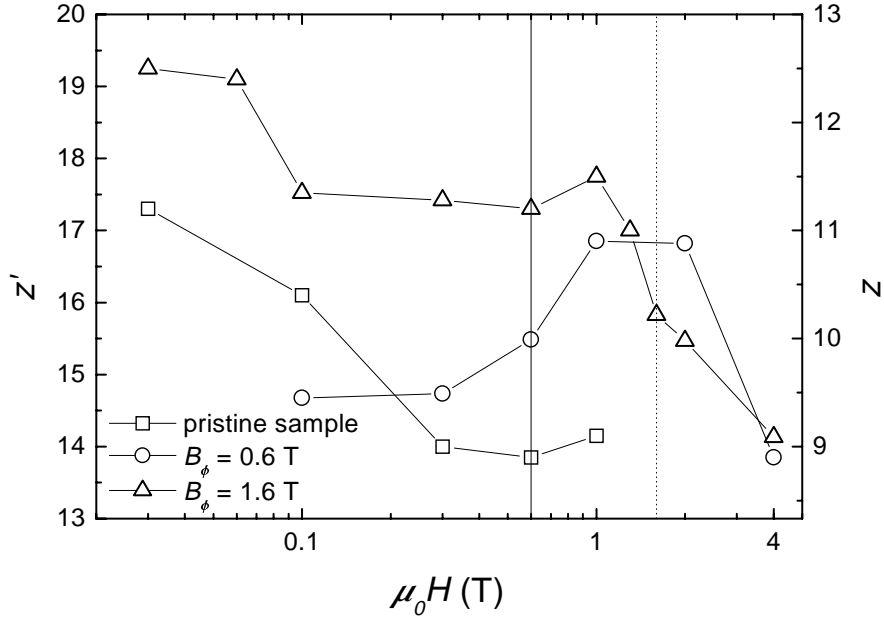
Figure 3.10: *Magnetic field dependence of the dynamic critical exponent. The left axis shows z', whereas the vortex-glass exponent z is plotted on the right axis. Vertical lines indicate the respective matching fields $B_\phi = 0.6$ T (solid) and $B_\phi = 1.6$ T (dashed). A noticeable magnetic field dependence is observed. Data of the pristine sample were taken from [21].*
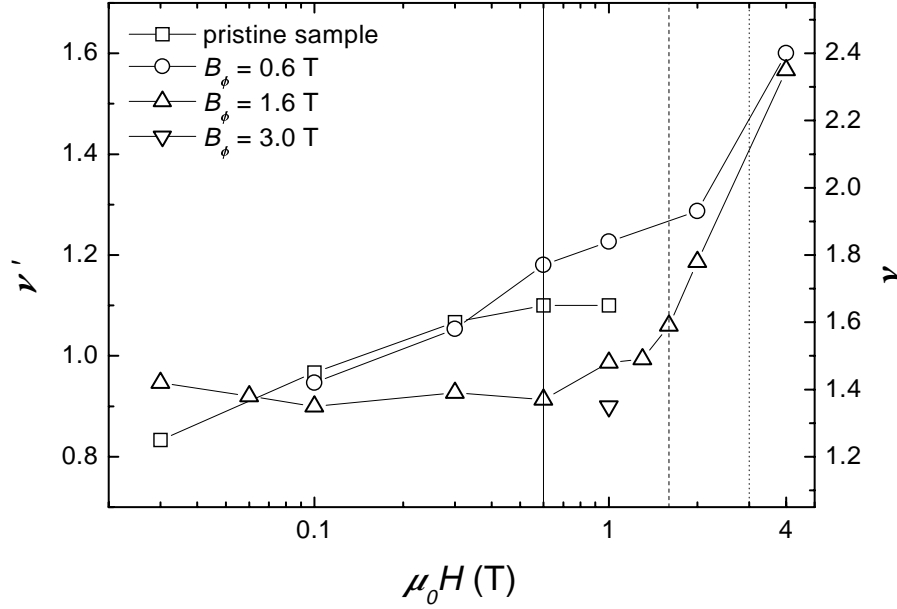
Figure 3.11:   *Magnetic field dependence of the static critical exponent. The left axis shows the Bose-glass exponent ν', whereas the vortex-glass exponent ν is plotted on the right axis. The vertical lines indicate the respective matching fields $B_\phi = 0.6$ T (solid), $B_\phi = 1.6$ T (dashed) and $B_\phi = 3.0$ T (doted). The observed behavior indicates a crossover from Bose-glass to vortex-glass with increasing field. Data of the pristine sample were taken from [21].*

magnetic field indicating the required universality. But it is obvious that the vortex-glass dynamic critical exponent decreases with increasing field. A similar behavior is found for z' in the irradiated samples. For $B_\phi = 1.6$ T this tendency is rather clear: in the low field regime the slope of this decrease is weak, whereas for $B \approx B_\phi$ (vertical lines) a stronger field dependence is observed. At high fields $B > B_\phi$ the dynamic critical exponent assumes a value $z \approx 9$ and/or $z' \approx 14$. Thus it appears that the dynamic critical exponent depends on the magnetic field and the electric field range so that the universality of the scaling ansatz can be doubted.

The situation is different for the magnetic field behavior of the static critical exponent ν'. It is shown in Fig. 3.11 in the same representation that was chosen for $z'(\mu_0 H)$, enabling to compare the Bose-glass and vortex-glass cases. Again a weak field dependence is found for low magnetic fields $B \ll B_\phi$. For an equivalent field of 1.6 T, ν' remains constant up to a field $B \approx B_\phi$ and increases sharply for higher magnetic fields. The results for the lower ion dose show a comparable behavior and even in the case of the highest irradiation dose the data point[3]

---

[3]Unfortunately a successful scaling analysis of the sample irradiated with $B_\phi = 3.0$ T could be performed only for one single magnetic field value.

plotted for $B < B_\phi = 3.0$ T is consistent with $\nu' \approx 1$. An increase of the static critical exponent is also observed in the low field regime ($\mu_0 H < 0.3$ T) of the unirradiated sample. Its value assumes a maximum value $\nu \approx 1.6$ for higher fields. In contrast to the rather strong magnetic field dependence of z' which indicates the disagreement with the universality of the scaling ansatz, the observed weak magnetic field behavior of ν' and ν below B_ϕ and in the unirradiated case would support the prediction of a universal scaling ansatz.

Compared to the theoretical predictions [19] illustrated in Fig. 3.12, the magnetic field dependence of the critical exponents shows a similar behavior: as the magnetic field is increased from $B \le B_\phi$ to $B > B_\phi$, the dynamic critical exponent should decrease whereas the static critical exponent should increase. Although the values for z' and z are larger than theoretically predicted, the observed magnetic field dependence indicates this crossover from the Bose-glass to the vortex-glass phase. Therefore the right ordinates of Figs. 3.10 and 3.11 are labeled with the respective critical exponents of the vortex-glass case. For high magnetic fields the number of vortices exceeds the number of columnar defects so that only a part of the flux lines is directly pinned by the columnar defects, whereas the remaining vortices are localized at positions between the columnar tracks due to the interaction with the strongly pinned flux lines. Radzihovsky expects that these vortices form an interstitial liquid (IL) that will freeze into a weakly pinned Bose-glass phase [108]. The pinning potential felt by intermediate flux lines is significantly weaker compared to the potential of the columnar defects [109]. Due to this two Bose-glass phases, the corresponding CVCs should be characterized by a depinning of the weakly pinned flux lines at lower currents and a second depinning of the stronger localized vortices at high currents. However, this additional features for magnetic fields $B > B_\phi$ are not detected in the CVC measurements performed in this work. Beside columnar defects, the irradiated thin films under investigation also contain randomly distributed point defects (quenched point disorder) representing additional uncorrelated pinning centers that act on the intermediate flux lines. According to this, the predicted sharp transition from a Bose-glass into the IL phase would more likely show a Bose-glass to vortex-glass transition so that the samples behave similar to the unirradiated ones for $B \gg B_\phi$. Especially the characteristic magnetic field dependencies of z and z' support this assumption.

Nevertheless, the controversy between the experimentally found high dynamic critical exponent and the predicted lower value remains an open question. In the case of the pristine sample some alternative models are discussed in order to explain the deviation of z from other results which agree with the theoretical predictions [21]. Finite size effects can be excluded, because such effects have only been observed for reduced film thicknesses $t \ll 100$ nm [107,110]. An inhomogeneous sample quality can also be excluded as the reason for the high z' due to the
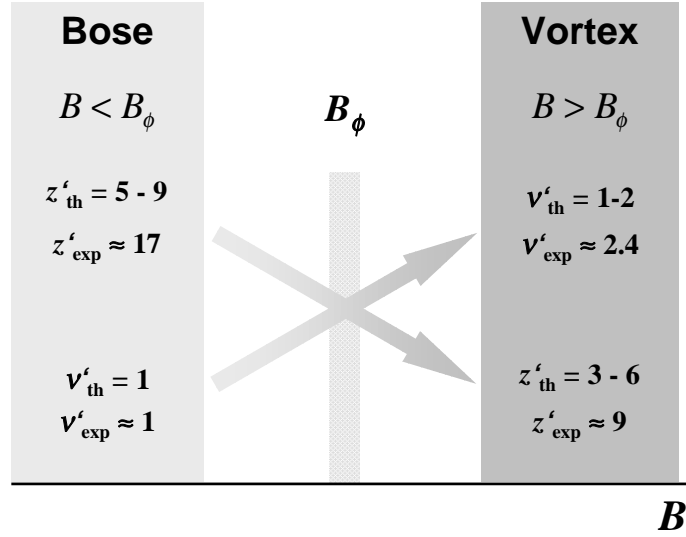
Figure 3.12:   *Critical exponents in the Bose-glass and vortex-glass phases. The corresponding subscripts indicate whether the values are theoretical predictions ($z_{\mathrm{th}}, \nu_{\mathrm{th}}$) [19] or experimentally deduced results ($z_{\mathrm{th}}, \nu_{\mathrm{th}}$). From this point of view a crossover from Bose-glass to vortex-glass with increasing magnetic field seems to be probable.*

fact that a qualitatively good scaling analysis on CVCs measured on such long bridges only is possible if the sample homogeneity is nearly perfect. Figure 3.2 shows that the resistive transition is broadened for an ion dose equivalent field $B_\phi = 3$ T. The large $\Delta T_c = 2.49$ K in this case indicates a reduced homogeneity of the superconducting properties which makes it nearly impossible to perform a successful scaling analysis. For lower ion doses this problem is absent and in consequence the scaling analysis was carried out successfully. Finally the flux creep model [18] can be used to explain the transport data. Based on this model a vortex-glass scaling analysis yields $z = 13.5$ and $\nu = 0.6$ [111]. In order to access a larger dynamic region of the $E(J)$ characteristics Wen *et al.* [112] combined dc-transport and magnetic relaxation measurements on unirradiated samples and supposed that the vortex-glass phase only exists at high current densities while the flux motion changes from collective creep or glassy motion to a thermally activated flux-flow at low J. This model can also be transferred to the irradiated case because TAFF can also be a possible vortex motion as shown in chapter 1, but nevertheless it can be excluded as an explanation for the deduced high dynamic critical exponent here. As in the pristine case, the consistency between the method of crossover current densities and the scaling analysis over the whole E field range does not indicate at all a positive curvature of the CVCs in the

Bose-glass phase at low current densities. Thus the assumption of the flux creep model in this context is not suitable.

An interesting ansatz to solve the still open problem of high z' and z is given by Minnhagen *et al.* [113]. They give evidence for two distinct dynamic critical exponents in connection with vortex physics. Due to a weaker dynamic universality compared to the static behavior, two competing models with different z describe the dynamic critical behavior of a vortex system. For HTSC consequently, the possibility of two critical dynamic exponents would have to be taken into account when analyzing CVC experiments. However a criterion to distinguish these exponents remains to be found.

Thus, although the scaling analysis of the CVCs shows the required collapse of the measured data, the remaining problems indicating a lack of universality should not be neglected. Current publications suggest that true evidence for a glass transition has not yet been demonstrated through CVCs [28]. The criterion to proof the existence of the glass phase is that the positive curvature of the CVCs for $T > T_G$ and the negative curvature for $T < T_G$ must be measured at the same current density. This requires the measurement over an electric field range that must be even larger than the accessible measurement window achieved with the method of long measurement bridges.

3.4.2 Irreversibility Line

In the framework of the vortex-glass and Bose-glass models the applied scaling analysis can be used to determine the characteristic fields and temperatures of HTSCs to construct a phase diagram. As the glass temperature defines the transition into a true superconducting phase the $(H,T)_G$ line represents such a characteristic feature and can be interpreted as the irreversibility line [32]. In the context of magnetization measurements the irreversibility line is defined as the line that separates the region near T_c in the (H,T)-plane in which the sample shows a unique reversible magnetization $M(H,T)$ from the region in which $M(H,T)$ depends on the previous path in the (H,T)-plane [114].

Figure 3.13 represents the irreversibility line of the pristine as well as of the irradiated sample obtained from scaling analysis in a semi logarithmic plot. For the determination of the glass transition temperature T_G the corresponding analysis were performed over a large electric field range as described in the previous section. The strong pinning efficiency of correlated disorder that shifts the irreversibility line towards higher temperatures is clearly visible for high magnetic fields [115]. This shift is most distinct for magnetic fields in the range of B_ϕ, in agreement with the result found for the analysis of the magnetic field dependence of the activation energy. The inset of Fig. 3.13 illustrates that the glass transition temperature in an external field of $\mu_0 H = 1.0$ T is increased with the irradiation
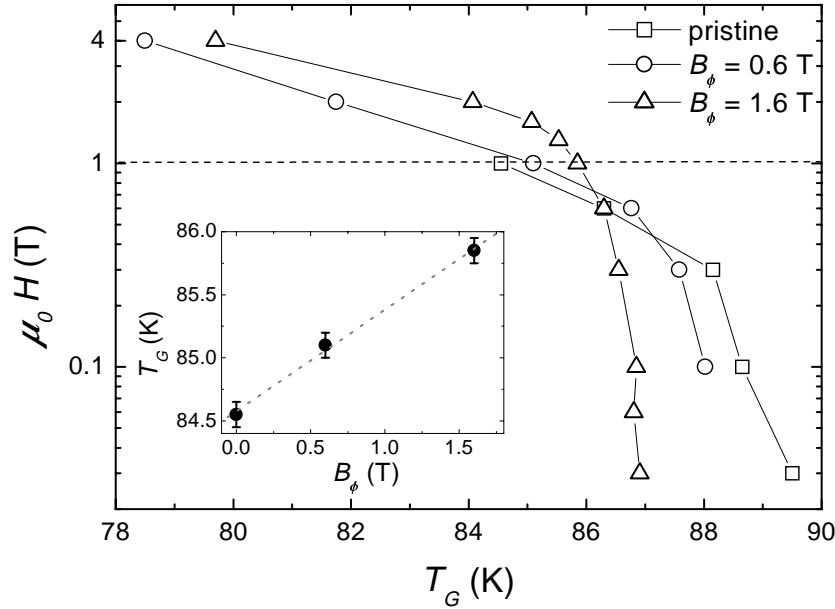
Figure 3.13: *Irreversibility lines of Y 12 10 98 before and after irradiation in a semi logarithmic representation. In the high field region the behavior of all three samples is similar, whereas the magnetic field behavior depends on the irradiation dose for low magnetic fields. The inset shows the linear dependence between the irradiation dose and the glass transition temperature for $\mu_0 H = 1$ T. Data of the pristine sample were taken from [21].*

dose from $T_{VG} = 84.55(20)$ K in the unirradiated case to $T_{BG} = 85.8(2)$ K for $B_\phi = 1.6$ T. In the low field region this shift cannot compensate the irradiation induced reduction of the zero field transition temperature T_c. But the influence of columnar defects on the dynamic properties of the vortex system in this regime is emphasized if the extension of the vortex liquid regime is considered. Assuming that the vortex liquid is limited by T_c and the vortex-glass or Bose-glass transition temperature, this phase with ΔT_{VL} is significantly reduced if the pinning potential is enhanced. Table 3.4 illustrates the shrinking of the vortex liquid phase by the introduction of correlated disorder.

In addition, two regions of the irreversibility line can be distinguished. At low fields $B \ll B_\phi$ the glass transition temperature is nearly unaffected by the increase of the magnetic field. This effect is amplified for higher ion dose equivalent fields. The slope of the irreversibility line changes noticeably near B_ϕ and for high magnetic fields a strong field dependence is observed. Even for the unirradiated sample this change of the slope of the $(H,T)_G$ line is visible at $\mu_0 H \approx 0.3$ T. An explanation for this observation is found in the different interaction mechanisms of vortices at fields well below and above the matching field. At low magnetic fields the number of columnar defects is much larger than the number of vortices and all

Table 3.4: *Vortex liquid regimes in* $YBa_2Cu_3O_{7-x}$ *for an external magnetic field* $\mu_0 H = 1$ T *for the thin film* Y 12 10 98 *before (point disorder) and after (additional correlated disorder with* $B_\phi = 1.6$ T*) irradiation. The borders of the liquid regime are defined by the zero field transition temperature* T_c^0 *and the corresponding glass transition temperatures* T_G.

	As grown point disorder	With additional Correlated disorder
T_c (K)	89.5	88.0
T_G (K)	84.6	85.8
ΔT_{VL} (K)	4.9	2.2

flux lines will interact with the correlated pinning centers. As in the discussion of the magnetic field dependence of the activation energy (see Fig. 3.5 [100]) this case can be treated as a single vortex problem and the individual pinning and depinning properties are dominant. The interaction mechanism changes if the external magnetic field is increased above B_ϕ. In this case the number of vortices exceeds the number of columnar defects, the pinning efficiency is reduced and collective effects induced by long range vortex-vortex interactions become important [116]. The accommodation field $B^*(T)$ characterizing this change in the interaction mechanism was already introduced in section 1.3 in the context of the crossover from single vortex creep to vortex bundle dynamics for $B \geq B^*(T)$.

A power law behavior which includes the reduced temperature $t = T_G/T_c$ is used to approximate the irreversibility line [117,118]

$$H(T_G) = H_0(1 - t)^\mu, \tag{3.7}$$

and the deduced power law exponent μ provides additional information about the different phases of vortex interaction in the $(H, T)_G$ plane. The results for the different matching fields are illustrated on a double logarithmic scale in Fig. 3.14. The pristine sample is characterized by one single exponent $\mu = 1.6(2)$. This is similar to earlier results where values between $\frac{3}{2}$ [25,117] and $\frac{4}{3}$ [5,118] were found. The behavior of the irreversibility lines with increasing irradiation dose exhibits two regimes: at low fields the curvature steepens with increasing B_ϕ (μ changes from 4 to 11). At high fields the power law dependence is weaker and approaches a linear $H(T_G)$ dependence with increasing ion dose as expected for a collective pinning behavior [119]. The accommodation field $B^*(T)$ can be estimated from this representation by determining the intersection between the different power law behaviors. The obtained fields are summarized in table 3.5 indicating a reduced field compared to B_ϕ. The relative reduction to ≈ 70 % is
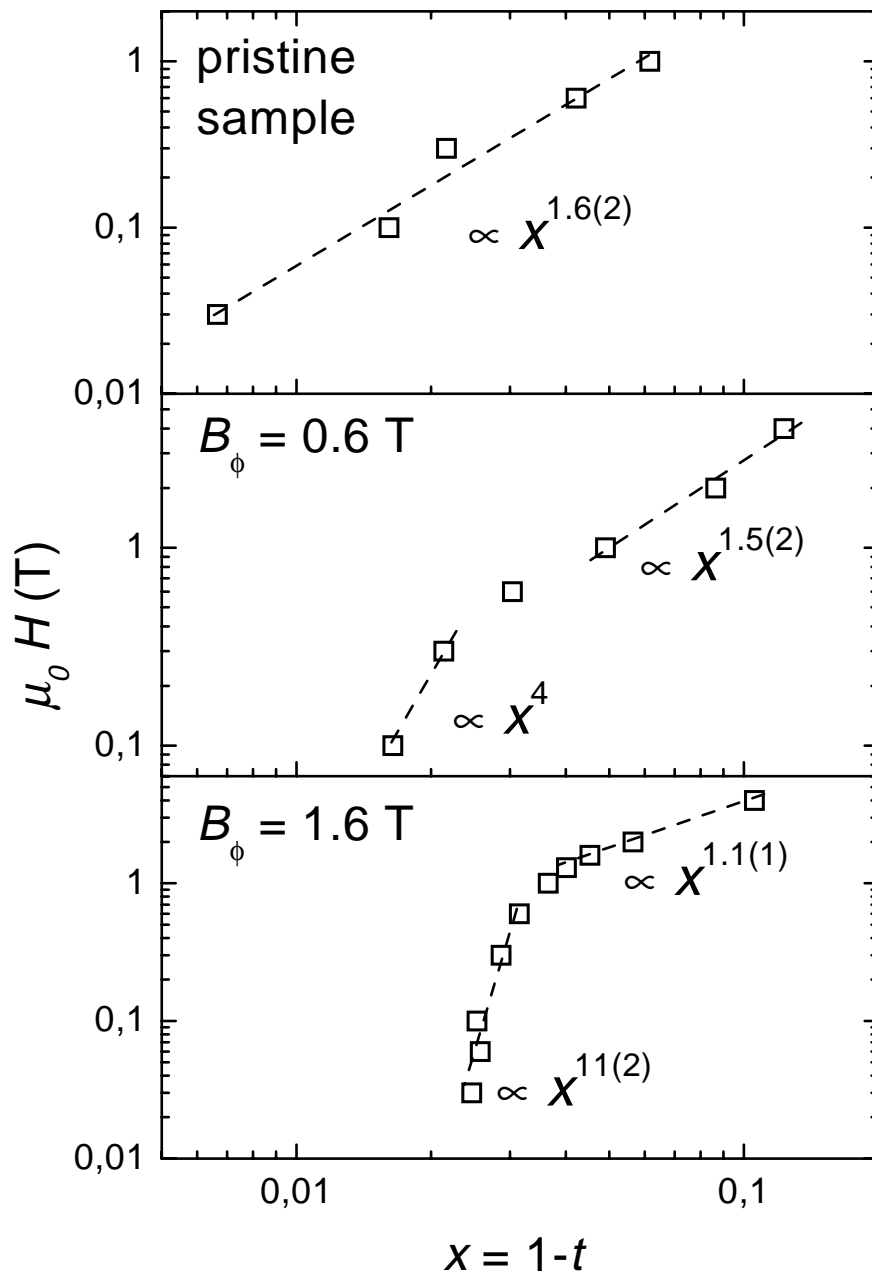
Figure 3.14:   *Scaling of the irreversibility lines shown in Fig. 3.13 using Eq. (3.7). The pristine sample shows a power law behavior with $\mu \approx \frac{3}{2}$, whereas the irradiated samples exhibit two different power law behaviors that are separated by the respective accommodation field B^*. This behavior is typical for a crossover from individual vortex pinning and depinning at low magnetic fields to collective vortex dynamics at high fields $B > B_\phi$.*

independent of the irradiation dose, implying that about 30 % of the columnar defects are not effective in this range of B_ϕ due to the superposition of the pinning potential of neighboring columnar tracks.

Table 3.5: *Determination of the accommodation field B^* from the different power law behaviors of the irreversibility lines shown in Fig. 3.13 and Fig. 3.14.*

B_ϕ (T)	B^* (T)	B^*/B_ϕ
0.6	0.44(5)	0.73(8)
1.6	1.14(2)	0.71(2)

3.4.3   Current Dependence of the Activation Energy

The investigation of the CVCs is concluded with a study of the current dependence of the activation energy $U(J)$ in the vicinity of the corresponding glass transition for the pristine and the irradiated samples. Assuming the existence of the vortex-glass as well as the Bose-glass phase, the theory predicts a diverging activation energy in the low current density limit $J \longrightarrow 0$ [5,32], in contrast to the TAFF models. Therefore, the extraction of the $U(J)$ behavior provides additional information about the characteristics of these second order phase transitions.

Following the approach of Miu *et al.* [120,121] one can determine the activation energy from the experimentally obtained $E(J)$ isotherms

$$U(J) = k_B T \frac{d\ln(E)}{d\ln(J)}. \tag{3.8}$$

The resulting $U(J)$ curves of the pristine sample are shown in Fig. 3.15 for temperatures between 80.5 K and 86.4 K. In the high temperature regime $(T > T_{VG})$, U increases with increasing current density, achieves its maximum and decreases with a power law behavior for high J. For temperatures below the vortex glass transition which is indicated by the bold curve at $T_{VG} = 84.6$ K, a decrease of the activation energy with increasing current is observed. A divergence of the activation energy on lowering the current density cannot be observed experimentally in this case due to limits in the sensitivity of the measurement. Only a saturation of the activation energy for decreasing current densities can be suggested from this illustration. This behavior can be interpreted as a vortex plastic creep [121]. However, a reliable interpretation requires the determination of the activation energy using Eq. (3.8) for much smaller current densities and electric fields at low temperatures.

A similar result is observed in the case of the irradiated sample. Figure 3.16 represents the $U(J)$ variation for an irradiation dose of $B_\phi = 0.6$ T. A maximum of the activation energy is also observed for temperatures below the Bose-glass transition temperature (bold solid line, indicated by an arrow). Compared to the pristine sample the $U(J)$ behavior does not show a divergence in the limit of low current densities for temperatures below T_{BG}. It seems to approach a $U \propto J^{+0.31}$ power law for all curves. For a matching field of $B_\phi = 1.6$ T the situation is similar and neither a divergence nor a saturation of $U(J)$ is observed. Although a scaling analysis of the *same* CVCs was performed qualitatively well, these observations dispute the Bose-glass scaling ansatz due to the missing divergence of U in the limit of low current densities.

Based on the experimental data obtained on the spiral measurement bridges, the combination of the described $U(J)$ and glass scaling analysis therefore reinforces the doubts about the existence of the vortex-glass and the Bose-glass phase.

Nevertheless, the current dependence of the activation energy allows to extract further information about the properties of the pinning barriers controlling
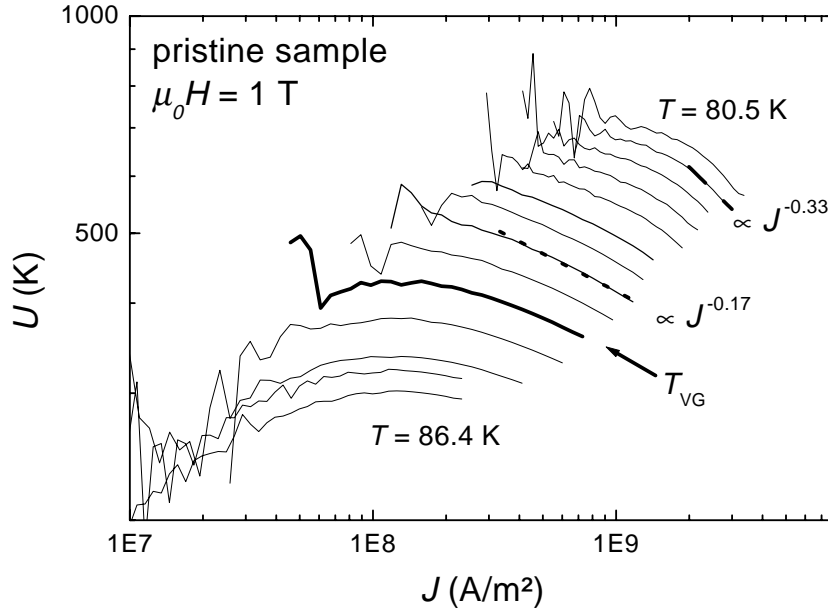
Figure 3.15:   *Current dependence of the activation energy for the pristine sample using Eq. (3.8) for $\mu_0 H = 1$ T. If the existence of a vortex-glass phase is assumed, the bold curve represents the $U(J)$ dependence at $T_{VG} = 84.6$ K. The power law behavior of the activation energy of Eq. (3.9) at high current densities is illustrated by dotted lines for $T = 81$ K and $T = 83.8$ K, respectively. The original data were taken from [21]. (T : 80.5 K, 81.0 K, 81.5 K, 82.0 K, 82.5 K, 83.0 K, 83.4 K, 83.8 K, 84.2 K, 84.6 K, 85.0 K, 85.4 K, 86.2 K, 86.4 K)*
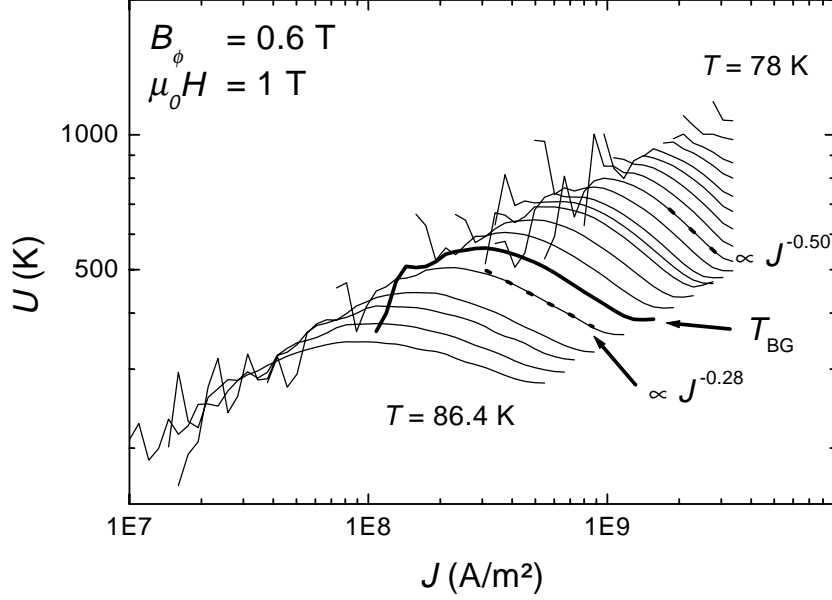
Figure 3.16:   *Current dependence of the activation energy after irradiation using Eq. (3.8) for $\mu_0 H = 1$ T. The bold curve illustrates the current dependence of U at $T_{BG} = 85$ K, if the existence of a Bose-glass phase is assumed. The dotted lines indicate linear fits of $U(J)$ in order to extract the exponent μ. (T : 78.0 K, 79.0 K, 80.0 K, 80.5 K, 81.0 K, 81.4 K, 81.8 K, 82.2 K, 82.6 K, 83.0 K, 83.4 K, 83.6 K, 83.8 K, 84.2 K, 84.6 K, 85.0 K, 85.4 K, 85.8 K, 86.0 K, 86.2 K, 86.4 K)*

the vortex dynamics at current densities $J < J_c$

$$U \propto \left(\frac{J_c}{J}\right)^{\mu} , \tag{3.9}$$

where J_c is the critical current density. In the $U(J)$ representation of Fig. 3.16 the value for J_c is visible as an upward curvature at high current densities. As an example this analysis is shown in Figs. 3.15 and 3.16 for two temperatures ($T = 81$ K and $T = 83.8$ K for the pristine, $T = 82.6$ K and $T = 85.4$ K for the irradiated sample). Figure 3.17 illustrates the temperature dependence of the exponent μ extracted from the $U(J)$ characteristics at $\mu_0 H = 1$ T for $B_\phi = 0.6$ T, $B_\phi = 1.6$ T and the pristine case, respectively. Two different behaviors are observed if the temperature is increased. The pristine sample shows a decrease of μ, whereas the irradiated samples show an increase of the exponent up to approximately 83 K and a decreasing $\mu(T)$ for higher temperatures. For the indicated temperatures the values for all extracted exponents are $\mu(T) < 1$. From the linear fits indicated by the dotted lines in Figs. 3.15 and 3.16 it is obvious that low temperatures represent high current densities and vice versa higher temperatures
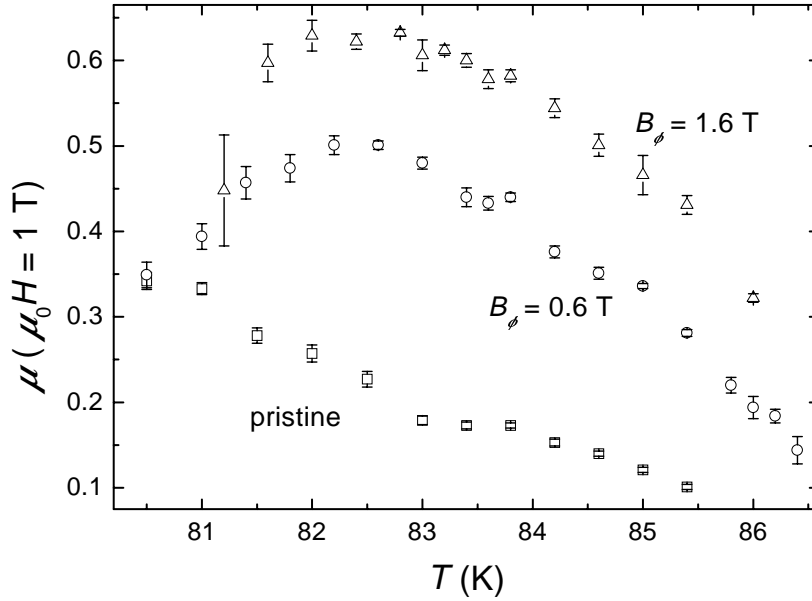
Figure 3.17:   *Temperature dependence of the $U(J)$ power law exponent μ as extracted from the previous illustrations. Squares represent the pristine samples, the irradiated cases are represented by circles ($B_\phi = 0.6$ T) and triangles ($B_\phi = 1.6$ T). The different values for μ can be attributed to different vortex creep regimes.*

denote low currents. The Bose-glass model predicts a decrease of the exponent from $\mu = 1$ at low temperatures (high currents) to $\mu = \frac{1}{3}$ on approaching T_{BG}, corresponding to low current densities.

The values for μ can be attributed to different vortex creep regimes. Following the assumptions made within the context of the glass scaling analysis in section 3.4.1, the creep mechanisms must be treated in a random pinning environment as a pinned *vortex lattice* [19] in the case of $\mu_0 H > B_\phi$. Collective vortex creep effects will play the major role in this situation. For $\mu_0 H < B_\phi$, the correlated disorder of the columnar defects must be taken into account and vortex creep must be described in the Bose-glass picture [32]. The value for μ at low temperatures is similar for all three samples. An exponent $\mu = \frac{1}{3}$ can be attributed to a variable range hopping creep regime which is interpreted as an onset of single vortex creep behavior which is considered for lower temperatures. An experimental proof of this assumption requires additional data points at higher current densities (lower temperatures), but in order to avoid the risk of sample destruction, these measurements were not carried out. The maxima of the $\mu(T)$ curves of the irradiated samples are achieved at $\mu \approx \frac{5}{8} = 0.625$ for the high ion dose and $\mu \approx \frac{1}{2}$ for the lower dose, respectively. Both values correspond to a charge density wave (CDW) like creep mechanism which is applicable in the

Bose-glass picture ($B_\phi = 1.6$ T) as well as in the framework of a pinned *vortex lattice* ($B_\phi = 0.6$ T). In this case the hopping distance u of a vortex bundle exceeds the intervortex spacing a_0 and the influence of disorder on a bundle becomes weaker [122]. For $u > a_0$, the cost in elastic energy remains the same, but the possible gain in the pinning energy is restricted, because the flux line bundle experiences the same disorder potential after a shift by a distance a_0. The temperatures at which this value of μ is achieved is lower than the corresponding transition temperatures T_{BG} deduced from scaling analysis. in addition, the value $\mu = 0.5$ was found for a pinned *vortex lattice* [123], supporting this CDW-picture. Therefore the interpretation of the data for ($B_\phi = 0.6$ T) in this sense is suitable. Furthermore these results are in qualitative agreement with the predictions made in the context of the theory of collective vortex bundle pinning (cf. chapter IV.B.3 of Ref. [19]). On approaching the high temperature regime near T_c the extracted exponents of the $U(J)$ power law behavior seem to approach $\mu \longrightarrow 0$ indicating a current independent activation energy. In addition, the measured CVCs illustrated in Figs. 3.6 and 3.7 indicated that the vortex systems shows a free flux flow behavior in the high temperature region, underlining $\mu = 0$ for $T \longrightarrow T_c$.

3.5 Concluding Remarks

In summary, the investigation of the CVCs of the irradiated thin film Y 12 10 98 showed that it is possible to describe the experimental data within the framework of the Bose-glass theory. A scaling analysis of an enlarged $E(J)$ window allowed the deduction of the critical exponents which describe the Bose-glass phase transition. However, the obtained results give indications for the lack of universality of this model. While the static critical exponent ν' is independent of external magnetic field and measurement window for $\mu_0 H < B_\phi$, the dynamic exponent shows this dependence as in the case of the pristine sample. The additional crossover current density analysis confirms the obtained scaling results for T_{BG} and z'. Alternative models cannot explain the existence of an increased dynamic critical exponent indicating that a scaling approach cannot entirely describe this liquid-to-glass transition. It will be necessary to enlarge the experimentally accessible window in order to improve the scaling analysis. Apart from this an improved experimental sensitivity of the CVCs is required to obtain a clearer experimental evidence for the glass phase [28]. This aspect was also pointed out in the context of the current dependence of the activation energy. Measurement techniques providing a further increase of the electric field sensitivity in the limit of low current densities are required.

However, two regimes can be distinguished in the analysis of the magnetic

field dependence of z', ν' and T_{BG}. The value of both critical exponents changes remarkably if the magnetic field is increased over the matching field. This change is in agreement with the theoretically determined critical exponents considering a crossover from Bose-glass at low fields to vortex-glass at fields $\mu_0 H > B_\phi$. Such a behavior requires a change in the universality class [124] in order to describe the vortex system in the two different field regimes. The suggestion of a Bose-glass to vortex-glass crossover is supported by the behavior of the irreversibility line which is also divided into two magnetic field regimes, separated by the accommodation field $B^* \approx 0.7 B_\phi$. Interactions between vortices and columnar defects characterize the vortex dynamics in the low field regime, whereas vortex-vortex interactions dominate the dynamics at high magnetic fields. This change in the interaction mechanisms can be understood as a transition from a single vortex pinning regime to a collective vortex pinning behavior. First investigations of the current dependence of the activation energy supported this assumption, indicating that additional measurements at higher current densities and low temperatures are necessary to complete the picture of collective vortex bundle pinning.

In consequence the efficiency of the correlated pinning centers is strongly reduced for $\mu_0 H > B_\phi$ and the vortex bundles describing the collective regime "feel" the columnar tracks acting in the sense of a pointlike defect and thus the vortex dynamics will be described more appropriately with the vortex-glass scaling ansatz.

In this chapter it was pointed out that the interplay between the strong pinning Bose-glass phase and the "weak" pinning vortex-glass, phase i.e. the ratio between an externally applied magnetic field and the density of columnar defects, must be taken into account when analyzing the vortex dynamics with respect. Accordingly, the investigation of the interface between strong and weak pinning regions is an interesting task and will be the topic of the following chapters.

Chapter 4

Patterned Irradiation of HTSC Thin Films

4.1 Key Ideas

Apart from columnar defects, twin boundaries form a second class of correlated disorder. Their influence on the vortex dynamics was extensively studied during the last years in $YBa_2Cu_3O_{7-x}$ single crystals with unidirected twin boundaries using electrical transport measurements [125–130], ac screening experiments [131,132], simulations [133] and analytical methods [134–138]. For the case that the twin boundaries form an angle θ with the direction of an applied external current, the vortices are exposed to an anisotropic pinning force, in contrast to pointlike pins or columnar defects aligned along the magnetic field direction that are characterized by an isotropic pinning force. Figure 4.1 illustrates the twin boundary pinning forces acting on a vortex in the presence of a transport current density $\mathbf{j}$ (or J) for $\theta = 45°$. The induced Lorentz-force is balanced by the pinning force $\mathbf{F_p}$ that can be divided in two parts. Due to the planar pinning potential of the twin boundary, vortices are exposed to a large pinning force $\mathbf{F_p^{\perp}}$ in the direction perpendicular of the twins. In the parallel direction along the twin boundaries pinning only results from point defects and $\mathbf{F_p^{\parallel}}$ is considerably weaker. This leads to a guided vortex motion that can be detected in measuring the even transverse voltage – with respect to the field direction – in the presence of an external magnetic field [139]. In literature, two different mechanisms are proposed to be responsible for the guided motion of vortices in unidirected twins [133]. In the first, vortices will be channeled by the deep pinning potential of the twin boundary and will move only within the twin boundary (internal motion), whereas the second mechanism assumes the vortex-vortex interaction to be the dominating mechanism for a guided vortex motion inside and also outside the twin boundaries (external motion).
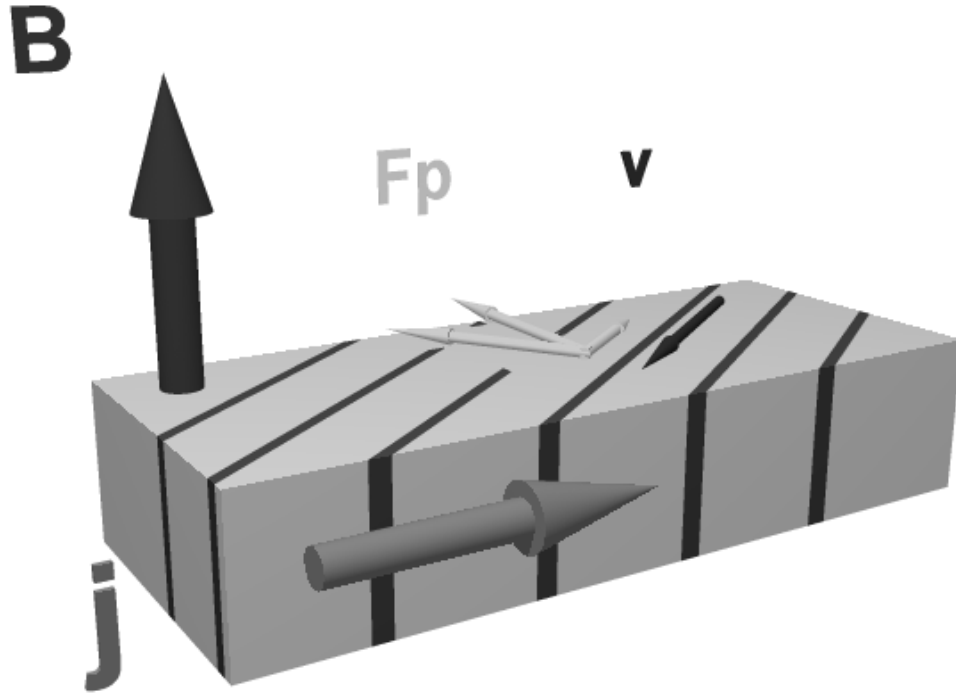
Figure 4.1:   *Illustration of the anisotropic pinning forces in a single crystal with unidirected twin boundaries. The component of the pinning force across the twin boundary is stronger than the parallel component. The external magnetic field is directed parallel to the crystallographic c-axis of the single crystal.*

In the following, an experiment using an arrangement of strong and weak pinning regions is presented and its relation to the guided vortex motion in single crystals containing unidirected twin boundaries is discussed. Channels of different pinning strength were created in $YBa_2Cu_3O_{7-x}$ thin films using heavy ion irradiation through metal masks consisting of an array of fine stripes in order to obtain a pinning arrangement that is similar to twin boundary experiments. The effects of homogeneous irradiation are analyzed using irradiated and unirradiated reference bridges on the same sample. The transverse voltage on a Hall-bar structure shows a strong correspondence to that in $YBa_2Cu_3O_{7-x}$ single crystals with unidirected twin boundaries. However, in this experiment the weak pinning channels have a macroscopic width in contrast to the very narrow channels between the twin boundaries. This results in a nontrivial current density distribution in the samples that is modeled using the longitudinal resistivities. In addition, the different pinning properties of twin boundaries and columnar defects yield different reasons for the guided motion of vortex. Flux lines tend to move parallel to the twin boundaries due to the anisotropic properties of these planar pinning centers. In the case of a patterned irradiation the columnar defects are linelike

pinning centers which excert an isotropic pinning force on the vortices. Therefore a guided vortex motion can only result from vortex-vortex interaction at the interface of strong and weak pinning regions. If the interaction length increases, the pinned vortices in the irradiated channels should induce a freezing of weakly pinned vortices in the unirradiated channels. At this freezing transition a guided vortex motion must vanish. Thus, the arrangement of strong and weak pinning regions represents a Bose-glass contact [13,140] which was already discussed in chapter 1.

The CVCs of both test bridges were additionally investigated in order to study the correlations between the even transverse voltage and the Bose-glass transition.

4.2   Sample Preparation

The thin films have been prepared, characterized and photolithographically patterned as reported in chapter 2. The resulting structures consist of a conventional Hall-structure (2 mm $\times$ 7 mm) and two identical test bridges (200 μm $\times$ 2000 μm). The samples were irradiated with 0.75 GeV Pb-ions and 1.14 GeV U-ions, respectively, in such a way that columnar defects were arranged in a periodic array of strong (irradiated) and weak (unirradiated) pinning regions. Differently patterned 0.5 mm thick Ni-masks were used to stop the swift ions and to reproduce the irradiation pattern on the thin film structure. A picture of such a mask prepared with the spark erosion technique is shown in Fig. 4.2.

Two arrangements were used in this experiment which differ only in the width of the irradiated channels that is 700 μm (1:7 ratio) and 400 μm (1:4 ratio) respectively, whereas the width of the weak pinning channel is 100 μm for each case. The angle θ between the edges of the Hall-structure and the direction of the weak pinning channels is $\theta = \pm 45°$. In addition, one test bridge was fully irradiated with the same ion dose ($B_\phi = 1.0$ T $\cong 5 \cdot 10^{10}$ Ions/cm^2) as the Hall-structure.

Table 4.1:   *Summary of the geometry parameters as well as of some superconducting properties in zero magnetic field for the samples used for the patterned irradiation. The superconducting properties were measured on the corresponding test bridges.*

	1:4 ratio structure		1:7 ratio structure	
	unirradiated	irradiated	unirradiated	irradiated
w_{channel} (μm)	100(10)	400(10)	100(10)	700(10)
B_ϕ (T)	0	1	0	1
T_c (K)	90.0	89.9	91.5	91.1
ΔT_c (K)	1.6	1.2	0.5	0.8

Sample and irradiation geometry are sketched in Fig. 4.3 for the Hall-structure with the 1:7 ratio. The 1:4 ratio structure was realized on a second $YBa_2Cu_3O_{7-x}$ thin film. The observed qualitative behavior was identical for both samples, showing sharp resistive zero field transitions for both, the irradiated and unirradiated test bridges with critical temperatures between $T_c^{1:4} \approx 90$ K and $T_c^{1:7} \approx 91.5$ K. Characteristic geometries and the superconducting properties of both samples are summarized in table 4.1.

The efficiency of the metal masks in the patterned irradiation was analyzed using glass substrates that were irradiated through the masks with a dose of approximately $3 \cdot 10^6$ Ions/cm^2. To visualize the defects, the glass substrates were etched with 18% HF acid for 20 s. A result of this procedure is shown in Fig. 4.4 for the 1:7 ratio structure. The width of the weak pinning channels is 110 μm, the periodic length of the irradiation pattern is 820 μm. Higher image resolutions show that the defect concentration has a steplike behavior at the interfaces between strong and weak pinning. Less than 2% of the ions are scattered in a 5 μm wide region of the unirradiated channels in both experimental arrangements.

Measurements of the voltage drop across different contacts of the Hall-structure were performed for temperatures from 70 K to 300 K and magnetic fields up to 12 T at a constant current density of $J = 125$ A/cm^2. The various contacts allow
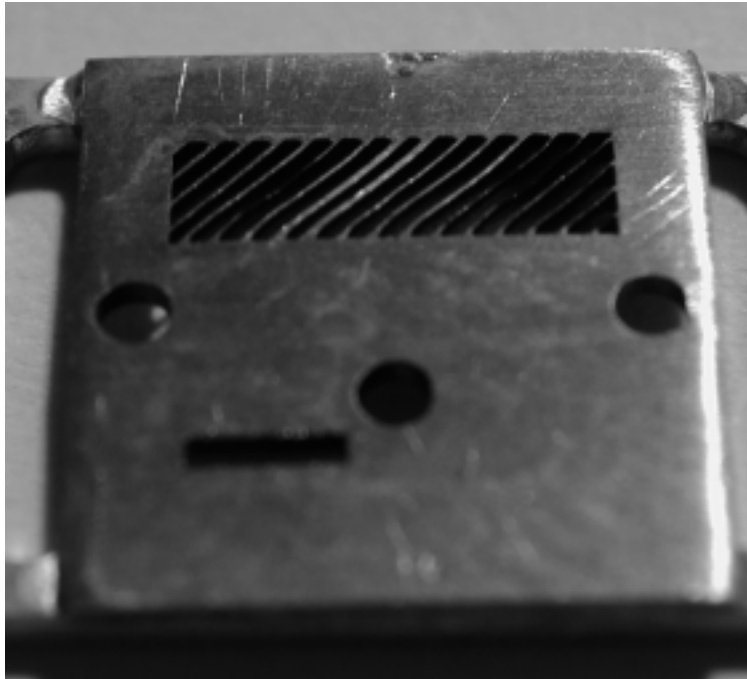
Figure 4.2:   *Image of the Ni-mask used for patterned irradiation of the 1:4 ratio structure. In this case 100 μm wide weak pinning channels and 400 μm wide strong pinning channels are generated. Ions are stopped by this mask, except in the dark regions. The tree circles in the middle of the mask are used for a positional adjustment. Mask prepared by H. Lott.*
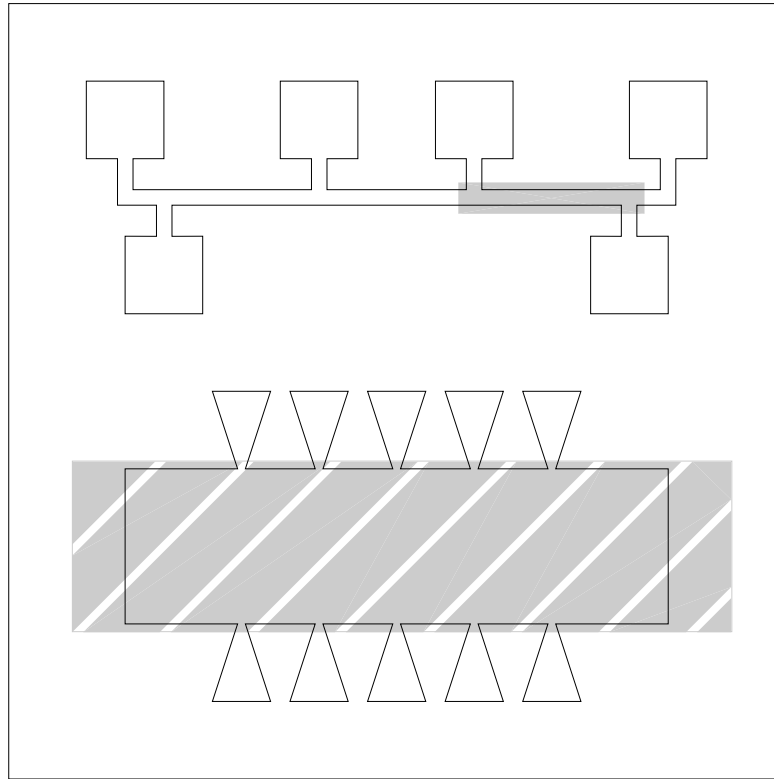
Figure 4.3: *Sample and irradiation geometry of the 1:7 ratio structure. The upper part shows the two test bridges. Gray regions are irradiated. The Hall-bar structure consists of 10 probes in order to measure the voltage in longitudinal as well as in transverse direction. The current is applied trough evaporated and diffused rectangular gold contact pads on the left and right side of the Hall-structure.*
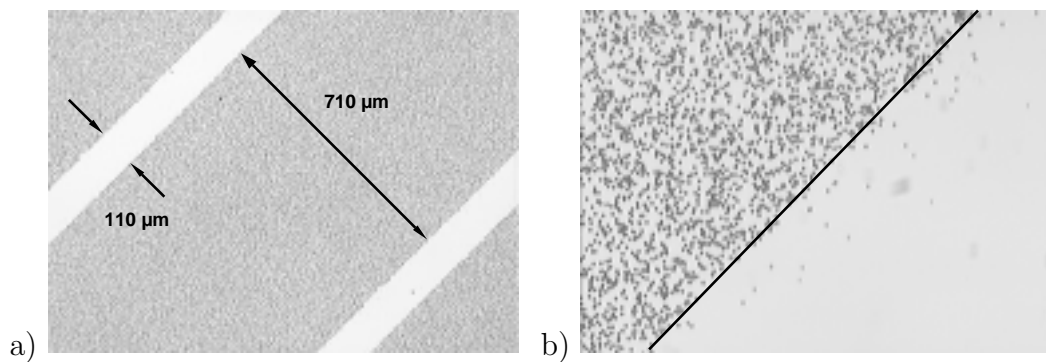
Figure 4.4: *Image of an irradiated glass substrate (dose:* $3 \cdot 10^6$ *Ions/cm^2) that was etched in 18% HF acid for 20 s.*
(a) For the structure with the 1:7 ratio that is shown here, the channel width is 110 μm for the unirradiated and 710 μm for the irradiated regions.
(b) Higher resolution illustrate that the interface between irradiated and unirradiated regions is very sharp and can be described by a wall-like defect distribution.

to measure the voltage drop in different directions with respect to the direction of the weak pinning channels and the external current. In addition, the two parts of the test bridge allow to determine in parallel the voltage drop over a completely irradiated and unirradiated part of the sample for all parameters used in the measurement.

4.3   Modeling of the Irradiated Structure

The results obtained for both parts of the test bridge represent the input values for different methods of modeling the periodically irradiated Hall-structures with the different arrangements. Two methods were applied during this work in order to compare the measured with the calculated results. The scaled resistor network representation of the Hall-structure is the first method to be described in the following. In addition an effective medium approach was used to model the system. This approach was carried out for $YBa_2Cu_3O_{7-x}$ single crystals with unidirected twin boundaries [128] and was applied here to calculate transverse and longitudinal voltages and to crosscheck these results with those obtained with the network calculation.

4.3.1   Network Calculations

For the scaled resistor network representations the samples are modeled by dividing Hall-structure and reference bridges into areas of $25 \times 25~\mu m^2$. Each element is replaced by a square of resistors sharing common edges. In the Hall-structure there exist two values for the resistors, depending on the respective state of irradiation at the resistors' position. At given values of magnetic field and temperature these two values are determined from the measured area resistivities of the irradiated and unirradiated test bridge, respectively. Kirchhoff's laws were solved by numerical inversion of a 22401×22401 matrix representing a set of independent current loops around each area element of the Hall-structure. As each area is connected to at most 4 neighbors the matrix can be constructed to be sparse containing only about 110000 nonzero elements. This allows an efficient solution on a personal computer and to calculate the potential distribution across the Hall-structures. An example for such a calculation is given in Fig. 4.5 where the potential distribution of the 1:4 ratio structure is shown for a ratio between the resistance of the unirradiated parts R_{unirr} and the irradiated regions R_{irr} of $R_{\mathrm{unirr}}/R_{\mathrm{irr}} = 100$. Due to the different resistances a steplike behavior of the potential drop which reproduces the periodic arrangement of the strong and weak pinning channels is observed. The plateaus where the potential is nearly constant in this illustration represent the regions of $R_{\mathrm{irr}} = 0.01~\Omega$.

The potential distribution at the borders of the Hall-structure was calculated at each value of temperature and magnetic field. Subsequently the voltages between different probes were extracted from the border potentials and compared with the measured results. An important point to mention here is that the irradiated and unirradiated channels cover the full width of the Hall-structure. Thus, the current is enforced to cross the channels and the current density is identical in the irradiated and unirradiated channels aside from small edge effects. Therefore nonlinear effects in the CVCs are taken into account by using identical current densities for the reference bridges and the Hall-structures. Another advantage of this experimental set is the possibility to measure the CVCs of both, the unirradiated and irradiated part of the film. Based on this information one can carry out a glass analysis in order to determine the characteristic fields and temperatures of the vortex dynamics for both test bridges.

Alternatively to the above described method a finite element calculation [141] yield comparable results. An advantage of such a method is that lateral resolu-
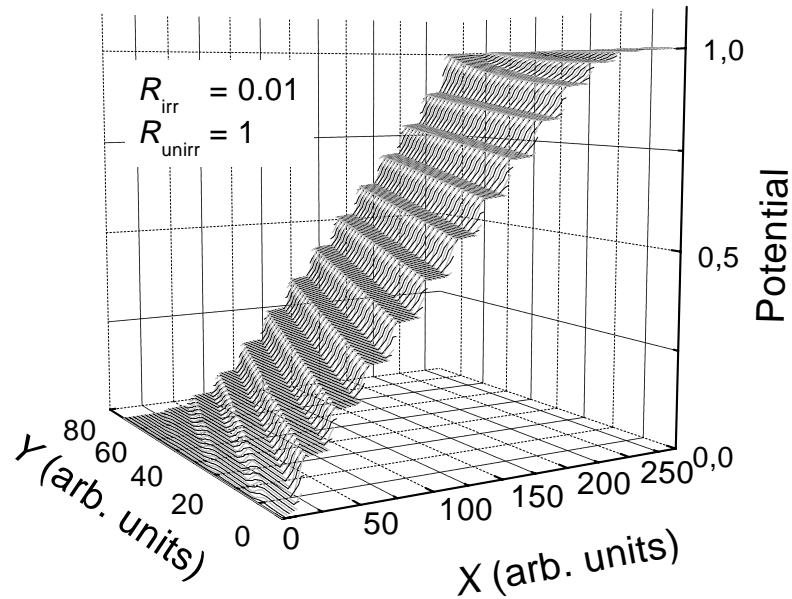
Figure 4.5: *Calculated potential distribution across a periodically irradiated Hall-structure (1:4 ratio) using the resistor network calculation. In this example the resistance of the irradiated regions R_{irr} is by a factor 100 lower than the resistance of the unirradiated parts R_{unirr} yielding a steplike behavior. The potential drop mainly takes place in the unirradiated regions. The X and Y axis represent the length and the width of the Hall-array. One length unit is equal to 25 μm.*

tions of the area elements much better than 25×25 μm^2 can be achieved without exceeding the conventional computer power.

4.3.2 Effective Medium Approach

The effective medium method is used to calculate the effects of anisotropic pinning in YBa$_2$Cu$_3$O$_{7-x}$ single crystals with unidirected twin boundaries. It is based on a phenomenological approach [134,142,143] that predicts the resistivities in longitudinal ρ_l and transverse ρ_t directions with respect to the external current density if the unidirected twin boundaries form an angle θ with the current direction (cf. Fig. 4.1). These resistivities are related to the intrinsic resistivities where the current is applied parallel to the twin boundaries (vortex motion perpendicular to the twins) $\rho_\parallel$ and in perpendicular direction (vortex motion parallel to the twins) $\rho_\perp$, respectively

$$\rho_l = \rho_\parallel \sin^2 \theta + \rho_\perp \cos^2 \theta, \tag{4.1}$$

$$\rho_t = (\rho_\perp - \rho_\parallel) \sin \theta \cos \theta. \tag{4.2}$$

Due to the anisotropy of the pinning forces it is clear that the intrinsic resistivities should be different. However, it is not possible to measure the resistivity of a twin boundary directly but only via an averaged resistivity including the contributions of the twinned as well as of the untwined part.

For patterned irradiation experiments the case is somewhat different because both contributions to the intrinsic resistivities can be measured directly using the test bridges. Therefore $\rho_\perp$ and $\rho_\parallel$ of the effective medium approach can be calculated from the resistivities of the unirradiated and irradiated test bridges, ρ_u and ρ_i, respectively, using the corresponding channel widths of the irradiated Hall-structures

$$\rho_\perp = \frac{\rho_i \kappa + \rho_u}{\kappa + 1}, \tag{4.3}$$

$$\rho_\parallel = \frac{\rho_i \rho_u (1 + \kappa)}{\rho_i + \kappa \rho_u}, \tag{4.4}$$

where $\kappa = l_i / l_u$ is the ratio between the widths of the differently irradiated channels.

This approach enables to calculate transverse and longitudinal resistivities directly, but not the voltage drop across the Hall-structure in any arbitrary direction with respect to the channels. Another disadvantage of this method is that it is not possible to localize the voltage probes at a fixed position at the borders

of the patterning as in the real case of an experiment. The network calculation
method is therefore much more powerful and flexible here.

4.4   Results

Electrical transport measurements were performed on the periodically irradiated
Hall-structures with different aims. First, the results of magnetic field dependent
measurements are used to compare the effects of patterned irradiation with the
results on $YBa_2Cu_3O_{7-x}$ single crystals with unidirected twin boundaries in order
to check if there exists an effect of guided vortex motion in irradiated HTSC thin
films prepared as described above. On the other hand the measurements represent
a test of the described network calculation. A successful modeling of the Hall-
system then facilitates the interpretation of several features in the experimental
results that will be discussed in the following.

4.4.1   Zero Field

The resistive transitions of the irradiated Hall-structure have been measured for
different directions of the voltage drop with respect to the external current direc-
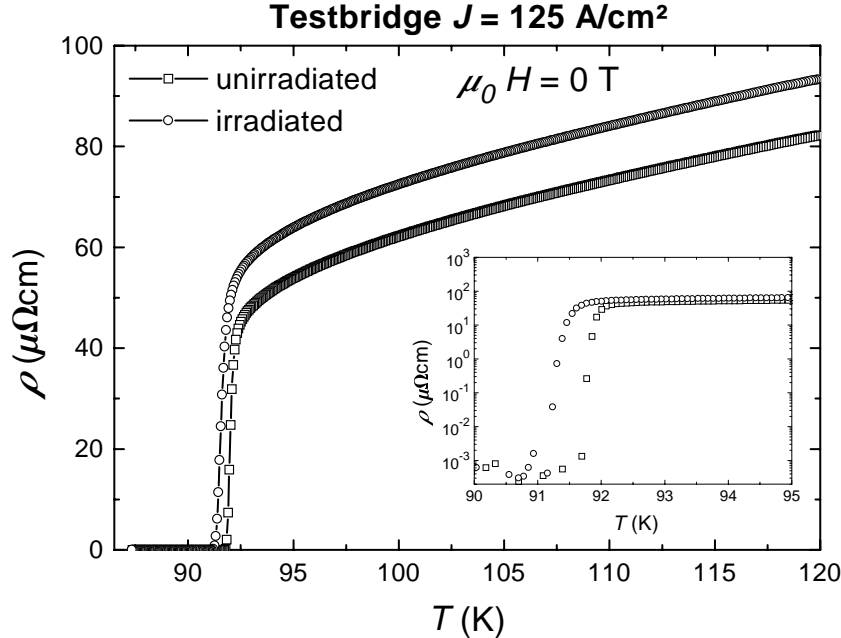

Figure 4.6:   *Resistive transitions of the test bridges for the 1:7 ratio Hall-
structure in zero field. The same irradiation effects as in Fig. 3.2 are observed.
In the irradiated case the normal state resistivity is increased and T_c is de-
creased. The inset shows the transitions in a semi logarithmic representation.*
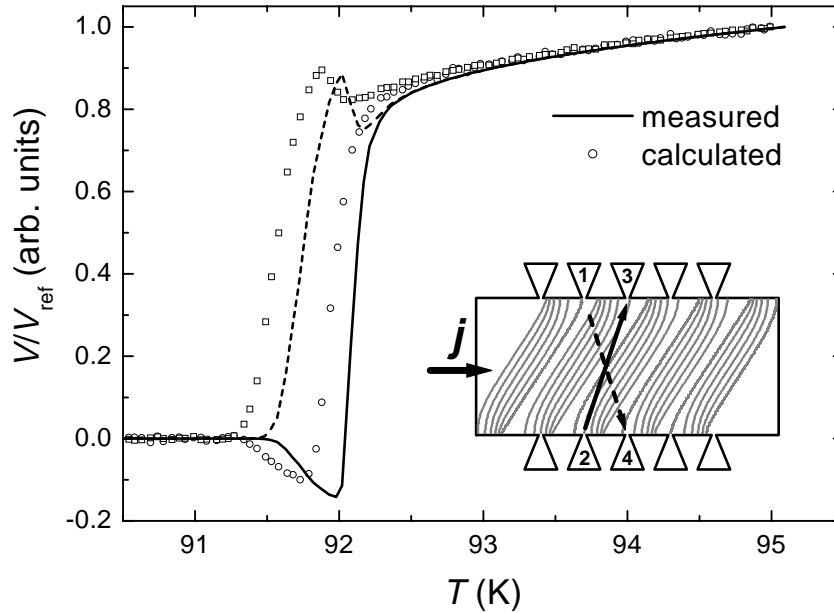
Figure 4.7:   *Voltage drop between two contact pairs of different direction with respect to the applied current density for the structure with the 1:7 ratio in zero magnetic field. The solid line (calculated data) corresponds to the open circles (measured results), the dashed line to open squares. Measured and calculated data are normalized to its corresponding value at $T = 95$ K. The position of the contacts is sketched schematically in the inset. In this sample T_c differs by 0.14 K between test bridges and Hall-structure, visible as a shift in the local extrema between calculated and measured curves. The inset shows the measurement geometry as well as the equipotential lines for $T = 91.88$ K.*

tion in zero field. In an unirradiated sample transverse voltages are negligible in zero field and one should observe a monotonously vanishing voltage signal along all contact configurations containing a longitudinal component. Measuring the configurations connecting contacts 1 and 3 (V_{13}) (see inset of Fig. 4.7) should yield identical results as probing V_{24}, V_{14}, or V_{23}, respectively.

In the patterned irradiation geometry the symmetry of the contact configuration is broken. As illustrated in Fig. 4.6, the test bridge resistivities are different for the unirradiated and the irradiated part for temperatures near T_c. In consequence, the resistivities of the strong and weak pinning channels are also different in this temperature range and the resistive transition measured using V_{14} shows a maximum at 91.88 K and using V_{23} one even observes a sign reversal. The network calculation reproduces these unusual features for both contact configurations. Figure 4.7 shows the temperature dependence of V_{14} and V_{23} together with the corresponding calculations. The existence of a sign reversal for V_{23} is obvious from the arrangement of the equipotential lines sketched in the inset. It

shows the equipotential lines across the 1:7 ratio structure resulting from the network calculation at $T = 91.88$ K. At this temperature the ratio $\rho_{unirr}/\rho_{irr} \approx 0.04$ and therefore the potential distribution across the Hall-structure is very similar to the 3D plot of Fig. 4.5. By measuring the two indicated directions, the number of equipotential lines that are crossed differs due to the arrangement of the strong and weak pinning channels. Following the dashed line, i.e. V_{14}, the equipotential lines are only crossed in the positive current direction, whereas this is not the case for the contacts of the solid line representing the measurement of (V_{23}).

4.4.2 Field Dependent Measurements

If the voltage drop for fixed temperatures is measured during magnetic field sweeps (-12 T $< \mu_0 H < 12$ T), the consistency between calculation and measurement holds for the longitudinal voltages as well as for the transverse case. This becomes obvious if the magnetic field dependences of the test bridge resistivities are considered. Figure 4.8 gives examples of the $\rho(B)$ behavior for both structures and both irradiation states respectively. Again the potential distribution of Fig. 4.5 is obtained if the ratio ρ_u/ρ_i differs significantly from 1, e.g. in the vicinity of the superconducting transition. In this field regime the influence of the columnar defects is strongest.

However, the network calculation does not include the asymmetric part of the transverse voltages V_{odd}^t that can be measured for inversion of the magnetic field due to the Hall-effect [144]. But here the interest is focused on the analogue of guided vortex motion in twin boundaries due to the anisotropic pinning forces present in the samples. This shows up as a transverse voltage, symmetric with respect to the field direction [139]

$$V_{\mathrm{even}}^t = \frac{V_{12}^t(+H) + V_{12}^t(-H)}{2}, \qquad (4.5)$$

where V_{12} is defined in Fig. 4.7. This procedure eliminates the asymmetric Hall-contributions. The magnetic field dependence of V_{even}^t at different temperatures is shown in Fig. 4.9 for the 1:7 ratio structure and in Fig. 4.10(b) for the 1:4 ratio structure, respectively.

Both samples show the same behavior, except for the fact that the angle θ describing the direction of the weak pinning channels is $+45°$ in one and $-45°$ in the other case. This results in negative and positive values for V_{even}^t as can be directly seen from the calculation of the potential distribution (e.g. inset of Fig. 4.7 for the case of $\theta = +45°$). For magnetic fields $\mu_0 H > 3$ T, the absolute value decreases with decreasing field. For smaller fields, an increase of $|V_{\mathrm{even}}^t|$ which has a maximum at $\mu_0 H_m$ followed by a sharp transition to $V_{\mathrm{even}}^t = 0$ at $\mu_0 H_0$ can be observed. The characteristic field $\mu_0 H_m$ increases and $|V_{\mathrm{even}}^t(\mu_0 H_m)|$
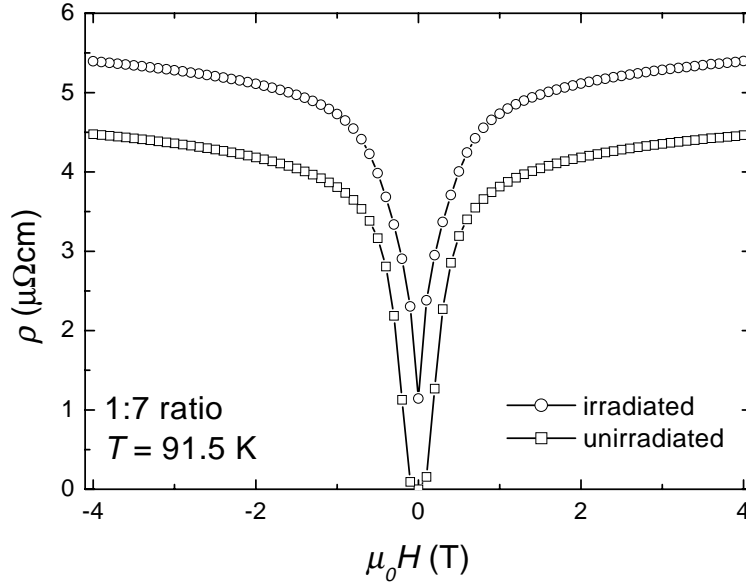
a)
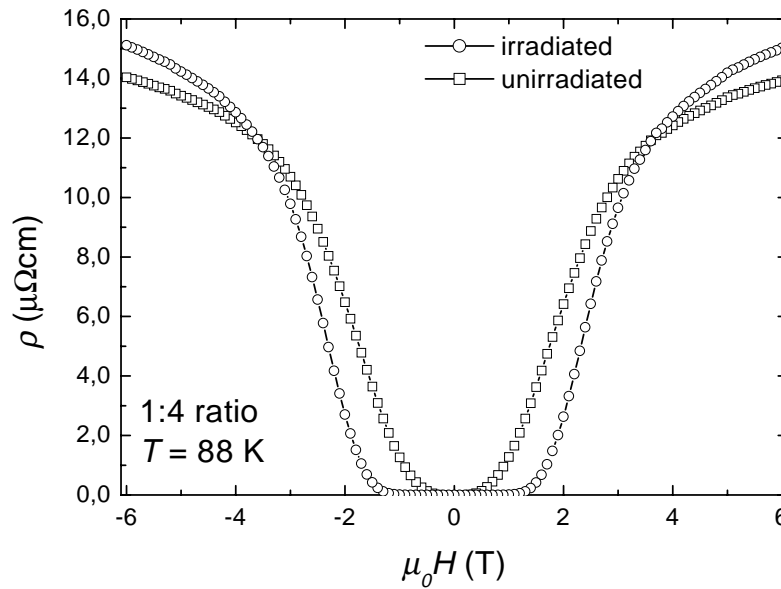
b)

Figure 4.8:   *Magnetic field dependence of the test bridge resistivities.*
(a) Structure with 1:7 ratio: At temperatures $T > T_c(\phi \neq 0)$, $\rho_i > \rho_u$ for the whole magnetic field range. In this case the calculated potential will increase continuously along the Hall-structure from 0 to 1.
(b) Structure with 1:4 ratio: For $T \leq T_c(\phi)$, due to the enhanced pinning of the irradiated part, the transition of $\rho_i(B)$ is sharper. The ratio $\rho_u/\rho_i >> 1$ for fields 0.5 T $< \mu_0 H < 1.5$ T yielding a steplike potential distribution as illustrated in Fig. 4.5. This arrangement represents the macroscopically anisotropic pinning situation.

decreases with decreasing temperature. A very similar behavior of the even transverse voltage was observed in $YBa_2Cu_3O_{7-x}$ single crystals with unidirected twin boundaries [128]. Thus, these results are a first indication for guided vortex motion in periodically irradiated $YBa_2Cu_3O_{7-x}$ thin films. However, compared to $YBa_2Cu_3O_{7-x}$ single crystals one should note that the length scale of both experiments is very different. In the case of twin boundaries the electric field in the sample is inhomogeneous on a microscopic scale and the voltage drop is localized near the twin boundary. But the periodic length in twin boundary experiments is about 1 μm to 10 μm [127,128] and is much smaller than the distance between the voltage contacts. The experiment here was performed on a length scale that is two orders of magnitude larger. In spite of this huge difference the temperature and magnetic field dependencies of the even transverse voltage are comparable. The origin of this resemblance is discussed in the following.

At high field values in this experiment the resistivity of irradiated and unirradiated regions of the film is close to the normal state resistivity, which is approximately the same for both regions. Therefore $\rho_u/\rho_i \approx 1$ and no transverse voltage should occur. For single crystals in the normal state, the twin bound-
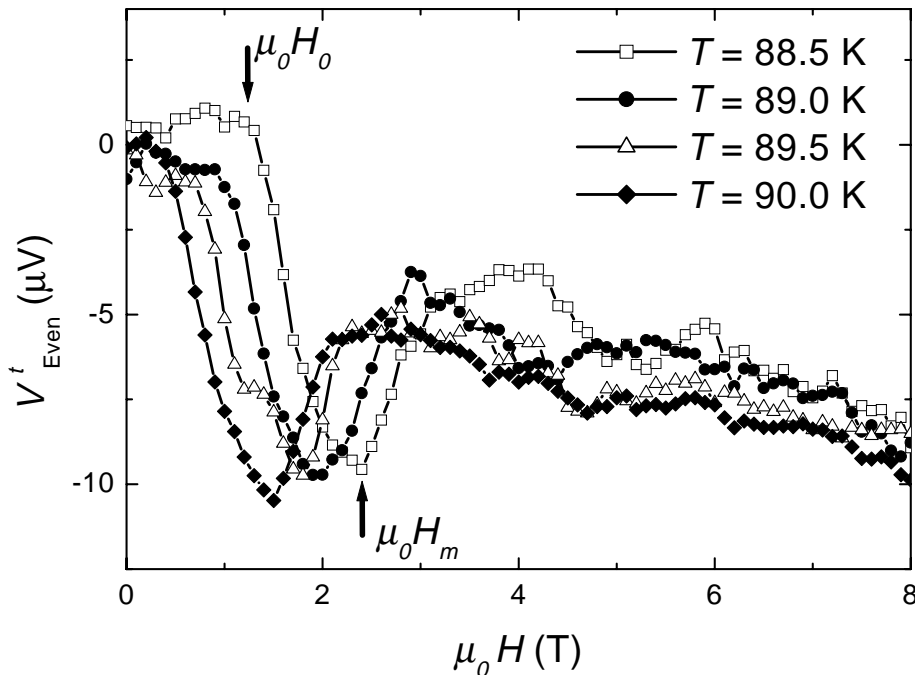
Figure 4.9: *Even transverse voltage for temperatures below T_c in the case of the 1:7 ratio structure ($\theta = -45°$). The curve is characteristic for the guided vortex motion effect and was also observed for $YBa_2Cu_3O_{7-x}$ single crystals with unidirected twin boundaries. The characteristic fields are considered to be $\mu_0 H_m$ where V^t_{even} reaches its maximum and $\mu_0 H_0$ where it vanishes.*
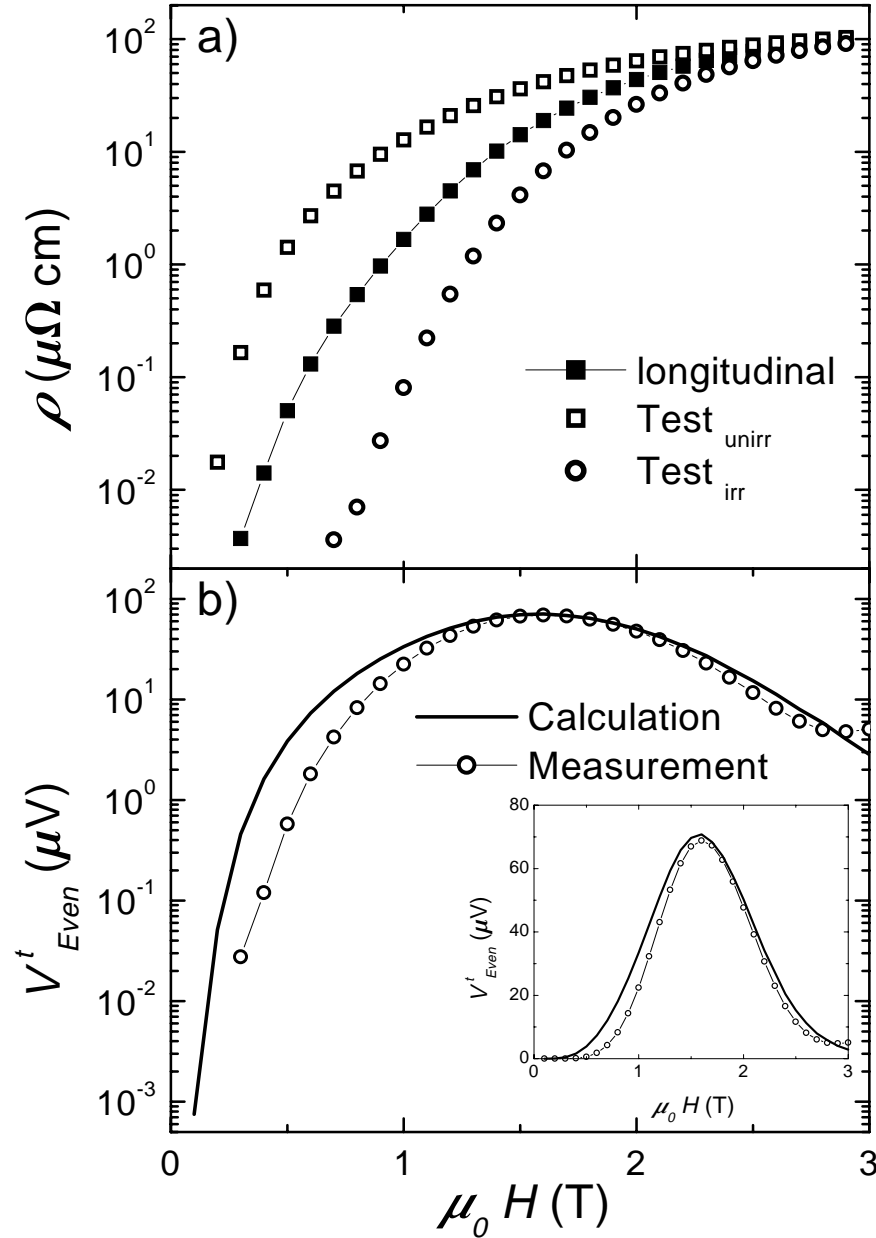
Figure 4.10: *Magnetic field dependence of the longitudinal resistivities and the even transverse voltage of the Hall-structure with the 1:4 ratio at 88 K. (a) resistivities of the irradiated (open circles) and unirradiated (open squares) test bridge. As discussed in the text, the magnetic field behavior of the longitudinal resistivity indicates the existence of vortex-vortex interactions between the channels. (b) Measured and calculated even transverse voltage. In this case, $\theta = -45°$. At low temperatures, calculated and measured values differ by one order of magnitude. The inset shows a linear plot of the transition. The deviation for high magnetic fields is discussed in the text.*

parallel - 1:1 scale

▼ ▼ ▼ ▼
...n n n n n n n n n n p p p p...
...n n n n n n n n n p p p p n...
...n n n n n n n n p p p p n n...
⋮
...n n p p p p n n n n n n n n...
...n p p p p n n n n n n n n n...
...p p p p n n n n n n n n n n...
▲ ▲ ▲ ▲

a)

maximal longitudinal contribution

▼
...n n n n n n n n n n p p p p...
...n n n n n n n n n p p p p n...
...n n n n n n n n p p p p n n...
⋮
...n n p p p p n n n n n n n n...
...n p p p p n n n n n n n n n...
...p p p p n n n n n n n n n n...
▲

c)

parallel - 1:4 scale

▼
...n n n n n n n n n n p p p p...
...n n n n n n n n n p p p p n...
...n n n n n n n n p p p p n n...
⋮
...n n p p p p n n n n n n n n...
...n p p p p n n n n n n n n n...
...p p p p n n n n n n n n n n...
▲

b)

minimal longitudinal contribution

▼
...n n n n n n n n n n p p p p...
...n n n n n n n n n p p p p n...
...n n n n n n n n p p p p n n...
⋮
...n n p p p p n n n n n n n n...
...n p p p p n n n n n n n n n...
...p p p p n n n n n n n n n n...
▲

d)

e)

Figure 4.11: *Longitudinal contributions to V^t resulting from the network calculations. Due to its lateral extension the voltage probes (black triangles) cover more than one resistor area element (n, p). At least four geometries are realistic in the experiment. (a) The calculated voltage is averaged over four parallel area elements. (b) The voltage probe is considered to be pointlike. For an inhomogeneous probe longitudinal contributions must be taken into account. In the network calculation this fact is respected with (c) a maximal and (d) a minimal longitudinal contribution. (e) A comparison with the measurement shows that a small longitudinal contribution is measured for high magnetic fields. Note that the calculations for the parallel geometry yield identical results.*

aries only marginally influence the total resistivity and accordingly the transverse voltage vanishes. Experimentally small values of V_{even}^t are observed in both cases which are attributed to a small longitudinal contribution due to experimental artefacts as will be shown below. For temperatures below T_c and low magnetic fields again no transverse voltage is observed in both experiments. Clearly in this temperature and field range the vortex system becomes rigid and the longitudinal resistivity vanishes in the whole sample enforcing zero transverse voltage.

For these reasons the attention is focussed in the following on the intermediate field range where a pronounced maximum of V_{even}^t is observed. The calculation reproduces quantitatively the maximum in the magnetic field dependence of V_{even}^t as shown in the inset of Fig. 4.10(b). The existence of this maximum was already verified in an analytical approach by Shklovskij *et al.* [138] These authors used the above described effective medium approach to calculate the averaged resistivity of $YBa_2Cu_3O_{7-x}$ crystals containing dense arrays of unidirected twin planes. However, in the case presented here only a small number of weak pinning channels exists and an effective medium theory is not appropriate. A second point to mention is that nonlinearities of the CVCs have to be taken into account. This is done by using identical current densities for the reference bridges and the Hall-structures. In this case the continuity condition for the current eliminates nonlinear effects in first approximation. Compared to the calculated values for V_{even}^t the experimentally determined values show deviations for high and low fields. At high fields, the influence of the limited lateral resolution of the photolithographically patterned voltage probes leads to a residual longitudinal voltage. This fact is illustrated in Fig. 4.11, where four possible scenarios are shown. The voltage probes at the borders of the Hall-structure are not pointlike but have a width $w = 100~\mu$m. As the dimensions of the area elements used for the resistor network calculation are smaller ($25 \times 25~\mu\text{m}^2$), a longitudinal voltage will be detected in this geometry except for a nearly perfect contact (Fig. 4.11(a) and (b)). The comparison between the different calculations and the measurement of the indicated contacts (inset of Fig. 4.11(e)) proves that a longitudinal contribution to the transverse voltage at high magnetic fields must be taken into account. Depending on the quality of the respective voltage probes this contribution is stronger or weaker. The calculations also show that this contribution is negligible for fields below $\mu_0 H_m$.

More interesting are the deviations in the vicinity of $\mu_0 H_0$ where the transition to $V_{\text{even}}^t = 0$ appears. The logarithmic illustration of Fig. 4.10(b) indicates that the measured value is nearly one order of magnitude smaller than the corresponding calculated value expected from the longitudinal resistivities of the reference bridges. Effective medium calculations yield qualitatively same results. It is possible that this discrepancy is due to the interaction between pinned flux lines in the irradiated channels and vortices in the weak pinning channels as will

be discussed below.

A further interpretation of these results requires a detailed analysis of the different vortex states in the irradiated Hall-structure. A straightforward access to this problem is the analysis of the current-voltage characteristics of the test bridges. In the case of the sample with the 1:7 ratio structure Fig. 4.12 shows such a set of curves for the irradiated part of the test bridge and a magnetic field of $\mu_0 H = 1$ T. The Bose-glass temperature T_{BG} of the irradiated and the vortex glass temperature T_{VG} of the unirradiated test bridge were determined using the known scaling analysis described in chapter 3.

Such a scaling analysis is illustrated in Fig. 4.13 for the irradiated test bridge at $\mu_0 H = 1$ T. For $z' = 7.5(2)$ and $\nu'_\perp = 0.94(2)$, all CVCs in question collapse onto two branches that are separated by $T_{BG} = 89.8(3)$ K. Comparable scaling results are obtained for the test bridges of the 1:4 ratio structure. It is worth to mention at this point that the critical exponents obtained here are very similar to those obtained for a scaling analysis of the long measurement bridges described in chapter 3 if the reduced electric field window is used for the glass scaling. The use of an extended measurement window would probably yield a higher dynamic critical exponent z'. However, the glass temperatures T_G of the irradiated and unirradiated test bridge respectively are used here only to build the irreversibility lines for both cases. For the Hall-structure with the 1:4 ratio and the correspond-
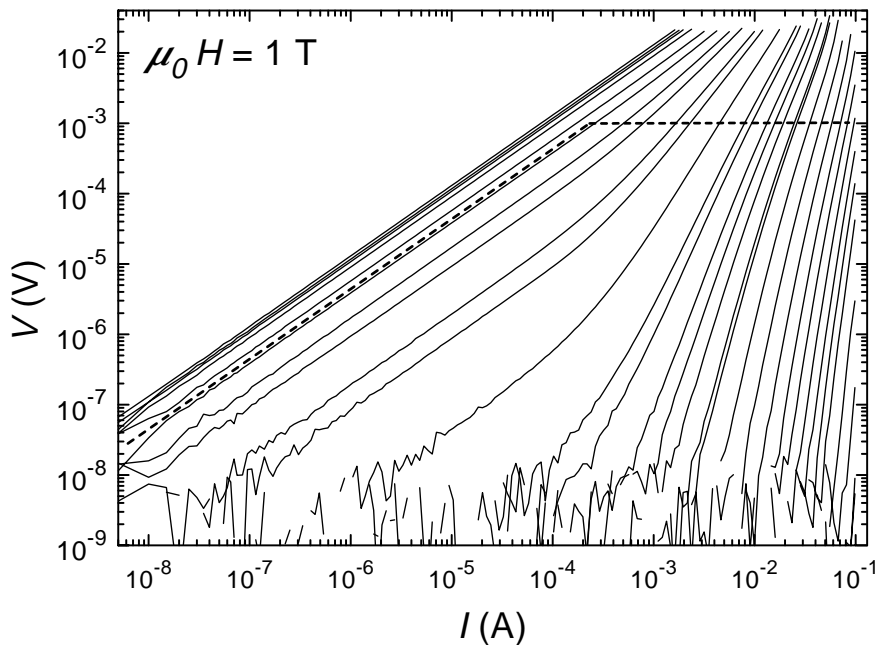

Figure 4.12: *CVCs of the irradiated test bridge for the sample with the 1:7 ratio structure. Isotherms between 91 K and 80 K (from left to right) for $\mu_0 H = 1$ T are shown. The dashed lines border the region used for the Bose-glass scaling shown in Fig. 4.13.*
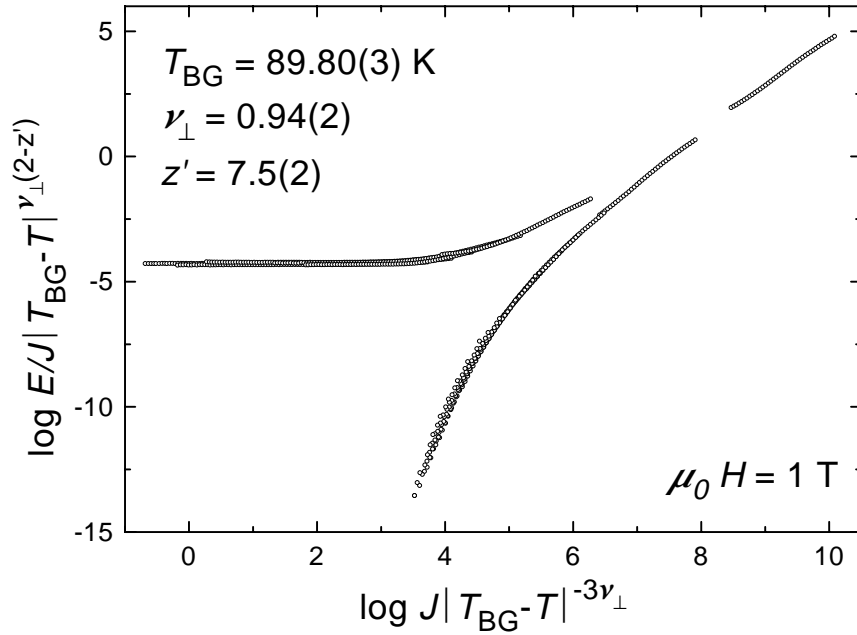
Figure 4.13:   *Bose-Glass of the CVCs of Fig. 4.12. Good scaling is achieved with $T_{\mathrm{BG}} = 89.8(3)$ K, $\nu_\perp = 0.94(2)$ and $z' = 7.5(2)$.*

ing test bridges the temperature dependence of the characteristic field $\mu_0 H_{BG}(T)$ is shown in Fig. 4.14 (open squares) together with the $\mu_0 H_{VG}(T)$-behavior of the unirradiated test bridge (open circles). It is in qualitative accordance with $H(T)$ diagrams obtained in experiments that reveal the influence of correlated defects on the vortex system. [54,132] In addition, the characteristic points of $V_{\mathrm{even}}^t(\mu_0 H)$ for different temperatures shown in Fig. 4.10(b) are plotted. The magnetic fields $\mu_0 H_m$ at which V_{even}^t reaches its maximum (filled upward triangles) and $\mu_0 H_0$ where V_{even}^t disappears (filled downward triangles) are two important features.

The first information one can extract from this diagram is that the maximum of V_{even}^t appears for fields and temperatures above the irreversibility line of the irradiated test bridge. A comparison between the 1:4 ratio and the 1:7 ratio structure shows that the temperature dependence of $\mu_0 H_m$ is proportional to T/T_c^{irr}, where T_c^{irr} is the critical temperature of the irradiated test bridge in zero field. Thus, the peaks in the field dependence of V_{even}^t shown in Fig. 4.9 and Fig. 4.10(b) appear in the flux flow regime.

The analysis of the temperature and magnetic field behavior of $V_{\mathrm{even}}^t = 0$ is the second point to be discussed in this context. In the phase diagram the obtained data points for $\mu_0 H_0(T)$ can be found between the irreversibility lines of irradiated and unirradiated test bridges. However, the position of the $\mu_0 H_0(T)$ line with respect to the test bridge results depends on the ratio between the widths of both, strong and weak pinning channels. For the 1:7 ratio structure the irradiated channels are dominant and the $(\mu_0 H_0(T))$-line coincides with the

irreversibility line of the irradiated test bridge. The situation is different for the Hall-structure with the 1:4 ratio. In this case, the $\mu_0 H_0(T)$ line is shifted towards lower fields and lower temperatures.

While such a behavior is expected for a sensitivity limited detection of the small transverse voltage it could also be induced by a vortex-vortex interaction. Support for this mechanism is gained from Fig. 4.10(a) where the longitudinal resistivity is shown. The measured longitudinal resistivity in the Hall-structure is between that of the irradiated and that of the unirradiated bridge. For noninteracting channels the measured longitudinal resistance in the Hall-structure should roughly correspond to the resistivities of the respective parts weighted with the channel widths. However, for fields smaller than 1.5 T the measured longitudinal resistivity is more than a magnitude smaller than the resistivity of the higher ohmic channel. This observation indicates the existence of vortex-vortex interactions between the channels as proposed by Marchetti and Nelson [13,55]. This hydrodynamic approach is based on two heavily irradiated *Bose-glass contacts* that sandwich a weak pinning channel and was already described in chapter 1 and Fig. 1.7. The potential distribution illustrated in Fig. 4.5 and in the inset
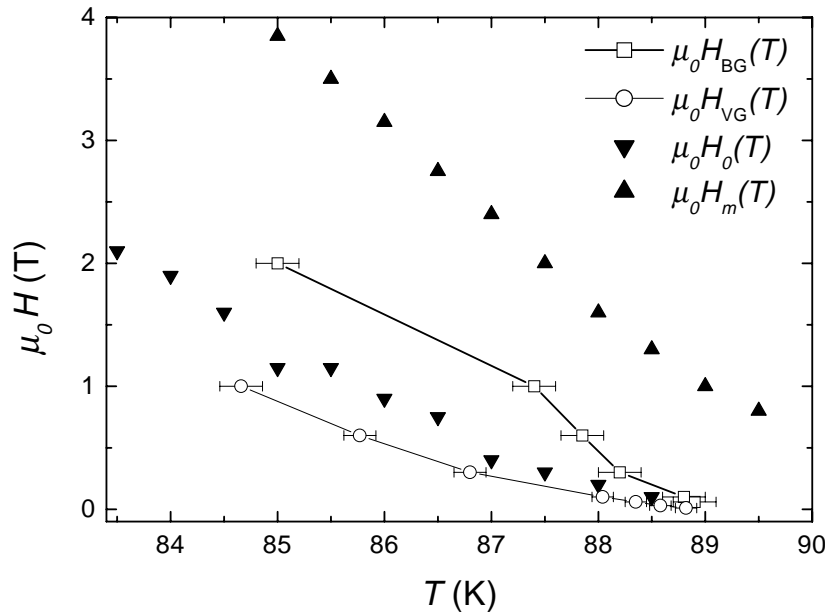
Figure 4.14: *Temperature dependent characteristic fields of the irradiated (open squares, $\mu_0 H_{\mathrm{BG}}(T)$) and unirradiated (open circles, $\mu_0 H_{\mathrm{VG}}(T)$) test bridge. In addition, $\mu_0 H_0(T)$ revealing from the magnetoresistive measurements of V_{even}^t for the 1:4 ratio structure is plotted (filled downward triangles) together with the $\mu_0 H_m(T)$ dependence (filled upward triangles). The position and the behavior of the $\mu_0 H_0(T)$ curve in the phase diagram corresponds to predictions for a Bose-glass contact [13].*

of Fig. 4.7 shows that the patterned irradiation experiments represent this geometry. The current vector is directed perpendicular to the equipotential lines and the resulting current path is illustrated in Fig. 4.15 for $R_{irr} \ll R_{unirr}$. The periodic pinning arrangement therefore induces a locally varying current direction yielding a vortex motion perpendicular to the current direction and thus parallel to the weak pinning channel direction. Following this interpretation, the effect of guided vortex motion in the twin boundary experiments is not the direct consequence of the planar pinning potential, but founded in an inhomogeneous current distribution.

At the Bose-glass transition temperature of the strong pinning regions, the vortices in the weak pinning channels are in the liquid state. Therefore the trapped vortices in the irradiated regions act like a barrier for the weakly pinned flux lines. The interaction between strongly and weakly pinned vortices can be described by a viscous length δ which depends on the flux liquid viscosity [140]. A further analysis shows that δ is the Bose-glass correlation length $l_\perp$ [11]. Therefore, the borders of a weak pinning channel can be understood as a *Bose-glass contact* and the results of Fig. 4.9 and Fig. 4.10(b) can be interpreted in this picture. The vanishing transverse resistivity at $\mu_0 H_0(T)$ indicates the transition into a glass phase in the weak pinning channels at fields well above $\mu_0 H_{VG}$. This is underlined by the comparison between the measured and calculated magnetic

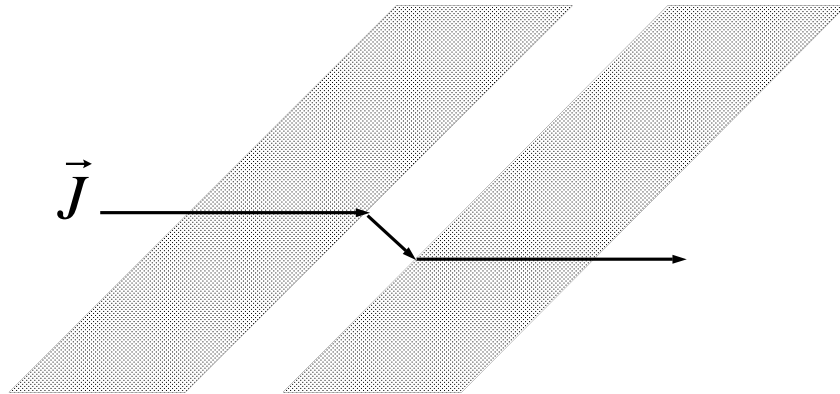Figure 4.15:   *Expected current path in the Hall-structure for the patterned irradiation. As the current crosses equipotential lines vertically, this result follows directly from the potential distribution shown in Fig. 4.5 for the case that $R_{irr} \ll R_{unirr}$. This locally varying current direction induces a vortex motion parallel to the weak pinning channels. The dotted areas represent the irradiated regions.*

field dependence of V_{even}^t. The transition to $V_{\text{even}}^t = 0$ is measured for higher fields than the calculated transition, indicating that the divergence of the shear viscosity η depends on whether strong and weak pinning regions are independent or, as in the case of the Hall-structures and *Bose-glass contacts*, depends on the interaction between vortices in both regions. The length scale set by this interaction can be macroscopic and is described by the viscous length δ.

This result is consistent with other experiments carried out in this field of research. The diverging correlation length of the vortex system near the melting transition was already predicted by Nelson and Halperin [145]. For the case of $Bi_2Sr_2CaCu_2O_{8+\delta}$ single crystals being irradiated similarly to the samples used in this experiment, Pastoriza *et al.* [54] pointed out that the characteristic features of the melting transition can be observed when the correlation length is comparable to the dimensions of the width of the unirradiated channel (in this case $\approx 10\ \mu$m). Experiments in the Corbino disk geometry give an estimate of the order of magnitude of the dynamic correlations between vortices in $YBa_2Cu_3O_{7-x}$ single crystals. López and co-workers [57] report a correlation length with macroscopic dimensions. The voltage probes they used to obtain these results have distances of 60 μm which is in good agreement to the dimensions of the unirradiated channels in the experiment described above.

4.5   Microprobe Irradiation

Is was already mentioned that the pattern used to investigate the vortex dynamics in a periodically irradiated Hall-structure has a rather macroscopic character. The length scales in the motivating twin boundary experiments [127,128] are one or two orders of magnitude smaller than the periodic lengths l_p used here. In experiments where the flux lines are confined to narrow channels [53,146,147] advantage was taken of many channels to obtain a self averaged measurement signal. The same idea was used for the spatially resolved irradiation of $Bi_2Sr_2CaCu_2O_{8+\delta}$ single crystals where approximately 60 serially connected 3 μm wide strong pinning channels with $l_p = 10\ \mu$m were generated using a 200 μm thick Au/Kapton bilayer irradiation mask [54]. Hence, an increase of the channel density represents an improvement of the entire measurement set-up. The use of metal masks as shown in Fig. 4.2 is not practicable if the length scales of the irradiation pattern are reduced.

microprobe irradiation as described in section 2.3.2 is a very powerful irradiation technique in this context. This section describes the first irradiation of HTSCs and the corresponding investigations of vortex dynamics with use of this method. Unfortunately problems during the beamtime inhibited reliable results, but the conclusions that can be drawn from this first attempt are rather moti-

vating to continue this kind of experiments.

The structure of the Hall-patterning shown in Fig. 4.3 was slightly modified for the microprobe irradiation experiments. Again the angle between the borders of the Hall-structure and the direction of the channels was chosen to be $\theta = \pm 45°$. But in contrast to the irradiation through metal masks, the dimensions of the irradiated channels were reduced. Beside the aspired width of 10 μm the channel length is also limited to 200 μm due to technical reasons. Accordingly, the width of the Hall-structure should be smaller than 200 μm$/\sqrt{2} \approx 150$ μm. An illustration of the modified measurement structure ($100 \times 1000 \mu$m^2) is shown in Fig. 4.16.

This superposition of two images also shows the main irradiation results and the problems encountered during the microprobe beam time. The most important preparational work is the precise adjustment of the sample position with respect to the projected ion beam generating the strong pinning channels. Therefore two 10×10 mm^2 glass substrates are mounted in a rotating sample holder. A test structure which is identical to the modified Hall-structure was prepared on the lower substrate using a standard photoresist (*AZ 6612* produced by former Hoechst AG, Germany). On top of this structure ion tracks were generated and visualized in a second glass substrate. The relative position of the ion beam
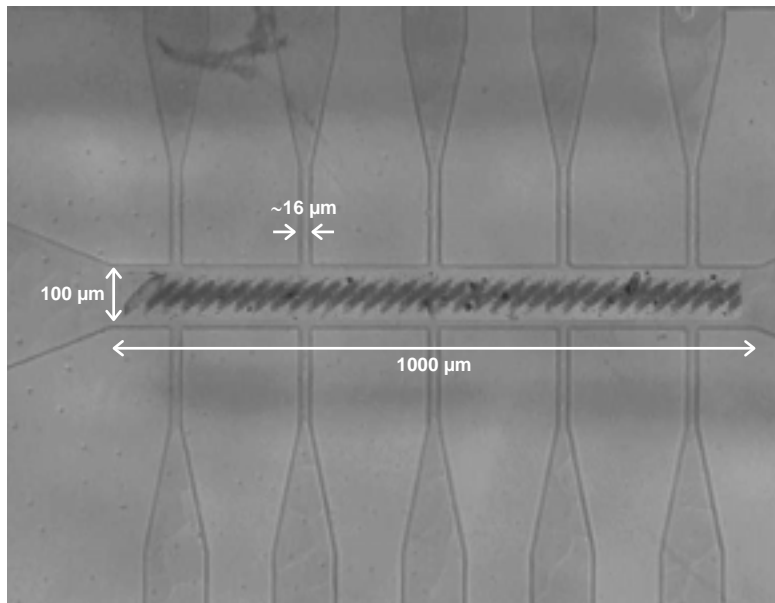

Figure 4.16:   *Illustration of the modified Hall-structure and a mapping of the first microprobe irradiation of HTSCs (see text). This superposition shows the image a test structure on a glass substrate that was used to adjust the orientation of the microprobe patterning as well as an image of ion tracks in a second glass substrate after HF etching.*
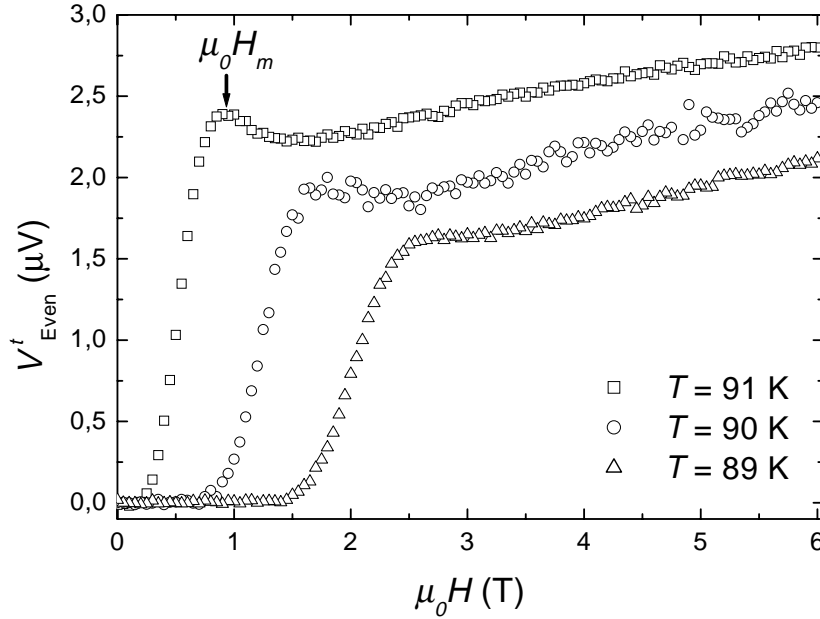
Figure 4.17:   *Even transverse voltage of the microprobe irradiated Hall-structure. As in the case of the macroscopic irradiation pattern the characteristic features of the $V_{\mathrm{even}}^t(H)$ behavior are observed (see text).*

aperture is determined by comparing the positions of the track patterning and the test structure. For the irradiation of HTSC thin films this positional correction has to be taken into account. But Fig. 4.16 indicates the fundamental problem met during this beamtime. The length of the strong pinning channels (dark stripes) is less than the required 200 μm and the channels do not cover the entire Hall-structure. In addition, the strong pinning channels do not have as sharp interfaces between irradiated and unirradiated regions as obtained for the irradiation through metal masks demonstrated in Fig. 4.4. Furthermore, the channel width is not constant over the full length so that the irradiation pattern resembles more to oval structures than to aligned channels. The reasons for this unsatisfying result was found in incorrect settings of the ion optics leading to a bad focussed ion beam. Unfortunately these problems could not be solved within the close beam time schedule and the intentions of the experiment failed.

However, the microprobe irradiation of an $YBa_2Cu_3O_{7-x}$ thin film was performed under the described circumstances for the very first time in order to evaluate the chances of success of this kind of experiment and to detect possible flaws in the experimental set-up.

As in the case of the 1:7 and 1:4 ratio structures the transverse voltage was measured at a fixed current density $J = 250$ A/m^2 in magnetic fields -6 T $\leq \mu_0 H \leq 6$ T and the even transverse voltage was calculated in accordance with

Eq. (4.5). The experimental results of this procedure are shown in Fig. 4.17 for temperatures between 89 K and 91 K. The behavior of V_{even}^t is similar to the results obtained on the irradiated Hall-structures with large channel dimensions (cf. Figs. 4.9 and 4.10). Again the maximum of the even transverse voltage at a field $\mu_0 H_m$ and the sharp transition to $V_{\text{even}}^t = 0$ are the main features of these curves. But in the case of the mircroprobe irradiated sample the value for V_{even}^t at high magnetic fields $H > H_m$ is larger compared to the cases reported above. The reason for this observation is attributed to an increased longitudinal contribution to V_{even}^t due to the dimensions of the voltage probes. A network calculation points out this assumption as illustrated in Fig. 4.18. This calculation is based on a simplified network matrix representation. In contrast to the modeling of the 1:4 and 1:7 ratio structures one area element represents now $2 \times 2 \ \mu\text{m}^2$ and the irradiated pattern is assumed to be linelike with the dimensions $w = 10 \ \mu\text{m}$, $l = 71 \ \mu\text{m}$ and a periodic length of 20 μm. The pattern is positioned in the middle of the Hall-structure as indicated in Fig. 4.16 for the irradiation of the glass substrates. The fact that the channels do not cover the whole width of the Hall-structure breaks the condition that the current is forced to cross unirradiated as well as irradiated regions and an identical current density in these regions cannot be assumed any longer. However, this procedure permits an estimation of the potential distribution and the voltage drop across the microprobe irradiated Hall-structure.

If the lateral expansion of the approximately 16 μm wide voltage probes is taken into account when extracting the transverse voltages from the calculated potential distribution (cf. Fig. 4.11), a maximal longitudinal contribution to V_{even}^t would suppress the maximum of the even transverse at $\mu_0 H_m$ completely. Such a strong effect is not observed in the measured data presented here, but for high fields an increased longitudinal contribution is clearly visible in Fig. 4.17. The reason for this increase is the ratio between the distance and the width of the voltage probes defined by

$$r_{\text{Probe}} \equiv \frac{w_{\text{Probe}}}{d_{\text{Probe}}}, \tag{4.6}$$

which is 0.16 in this case. For the geometry shown in Fig. 4.3, $r_{\text{Probe}} = 0.05$ and the longitudinal contribution to the even transverse voltage is reduced by a factor 3. This factor can also be estimated by comparing the ratio $V_{\text{even}}^t / d_{\text{Probe}}$ of Figs. 4.9 and 4.17.

Thus, the first microprobe irradiation provided valuable results regarding the execution of this experiment. Concerning the technical realization of the irradiation, the problem of ion focussing will be resolved quickly and a patterned irradiation with microscopic channel dimensions (10 μm $\times$ 150 μm) and sharp interfaces between irradiated and unirradiated regions should be possible in the
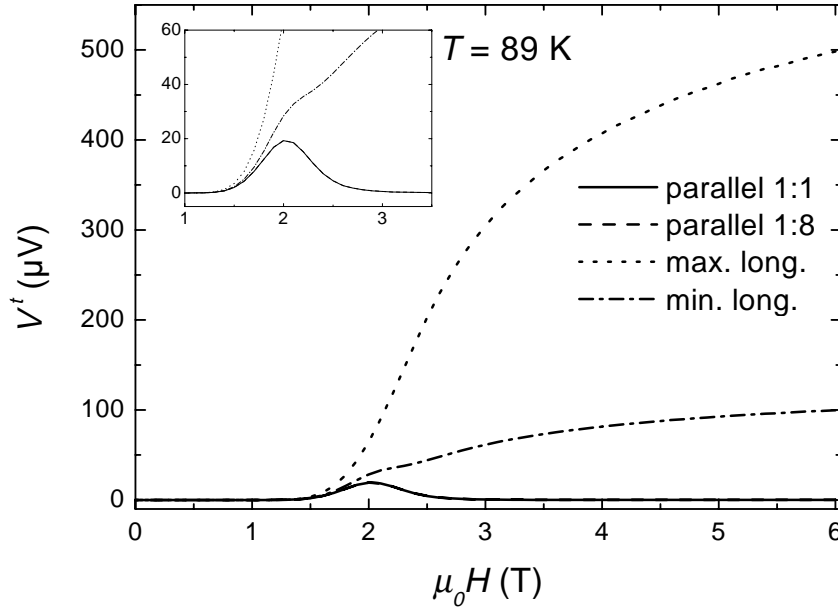
Figure 4.18: *Network calculation of the microprobe irradiated Hall-structure. The longitudinal contributions to the even transverse voltage yield a suppression of the characteristic features illustrated in Fig. 4.17 in the worst case. The calculations for both parallel configurations (1:1 and 1:8) are identical.*

near future. As a consequence thereof a reliable network calculation can be performed. In addition, it could be shown that the ratio r_{Probe} is an important quantity influencing drastically the results of transverse voltage measurements. An optimized width to distance ratio of the voltage probes has to be taken into account when designing new structures. In this context improved lithographic methods are rather useful in order to reduce the dimensions of the voltage probes.

4.6   Conclusions on the Patterned Irradiation

In summary, the vortex dynamics in periodically irradiated $YBa_2Cu_3O_{7-x}$ thin films for 100 μm wide unirradiated channels forming an angle of $\pm45°$ with the direction of an external current was investigated. This method can also be applied to other HTSC thin films and single crystals and the irradiation is not restricted to any pre-defined geometry. The magnetic field dependence of the even transverse voltage in such systems shows striking resemblance to a guided motion of the vortices as it was observed in recent experiments on $YBa_2Cu_3O_{7-x}$ single crystals with unidirected twin boundaries. So the microscopic mechanism is considered to be different in both cases.

Using irradiated and unirradiated on-chip test bridges it was possible to ana-

lyze the current-voltage characteristics of both the strong and weak pinning parts, respectively and to extract the input parameters for a numerical simulation of the potential distribution. This calculations additionally provide information about the direction of the current path in the Hall-structure. In a magnetic field and temperature regime in which guided vortex motion is expected, the current direction is essentially perpendicular to the weak pinning channels. Based on these results, the existence of a Bose-glass contact in the periodically irradiated samples was assumed. The obtained (H, T)-phase diagram was interpreted within the framework of a hydrodynamic approach near the Bose-glass transition. With respect to the guided vortex motion in twin boundary experiments this approach represents an alternative interpretation that is based on a locally varying current distribution. In this picture, the motion of vortices is a consequence of an anisotropic Lorentz-force density, in contrast to the assumption that an anisotropic pinning force is responsible for the guided vortex motion effect.

Finally the use of the microprobe to generate an irradiation pattern and first experimental results as well as occurring experimental problems were discussed. This irradiation technique is new in the context of vortex dynamics in HTSC and shows encouraging perspectives. One possible application of this method is the generation of a dc flux transformer irradiation geometry in order to probe the nonlocal resistive response of vortex liquids [55]. The creation of a variety of irradiation patterns on a microscopic scale will soon be possible.

Chapter 5

Realization of a Bose-Glass Contact

Vortex dynamics in periodically irradiated HTSC thin films has been treated in the previous chapter. It was worked out that pinned vortices in the irradiated channels interact with the weakly pinned vortices in the unirradiated regions and that these correlations can be described within a hydrodynamic approach of viscous vortex flow [13,55].

In order to study the dynamics of flux lines at a single interface between irradiated strong pinning regions and unirradiated weak pinning regions, the aim of this chapter is to prepare one single *Bose-glass contact*[1], to realize a direct measurement of the expected electric field profile illustrated in Fig. 1.7 and described by Eq. (1.31) as well as to extract the viscous length describing the strength of the vortex-vortex interaction in the interface region. Therefore high demands are imposed on the preparation of the measurement structure as well as on the irradiation procedure.

As in the case of the Microprobe irradiation discussed in the previous chapter this experiment is a first step regarding the applied technique as well as the obtained results and therefore is also has a somewhat exploratory aim.

5.1   The Measurement Structure

Measuring directly the local variation of the electric field in the *Bose-glass contact* geometry requires compact arrays of several voltage probes. In chapter 4 it was estimated that the length scale of the vortex-vortex interaction ranges between

---

[1]Following the results discussed in chapter 3, the existence of the vortex-glass and/or Bose-glass phase is not generally accepted. Therefore the expression *confined geometry* would be more appropriate. But as the terminology of the *Bose-glass contact* was introduced by Marchetti and Nelson [13], this term is used in the following.

10 μm and 100 μm. Therefore, the width of and the distance between the voltage probes should be as narrow as possible. With respect to the spatial resolution of the used photolithographic patterning these dimensions were $w_{\mathrm{Probe,1}} = 10$ μm and $w_{\mathrm{Probe,2}} = 20$ μm, respectively. The current is fed into a 100 μm wide and 2 mm long main bridge forming the center of the measurement structure illustrated in Fig. 5.1.

The complexity of the mask complicates the photolithographic patterning of the thin films and requires clean room conditions. In addition, the width of the voltage probes reaches the limits of the described patterning process and future experiments on *Bose-glass contacts* should take into account improved techniques of micropatterning. An alternative structure, where the upper voltage probes are replaced by two test bridges (50 μm $\times$ 2000 μm), was used for the patterning of a $Bi_2Sr_2CaCu_2O_{8+\delta}$ thin film. Optical microscopy and SEM images reveal a sharp microstructure so that the *Bose-glass contacts* could be prepared via heavy ion irradiation.

This kind of microstructure was particularly designed in order to probe the
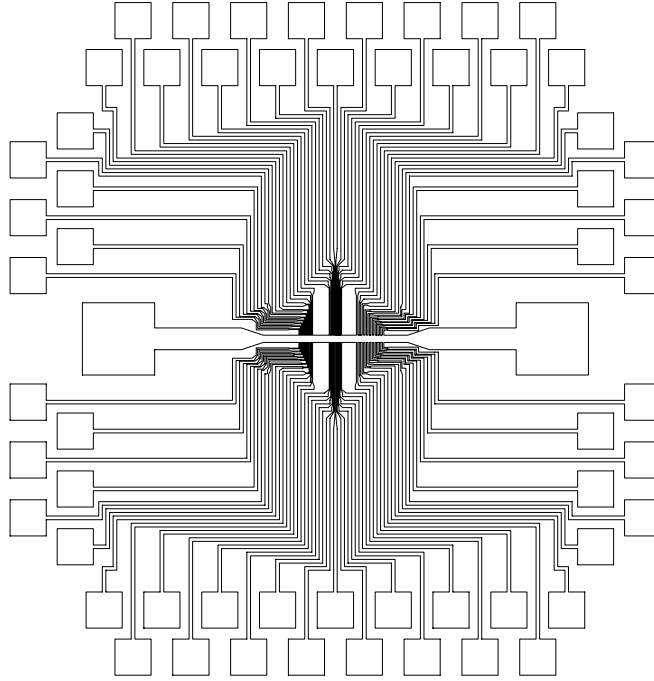
Figure 5.1:   *Photolithographic structure used for the measurements of the electric field profiles across a Bose-glass contact. The main bridge is located in the center of this structure. Three arrays of voltage probes are arranged along each side of the main bridge and permit to measure parallel and perpendicular to the current direction. Alternatively the upper probe array can be replaced by two test bridges (cf. Fig. 4.3). The central area of the measurement structure will be illustrated in a more detailed representation of the voltage probes in Fig. 5.2.*

local variation of the electric field in the *Bose-glasscontact* geometry. This arrangement of voltage probes considerably limits the electric field sensitivity of the measurement. For the channel geometry the local electric field in the weak pinning region is scaled in accordance with Eq. (1.31) in the limit of vanishing currents. A scaling analysis of CVCs measured with this probe array cannot be performed due to the reduced range in E.

5.2 Preparation of the Bose-Glass Contact

As in the case of the spatially resolved irradiation of the Hall-structure reported in the previous chapter, the preparation of a weak pinning channel in a strong pinning environment is realized via heavy ion irradiation through a Ni-mask. The position of this channels that remain unirradiated was adjusted to the middle of the voltage probe arrays so that most of the probes were covered by the mask. Only the outer probes belong to the strong pinning regions. The position of the Ni-mask was verified with an optical microscope before and after the irradiation. An image of the irradiation set-up is shown in Fig. 5.2. The upper part shows the photolithographic pattern of the main bridge and the different voltage probe arrays. The Ni-mask is fixed approximately 1 mm above the sample in the position shown in the lower image. The latter indicates that the areas which are probed by the the outer contacts of the corresponding arrays are not covered by the mask. These regions will be exposed to the ion beam and the respective voltage probes are used to measure the transport properties of the irradiated regions. This additional information is necessary in order to compare the transport properties of the irradiated and unirradiated parts. Table 5.1 summarizes the geometry parameters used for the preparation of the *Bose-glass contacts*. Beside the dimensions of the photolithographic structure the widths of the unirradiated channels L are also quoted. These values were determined by irradiating and etching a glass substrate through the same Ni-mask and measuring the channel width with an

Table 5.1: *Bose-glass contact geometry parameters used for the preparation of the structures shown in Fig. 5.2. The different length scales were verified with optical microscopy of the photolithographic structures and an irradiated and etched glass substrate, respectively.*
*) *The right side of array 3 remains unirradiated.*

Array	w_{Probe}	N_{Probes}	w_{array}	$L^{*)}$
1	10 μm	10	190 μm	115(5) μm
2	10 μm	9	170 μm	100(8) μm
3	20 μm	10	380 μm	345(5) μm
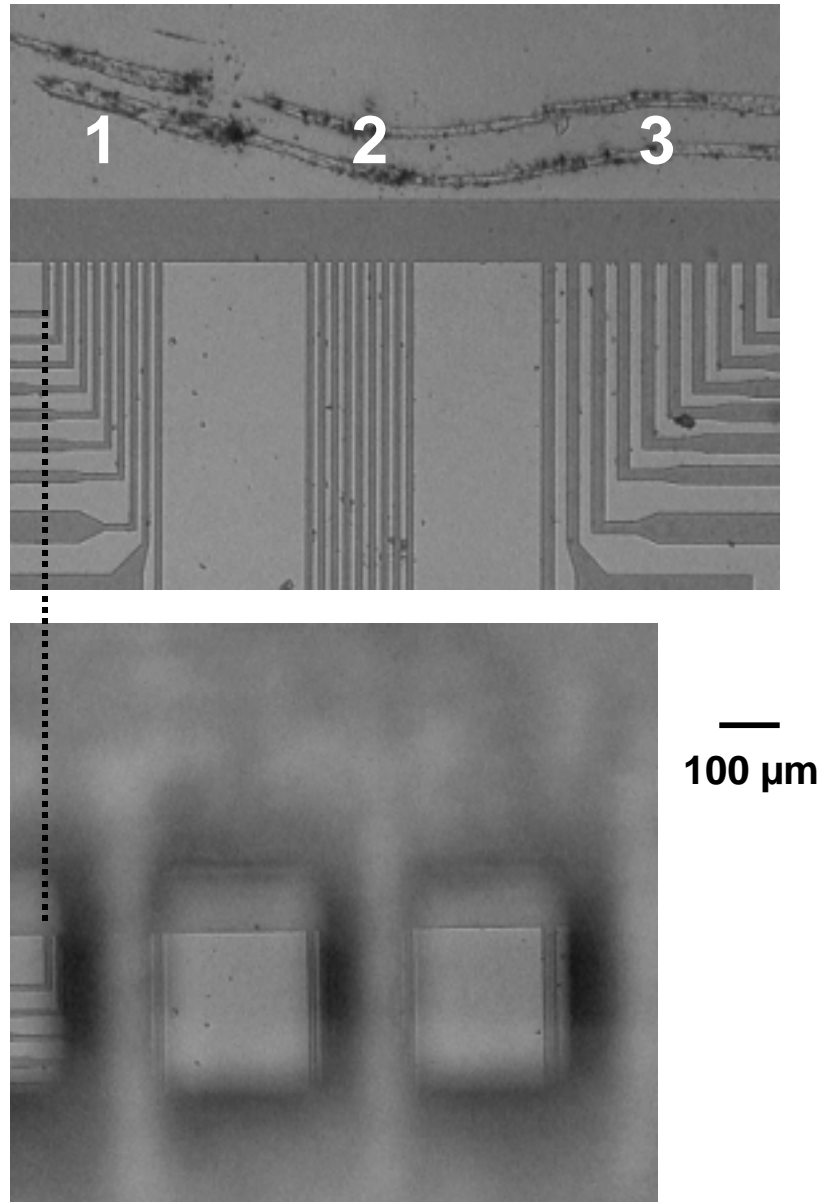
Figure 5.2:   *Optical microscope images describing the preparation of the Bose-glass contact. Upper part: image of the measurement structure. Three arrays probe the electric field profile with different lateral resolutions (10 μm and 20 μm). Lower part: The defocused layer shows the position of the Ni-mask on top of the probe arrays (focused layer). Three weak pinning channels are embedded in a strong pinning environment. The dotted line indicates the position of the left voltage probe of array 1 in both images. The main bridge is irradiated with 11.4 MeV/u ^{238}U ions at the positions of the outer voltage probes Table 5.1 summarizes the parameters of the geometrical arrangements that were used for the preparation of the Bose-glass contacts.*

optical microscope. The interfaces between strong and weak pinning regions are qualitatively similar to those obtained in the case of the patterned irradiation shown in Fig. 4.4. With this method the width of the weak pinning channel of array 1 was determined to $L = 115 \pm 5 \ \mu$m.

The irradiation of the $Bi_2Sr_2CaCu_2O_{8+\delta}$ thin film was performed with ^{238}U ions having an energy of 11.4 MeV/u and an equivalent field $B_\phi = 1$ T.

5.3   Transport Properties

After the irradiation the thin film was mounted on a sample holder and the 10 voltage probes of array 1 as well as the main bridge were connected to the measurement circuit as illustrated in Fig. 5.3. In this configuration the electric field profile was measured over an averaged distance of 180 μm that is divided into 9 segments. The use of a *HP 34970A* Data Acquisition/Switch Unit enabled to measure in parallel the respective segment voltages $V_{1,2}, V_{2,3}, \cdots, V_{9,10}$ as well as the averaged voltage

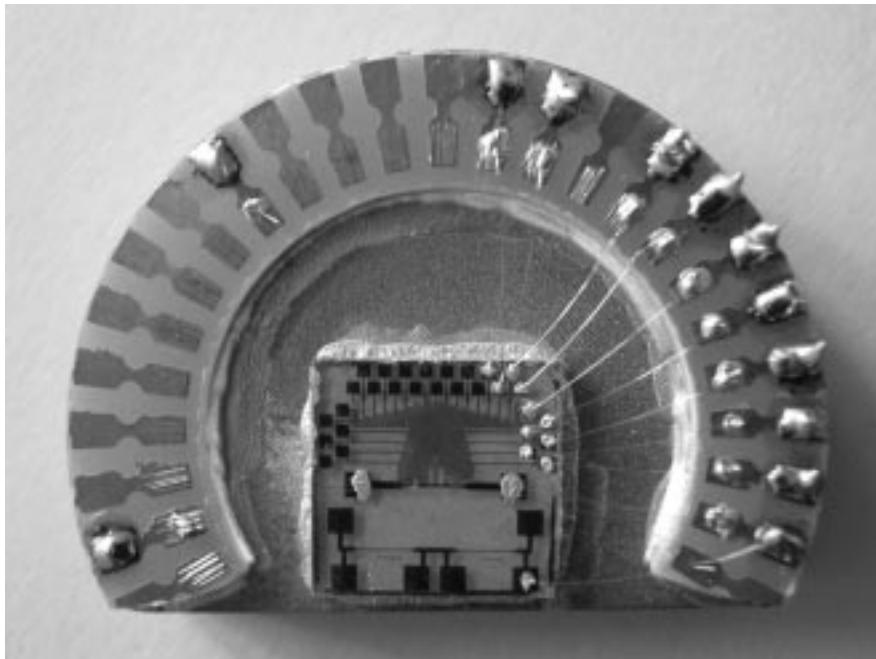$$V_{av} = V_{1,10} = \frac{1}{9} \sum_{i=1}^{9} V_{i,i+1}, \qquad (5.1)$$

Figure 5.3:   *Image of the contacted* $Bi_2Sr_2CaCu_2O_{8+\delta}$ *thin film mounted on the sample holder. The 10 voltage probes of array 1 are connected to the outer contact pads with Au wires. Two test bridges that are not connected are also visible in the lower part on the photolithographically patterned thin film.*

for external magnetic fields up to $\mu_0 H = 3$ T. All measurements were carried out during cooling of the sample down to temperatures $T = 60$ K with a small cooling rate.

5.3.1 Zero Field Transition

The filled symbols shown in Fig. 5.4 represent the zero field transitions of two of the segments, $\rho_{1,2}$ and $\rho_{5,6}$, respectively. The effect of irradiation is visible in an increased normal state resistivity of the outer segment $(1,2)$ compared to the inner one $(5,6)$. The unirradiated area only covers probes 3 to 8, whereas probes 2 and 9 belong to the interface region and the outer probes (1 and 10) are irradiated. Therefore $V_{1,2}$ probes the properties of the strong pinning region and $\rho_{1,2} > \rho_{5,6}$, in accordance with the results discussed in section 3.3. However, the irradiation effect is stronger in $Bi_2Sr_2CaCu_2O_{8+\delta}$ thin films compared to $YBa_2Cu_3O_{7-x}$ samples. Consistent with previous observations [49,92,148], the transition temperature T_c is shifted with the ion dose by approximately 5 K/T which is a factor 5 larger than the value extracted from Fig. 3.3 for $YBa_2Cu_3O_{7-x}$
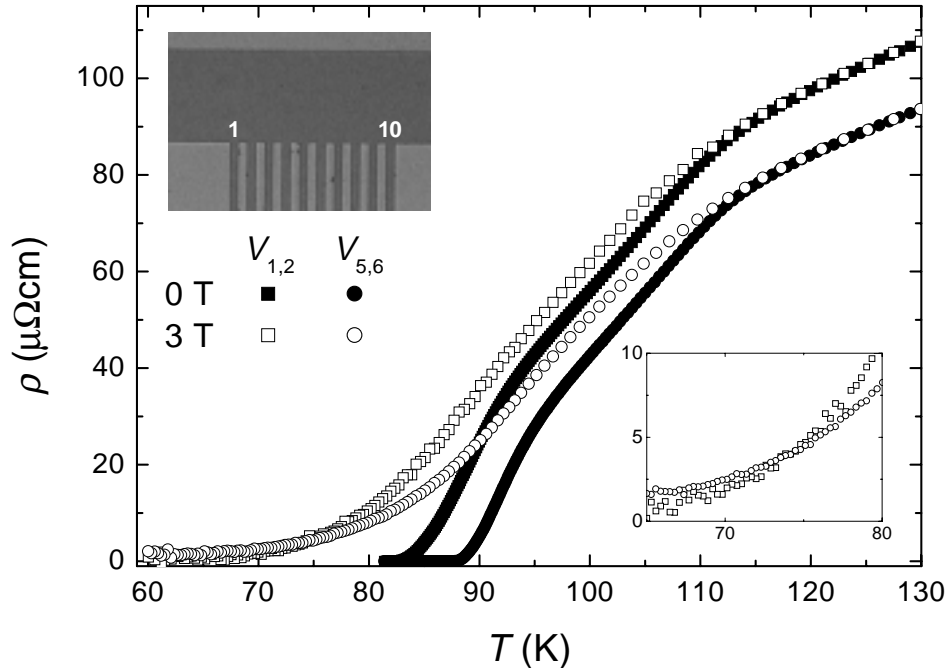

Figure 5.4:   *Resistive transitions of the segments 1 ($V_{1,2}$) and 5 ($V_{5,6}$) in zero field (filled symbols) and for $\mu_0 H = 3$ T (open symbols). The upper inset shows an image of array 1 with the 10 subsequent voltage probes and the corresponding ordering. In addition, the 3 T data near T_c is plotted in a magnified representation (lower inset).*
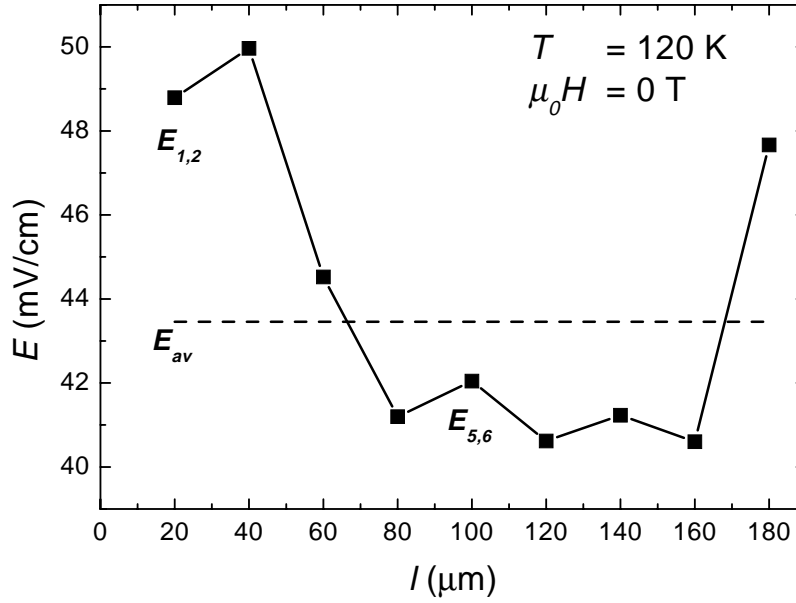
Figure 5.5: *Normal state electric field profile extracted from the $\rho(T)$ curves of the subsequent segments in zero magnetic field. The different values for $E(l)$ represent irradiated and unirradiated regions. The middle of voltage probe 1 is defined as $l = 0$.*

thin films that were irradiated with the same ion dose. A second feature of the $\rho(T)$ curves is the indication of a two-step transition with a first onset at 110 K which is characteristic if the sample additionally contains the $Bi_2Sr_2Ca_2Cu_3O_{10+\delta}$ phase.

To obtain the electric field profiles the corresponding data were extracted from the 9 $\rho_{i,i+1}(T)$ curves for a fixed temperature. Figure 5.5 illustrates an example for an $E(l)$ curve in the normal state at $T = 120$ K. This profile reproduces the situation of Fig. 5.4. Two different values of the electric field are obtained, corresponding to the irradiated and unirradiated regions. From this illustration it becomes clear that three voltage probes at the left side (1, 2, 3) had been exposed to the ion beam during irradiation. The segment at $l = 60$ μm contains the interface between strong and weak pinning regions because the electric field value between these probes coincides with the averaged field value $E_{av}(l)$ obtained from Eq. (5.1) which is represented by the dashed line

These results show that it is possible to measure the lateral resolution of the electric field in this geometry in principle and encourages to perform the same measurements if an external magnetic field is applied.

5.3.2 Interface Vortex Dynamics

In addition to the zero field curve, Fig. 5.4 contains the temperature dependence of $\rho_{1,2}$ and $\rho_{5,6}$ for $\mu_0 H = 3$ T in form of the open symbols. The normal state resistivities for both segments are similar to the zero field measurement, but the superconducting transition is broadened due to the dissipation of vortices in the presence of the external magnetic field. The enhanced pinning properties in the irradiated areas reduce the vortex dissipation yielding a crossover from $\rho_{5,6} < \rho_{1,2}$ to $\rho_{5,6} > \rho_{1,2}$ for temperatures below $T < T^* \approx 73$ K. This is illustrated in the lower inset of Fig. 5.4. In this regime the strongly pinned vortices in the outer segments interact with the weakly pinned flux lines in the unirradiated channel. A changed electric field profile in this temperature regime is detected and shown in Fig. 5.6. In contrast to the normal state $E(l)$ profile where the outer segments represent the regions of high electric fields, the high field region is now established within the weak pinning channel. But compared to the normal state, the local electric field shows a quasi parabolic $E(l)$ dependence and not only two discrete field values are measured. Moreover some of the detected signals do not fit to the field profile systematically which can be attributed to a high contact resistance of the corresponding voltage probes. These points are indicated by an arrow and
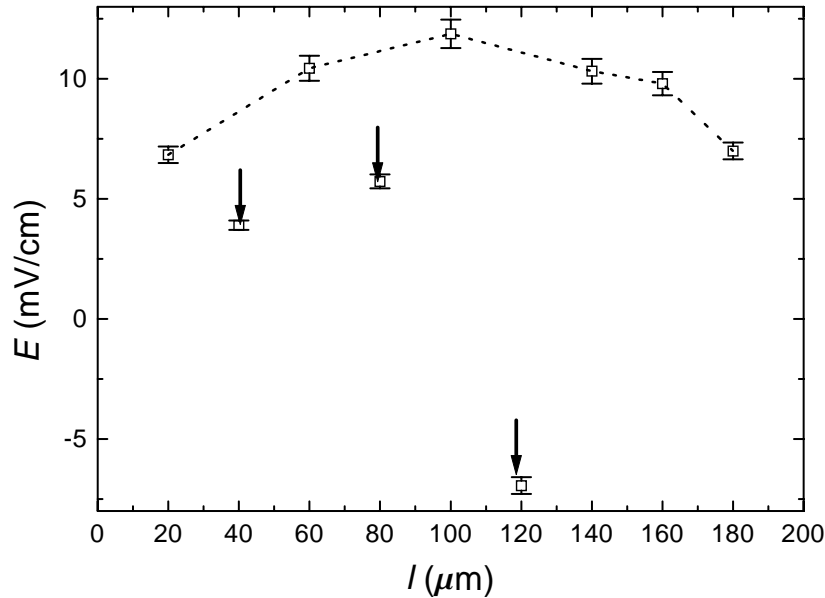

Figure 5.6: *Electric field profile at $T = 69$ K and $\mu_0 H = 3$ T. The dissipation is suppressed in the irradiated parts and compared to the profile in Fig. 5.5 the structure of the profile is much more complex. The data points indicated by an arrow are interpreted as systematic deviations due to a high contact resistance.*

were not taken into account for the analysis of the extracted field profiles. An explanation for the high contact resistances is given in appendix A.

The measured field profiles were fitted to the $E(x, L, \delta)$ behavior of Eq. (1.31). Therefore the middle of segment 5 was defined as $x = 0$ and accordingly, the channel width was re-defined by $L = 160$ μm so that the outer segments $(E_{1,2}, E_{9,10})$ represent the zero electric field level E_0. The bulk resistance ρ_f which is necessary to calculate $E_f = \rho_f J$ is defined as the resistance in the middle of the channel

$$\rho_f \equiv \rho(x = 0) = \rho_{5,6}, \tag{5.2}$$

and $J = 500$ A/cm^2. In addition, the relative error in measuring the electric field was estimated from the individual $\rho_{i,i+1}$ curves to be 5%. Figure 5.7 shows such an analysis for the same data as illustrated in Fig. 5.6. The solid curve represents a fit in accordance with Eq. (1.31) using $E_f = 12$ mV/cm and a viscous length controlling the boundary pinning at the interface between strong and weak pinning regions $\delta = (82 \pm 4)$ μm. The experimental data show an asymmetric behavior with respect to $l = 0$. This deviation is included in the fitted curve by a lateral correction $\Delta x = (-7.5 \pm 3)$ μm. This offset is necessary for the curve fitting because the position of the weak pinning channel is not exactly in the
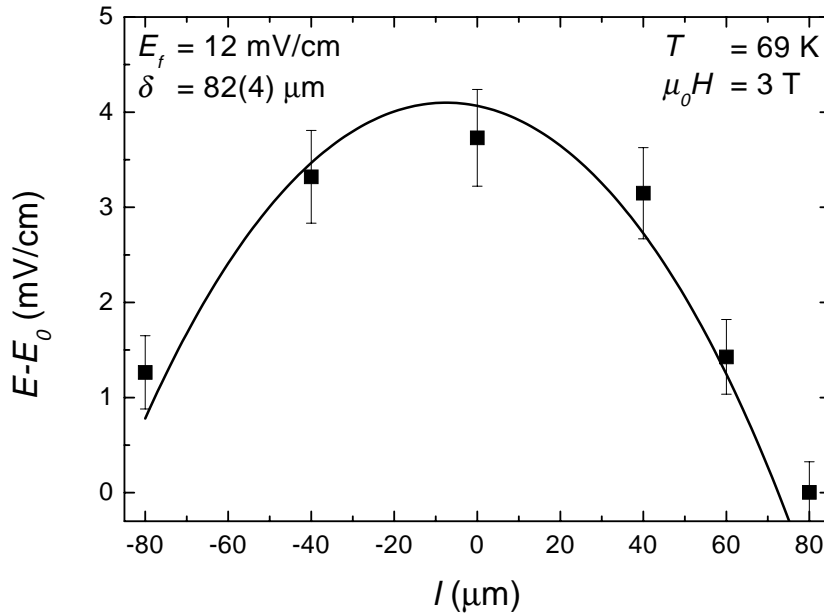

Figure 5.7:   *Hydrodynamic analysis of the electric field profile (T = 69 K, $\mu_0 H$ = 3 T) in accordance with Eq. (1.31). Assuming a bulk field $E_f = 0.012$ V/cm, the viscous length is $\delta = 85 \pm 5$ μm. For this value the fit corresponds to the curve with $\delta/L = 0.5$ in Fig. 1.7.*

middle of the probe array. At the applied magnetic field this value for δ corresponds to approximately 3200 intervortex distances, a value being much larger than the result of Pastoriza *at al.* [54]. In this experiment on $Bi_2Sr_2CaCu_2O_{8+\delta}$ single crystals containing an array of strong and weak pinning channels a correlation length of $\delta \approx 10$ μm was estimated for a magnetic field $\mu_0 H = 50$ mT, corresponding to 50 intervortex distances. This correlation was connected to the divergence of the shear viscosity $\eta(T) \propto \delta^2(T)$ near the vortex lattice melting transition appearing in such clean samples. It was supposed that the described effect is most pronounced if the value for δ is in the order of the channel width. Similar assumptions were made in the context of transport measurements performed on $YBa_2Cu_3O_{7-x}$ single crystals containing twin boundaries [149]. Using the channel flow model [140], a correlation length comparable to the estimated mean separation of twin boundaries in the sample was found. Furthermore, other experiments give hints for strong correlations of the vortex liquid. The measurements were performed on $Bi_2Sr_2CaCu_2O_{8+\delta}$ single crystals in the Corbino disk geometry [58] as well as on $YBa_2Cu_3O_{7-x}$single crystals using a multiterminal geometry [150]. In both cases these correlations are maintained over more than 30 μm.

All these results demonstrate that the interaction between vortices is characterized by a long range order. Especially the confined geometry experiments discussed in this work give strong hints to the suggestion that intervortex interaction at the *Bose-glass boundaries* yields "adhesion" of the flux liquid to these boundaries, forcing the flux flow velocity to vanish or to become very small. However, a systematic investigation of the temperature and magnetic field dependence of the correlation length was not possible due to comparatively high contact resistances.

5.4   Concluding Remarks

In summary, a technique of measuring the electric field profile of a weak pinning channel in a strong pinning environment with high lateral resolution was presented in this chapter. The detected local electric field can be described with a hydrodynamic approach of viscous vortex flow, indicating that the flux line liquid in the channel is strongly influenced by the pinned vortices in the irradiated regions. This interaction behaves very similar to the illustrated scenario shown in Fig. 1.6 and is characterized by long range correlations. The typical length scale obtained from independent experiments is in the order of the channel width of the corresponding geometries. Hence, this result supports the assumptions made in the previous chapter in the context of the patterned irradiation of the Hall-structures.

Unfortunately a reduced sample quality as well as the absence of a low contact resistance did not allow a systematic study of the *Bose-glass contact* and to verify the theoretical predictions. In this context two questions are of main interest. First, patterned irradiation described in chapter 4 and *Bose-glass contact* experiments discussed in this chapter were performed on different HTSC thin films that are distinguished by their different anisotropy of the coherence length

$$\gamma = \frac{\xi_{ab}}{\xi_c} \ , \tag{5.3}$$

which is $\gamma \approx 6$ for $YBa_2Cu_3O_{7-x}$ and $\gamma \approx 100$ for $Bi_2Sr_2CaCu_2O_{8+\delta}$ [151], respectively. This anisotropy has an influence on the longitudinal (parallel to the *c*-axis and the applied field) correlation length [152] $\xi_z \propto \gamma^{-1}a_0$, with the inter-vortex distance a_0 defined in Eq. (1.7), and could also influence the transverse correlation length that is investigated here. Otherwise, recent publications and the experiments performed here have shown that the value for δ is affected by the channel width indicating a dependence of the specific geometry and not of the anisotropy . Therefore the *Bose-glass contact* experiment should also be realized on $YBa_2Cu_3O_{7-x}$ thin films in order to answer this question.

Secondly, the connection between the divergence of the shear viscosity η and the Bose-glass transition is not directly proved yet. The use of two independent test bridges as well as the *Bose-glass contact* geometry on the same sample allows to measure all necessary quantities in parallel. Apart from the difficulties in determining the critical exponents encountered in chapter 3, the transition temperatures T_{VG} and T_{BG} can be extracted from the scaling analysis of the test bridge results in order to generate the irreversibility line. An analysis of the electric field profiles detected in the confined geometry can be integrated in this phase diagram enabling to correlate the Bose-glass transition to the δ values and to observe directly the divergence of the localization length $l_\perp$ and of the viscosity of the flux line liquid, provided that the glass picture is valid. In this sense such an experiment represents another access to proof the existence of the Bose-glass phase.

This first investigation of the described geometry and the promising results obtained in this context motivate to continue this kind of experiments. The theoretical description of the interaction between a Bose-glass phase and a vortex liquid was successfully adapted to the experimental results. The improvement of several experimental features is desirable in this context. On the one hand, single phase $Bi_2Sr_2CaCu_2O_{8+\delta}$ thin films showing a sharp resistive transition are necessary to perform a high quality scaling analysis. Such specifications are also valid for $YBa_2Cu_3O_{7-x}$ thin films for which this measurements should be realized either. In addition, improved contact resistances are required enabling the measurement of the different voltages $V_{i,i+1}$ with a better resolution.

Chapter 6

Heat Propagation in HTSC Thin Films Containing Columnar Defects

Aspects of the vortex dynamics at low dissipation levels have been discussed in the previous chapters. Particularly the behavior of the vortex system at interfaces between strong and weak pinning regions was investigated within the framework of the vortex-glass and Bose-glass picture. In the following, the attention is focussed towards another aspect of this phase transition appearing at high dissipation levels. Due to flux flow instabilities in type II superconductors, voltage jumps in the current-voltage characteristics (CVCs) are observed at characteristic fields $B_J(T)$ in this regime [153]. In $YBa_2Cu_3O_{7-x}$, the existence of this high dissipative flux flow instability is remarkably correlated with the transition into the the vortex-glass phase at $B_{VG}(T)$, which manifests itself at low dissipation [154]. It is interesting to check whether this correlation between the glassy phase and the instability is sustained in the presence of columnar defects or not.

The high power dissipation at which these instabilities occur, yields a quasi-particle temperature that is higher than the measured temperature of the bath and a temperature gradient is generated across the sample (including thin film and substrate). While heat in the thin film propagates instantaneously in good approximation, the gradients across the film/substrate interface and across the substrate must be taken into account. The parameters of heat propagation through this part of the system can be tuned by choosing adequate film-substrate combinations. As will be shown, such modifications of the interface properties can also be achieved with heavy ion irradiation.

The experiment described in this chapter concentrates on the study of the influence of heavy ion irradiation on the heat propagation in $YBa_2Cu_3O_{7-x}$ thin film systems. It was mentioned above that the occurrence of a voltage jump in the CVCs is connected to the transition into the vortex-glass phase. In chapter 3,

a shift of the glass transition temperature towards higher temperatures as well as a shrinked vortex liquid phase were reported in the presence of correlated disorder. The correlation between the glass transition and the vortex instability would imply that the voltage jumps in an irradiated sample will be observed at higher temperatures compared to the pristine sample, provided that the external magnetic field remains the same. However, the effect of columnar defects on this instability and on the heat propagation of the system was not yet studied.

An experimental access to the problem of heat propagation in thin film systems is the application of high current pulses and the time resolved measurement of the voltage drop across the sample in the normal state. The known $R(T)$ behavior in this regime is used to extract the time dependence of the sample temperature from the $R(t)$ measurements. This method is described after a brief review of the key points describing the vortex instabilities and a model for the heat propagation. Finally, the results as well as the influence of heavy ion irradiation on the thermal boundary resistance of the film/substrate interface are discussed.

6.1   Vortex Dynamics at High Dissipation Levels

While the competition between pinning forces and the current induced Lorentz-force has been the focus of interest in the study of vortex dynamics in chapters 1 and 3, vortex dynamics at high current densities is characterized by a Lorentz-force that exceeds the pinning forces largely and therefore the flux lines move rapidly across quenched pinning potentials. In this flux flow regime the vortices are subjected to a viscous damping force that is proportional to the vortex velocity resulting in an Ohmic response, i.e. the friction coefficient η is velocity independent. However, at high vortex velocities the bound quasiparticle states can escape from the vortex core yielding a decreased friction coefficient. Larkin and Ovchinnikov (LO) predicted that this mechanism results in a vortex instability manifested as a voltage jump in the CVCs at high flux flow velocities [116]. Above a critical velocity v_{LO}^* the viscous damping force decreases leading to an even higher velocity accompanied by a still lower viscosity, giving rise to the described instability. Such a voltage instability has been observed in low-temperature [155–158] and high-temperature [159–163] superconductors, respectively.

The experimental results show that the voltage jumps are intrinsic to the vortex system and are not artifacts due to thermal runaway and a reasonable agreement between experiment and the LO theory was found [155–160]. However, the critical current at which the voltage jumps occur [155–158,160] and the critical velocity that correspond to the instability [156,158,160,161] exhibit a significant

magnetic field dependence. While this behavior is not predicted by the LO theory, it can be explained by the extensions introduced by Bezuglyi and Shklovskij (BS) [164] in order to interpret the experimental data of classic superconducting indium thin films. They considered the effect of unavoidable heating of quasiparticles due to the finite rate of removing the power dissipated in the samples. The quasiparticles will have a higher temperature T^* compared to the experimentally measured bath temperature T_0. In consequence, two magnetic field regimes, separated by a normalized field B_T, were distinguished. For magnetic fields $B \ll B_T$ with a low vortex density the temperature of the quasiparticles increases proportionally to B but the difference to the bath temperature $\Delta T = T^* - T_0$ is small and the nonequilibrium LO mechanism dominates the vortex instability. In the opposite limit $B \gg B_T$ the quasiparticles have an effective temperature which is substantially higher due to the weak heat removal. Thus, the instability is mainly due to the influence of quasiparticle heating rather than to the LO mechanism.

Considering the HTSCs $YBa_2Cu_3O_{7-x}$ and $Bi_2Sr_2CaCu_2O_{8+\delta}$, this instability shows up in different ways. In the latter compound, experimental evidence for the applicability of the BS theory was found [162,163]. This is clearly different in $YBa_2Cu_3O_{7-x}$. Here the vortex instability occurs only in a well defined region of the (H, T)-phase diagram. This phase boundary[1] appeared to be identical to that of a vortex-glass transition of the vortex system at low dissipation levels. It is this correlation that makes it interesting to investigate the influence of columnar defects on the vortex instability.

A more detailed discussion of the theory and the experiments of vortex dynamics at high dissipation levels with long and short current pulses including the corresponding formulas describing the instability in the LO theory as well as in the BS extension is found in the thesis of P. Voss-de Haan [21].

6.2 Principle of Measurement

When measuring heating effects in HTSC thin films via electronic transport at high dissipation levels, the destruction of the samples should be avoided. If the power dissipated in the sample consisting of a photolithographically patterned measurement bridge is too high, the thin film temperature can be strongly increased under certain conditions yielding an evaporation of the HTSC material. For this reason the heat propagation experiments were performed using pulsed measurements in the normal state.

---

[1]Although time resolved measurements give hints for the absence of a discontinuity in the CVCs of very short current pulses [21], a change in the dynamic response of the flux line system was identified.

The principle of this technique consists of the four-probe determination of the CVCs by applying current pulses $J_0(t)$ on the sample at a fixed temperature and measuring the time responses of the voltage $V(J_0, t)$ across the sample [165,166] with a *Tektronix TDS 420* digital storage oscilloscope. The pulses had a rectangular shape and a length between 15 μs and 20 ms. They were generated by a set-up used for time resolved measurements of the vortex instability in $YBa_2Cu_3O_{7-x}$ thin films [21,167] that was slightly modified as documented in appendix C. The measured $R(t)$ behavior was transformed into a time temperature raise $\Delta T(P, t)$ in the measurement bridge. This temperature difference additionally depends on the power dissipated in the sample. A temperature calibration at low current densities was necessary in order to determine the $R(T)$ behavior. This dependence is monotonous in the normal state and a fit to the experimental $R(T)$ curve in this regime gives a mathematical relation between $V(t)$ and $\Delta T(t)$.

All measurements were performed on the $YBa_2Cu_3O_{7-x}$ thin film T 229 in zero magnetic field. This sample consists of four identical 50 μm wide and 2000 μm long striplines. While one bridge remains unirradiated, two striplines were irradiated with 11.4 MeV/u ^{197}Au ions as described in Ref. [49] in order to create an arrangement of splayed columnar defects consisting of two different irradiation angles $\pm \delta$ with respect to the crystallographic c-axis, each with an ion dose equivalent field of $B_\phi/2$. The remaining bridge was irradiated with $B_\phi = 2$ T and ion tracks oriented parallel to the c-axis. The temperature calibration was carried out for each stripline individually due to slight differences in the $R(T)$ behavior of the four measurement bridges.

6.3   Model of Heat Propagation

The high current pulses applied to the striplines of the sample at a fixed bath temperature T_0 yield an increase of the true film temperature $T(P, t) = T_0 + \Delta T(P, t)$ during the application of the current pulse. In consequence, heat flows in the direction of the heat sink at T_0. This temperature difference consists of three contributions [168]

$$\Delta T(P, t) = \Delta T_F(P, t) + \Delta T_I(P, t) + \Delta T_S(P, t) , \qquad (6.1)$$

that are schematically illustrated in Fig. 6.1.

The first contribution results from a small temperature variation $\Delta T_F(P, t)$ within the film, where thermal diffusion occurs essentially instantaneously. This temperature difference is therefore supposed to be constant and $\Delta T_F(P, t)$ will be neglected.

The temperature drop across the film/substrate interface is described by $\Delta T_I(P, t)$

On the time scale of nanoseconds [169], phonons transfer heat across this boundary the film/substrate interface. As in the case of ΔT_F, the time scale of the establishment of this temperature drop was not accessible with the used experimental set-up. On larger time scales this second contribution shows up as a constant contribution which is defined by a thermal boundary resistance R_{bd} [170]

$$\Delta T_I(P) = \frac{P}{A} R_{\mathrm{bd}} \; , \tag{6.2}$$

where P/A represents the power dissipated into the system per unit area. Finally as the heat pulse propagates through the substrate, resulting in a third component to the total temperature drop $\Delta T_S(P,t)$. The time evolution of this contribution is a special solution of the differential equation of heat conduction in three dimensions

$$\frac{\partial^2 T}{\partial x^2} + \frac{\partial^2 T}{\partial y^2} + \frac{\partial^2 T}{\partial z^2} = \frac{1}{D}\frac{\partial T}{\partial t} \; , \tag{6.3}$$

with the substrate thermal diffusion constant D. Assuming that the measurement bridge represents a continuous line source of heat and that the heat flows only in the direction perpendicular to the ab-plane of the thin film, indicated by an arrow in Fig. 6.1, Eq. (6.3) can be solved for the case of surface heating with a constant heat supply per unit time and unit area $q = P/A$ into an infinite stripe of width w [171]

$$\Delta T_S(q,t) = \frac{2q\sqrt{Dt}}{K\pi^{1/2}}\left\{\mathrm{erf}\left[\frac{w}{\sqrt{4Dt}}\right] - \frac{w}{\sqrt{4\pi Dt}}\mathrm{E_i}\left[-\frac{w^2}{4Dt}\right]\right\} \; . \tag{6.4}$$

Here, K is the heat conductivity of the substrate and the functions $\mathrm{erf}(x)$ and $\mathrm{E_i}(x)$ are known as the "error function"

$$\mathrm{erf}(x) := \frac{2}{\sqrt{\pi}}\int_0^x e^{-\xi^2}d\xi \; , \tag{6.5}$$

and the exponential integral

$$-\mathrm{E_i}(-x) := \int_x^\infty \frac{e^{-u}}{u}du \; , \tag{6.6}$$

respectively.

This model simplifies the real situation of heat propagation across the film/substrate system. An additional contribution to the temperature variation $\Delta T(P,t)$ arises from the thermal coupling between the substrate and the sample holder which is
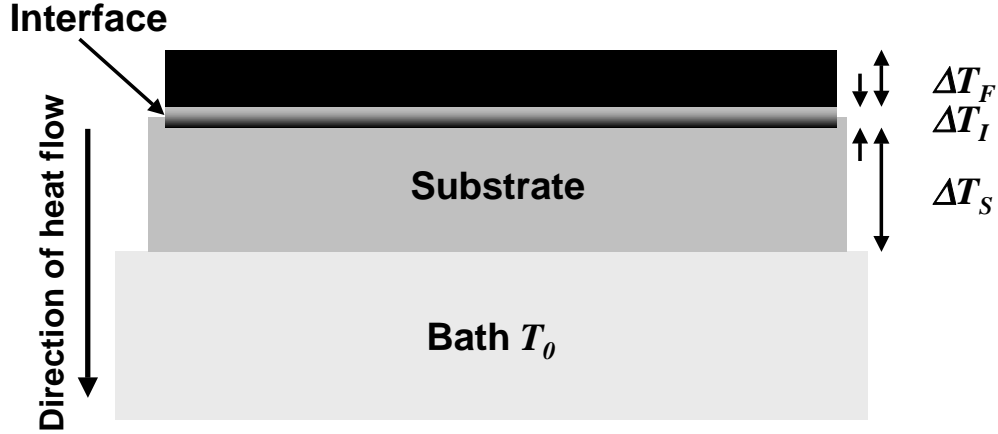
Figure 6.1:   *Different contributions to the heat propagation arising from Eq. (6.1). Only the heat transfer across the film/substrate interface ΔT_I and through the substrate ΔT_S are relevant for the fitting of the experimental results. The arrow on the left side of the illustration indicates the direction of heat flow. Drawing is not to scale.*

of the form of Eq. (6.2). Furthermore the influence of heavy ion induced columnar defects on the time evolution of the temperature difference is not explicitly included. In the fitting of the experimental data these contributions will particularly affect the true temperature on time scales of the order of the durations of the pulses applied in this experiment. Therefore, the temperature drop across the substrate will contain the influence of these contributions implicitly.

6.4 Experimental Results

Measurements of the temperature dependent film resistivity were carried out on the described bridges with a film thickness of 290 nm at current densities $J \approx 70$ A/cm^2 in order to calibrate the functional $\rho(T)$ dependence. Figure 6.2 shows the result of the zero field measurements for the pristine and the irradiated striplines, respectively. The $\rho(T)$ curves are identical to the results obtained earlier [49] on the same sample and indicate that T_c is only weakly influenced neither by the presence nor by the configuration of columnar defects. Again an increased normal state resistivity is observed and one should expect that the curves of the three striplines irradiated with a total ion dose $B_\phi = 2$ T coincide.
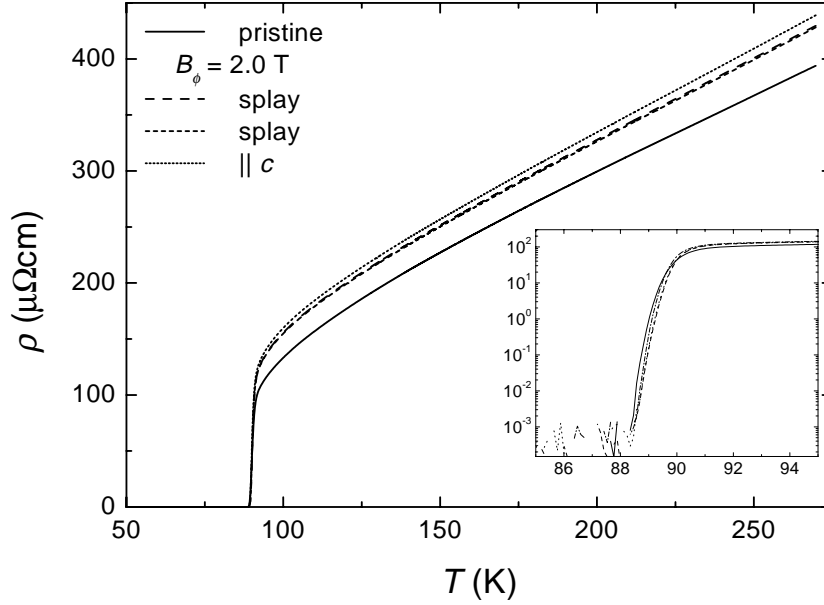
Figure 6.2:   *Resistive transitions of the thin film* T 229 *at low current densities in zero magnetic field. This* $\rho(T)$ *is identical to earlier results obtained on the same film [49]. For the four striplines, three different curves are observed: the pristine bridge, the two striplines irradiated in the splay configuration and finally the measurement bridge with columnar defects oriented parallel to the crystallographic c-axis. Heavy ion irradiation does weakly affect the transition temperature.*

However, the resistivity in the splayed configuration differs from the value of the stripline where the columnar defects are oriented perpendicular to the film surface. If the increase of resistivity with increased ion dose is a volume effect [96], the reduced ρ in the splayed configuration is connected to a reduced volume occupied by the columnar defects. This assumption takes into account that ion tracks generated at different angles $\pm \delta$ can cross each other yielding a region of common volume and reducing the total volume of damaged material.

Returning to the pulsed measurements, Fig. 6.2 also shows that the sample is in the normal state at $T = 100$ K for all striplines so that this value determines the bath temperature T_0. Current pulses were generated with a *HP 33120A* 15MHz Function Generator. For a pulse height of $I_0 \approx 10$ mA, corresponding to a current density $J_0 \approx 6.6 \cdot 10^4$ A/cm^2, the time evolution of the current pulse is illustrated in Fig. 6.3. Its shape has a nearly rectangular form with a raise and fall time $t_r = t_f < 4$ μs which is negligible compared to the pulse duration $\tau = 70$ μs. The voltage response $V(t)$ across the sample is also shown in this representation. It follows the current pulse qualitatively except for the raise and fall times where the voltage drop attains the plateau region $V = 2$ V and $V = 0$ after a short
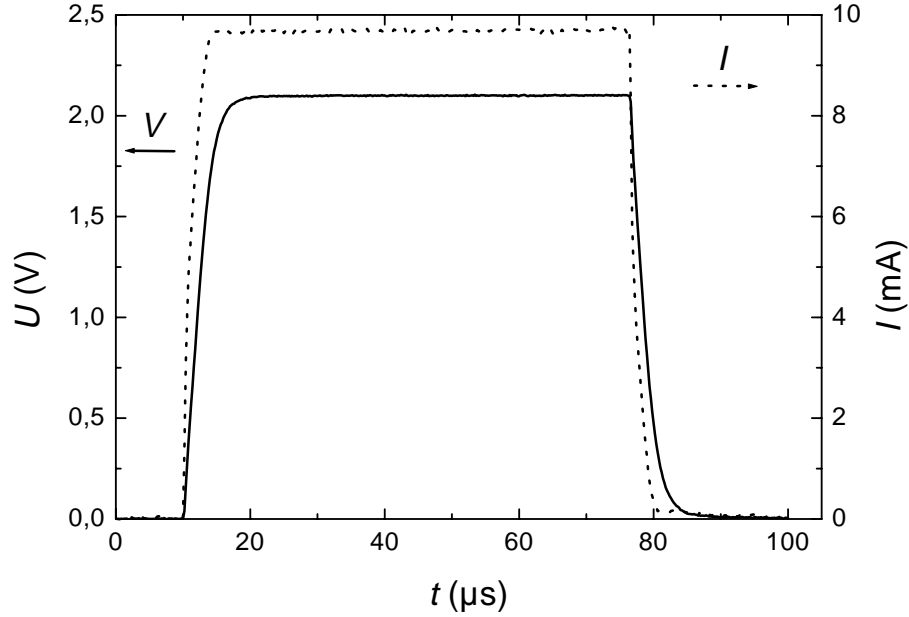
Figure 6.3: *Shape of the current and voltage pulses observed in the pulsed measurements for a current pulse height $I_0 \approx 10$ mA and $T_0 = 100$ K. The dotted line represents the time evolution of the current pulse (right axis). The simultaneously measured time dependent voltage $V(t)$ drop across the sample (left axis) is displayed as a solid line.*

delay with respect to the current pulse. For low current levels, no heating effects are observed in the $V(t)$ evolution. The application of current pulses with higher I_0 changes the shape of the $V(t)$ curves. In this case the plateau is replaced by a continuous increase of the voltage with time indicating a continuous heating of the sample during the complete current pulse duration due to an insufficient heat removal revealing from the contributions $\Delta T_I(P)$ and $\Delta T_S(P,t)$.

Figure 6.4 illustrates the time dependence of the extracted temperature differences between bath and sample $\Delta T(t)$ of the pristine bridge (circles) and one of the irradiated striplines (squares) for a power $P \approx 0.2$ W dissipated in the film. This method of temperature calibration can be carried out for any power level if the $\rho(T)$ dependence is unique. This $\Delta T(t)$ dependence was analyzed within the framework of the heat propagation model described in the previous section. Two features that distinguish the heat propagation properties in the different measurement bridges are observed in this illustration. On short time scales the irradiated stripline has a higher ΔT offset compared to the pristine case. In addition, the slope of the $\Delta T(t)$ dependence is larger in the irradiated case on time scales comparable to the pulse length that is 17 ms in this case. This observation gives hints for better heat propagation properties in unirradiated samples. A more illuminating picture is gained if the experimental data
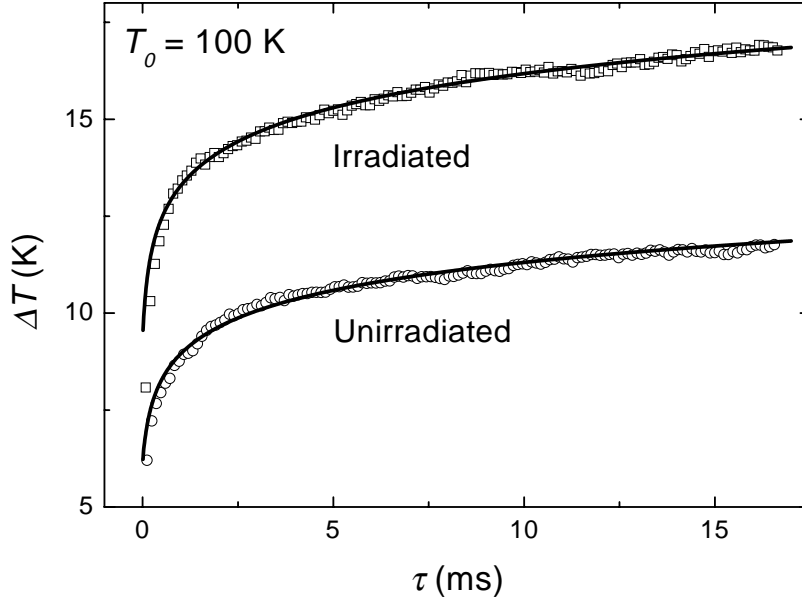
Figure 6.4: *Time dependence $\Delta T(t)$ for a bath temperature $T_0 = 100$ K. The open symbols represent the extracted temperature differences for the irradiated (squares) and unirradiated (circles) stripline. The solid lines show a fit to the described model (6.4) using K, D and an additional offset for short time scales as fitting parameters. This offset is the temperature difference across the film/substrate interface. This thermal boundary resistance extracted from the offset differs between the pristine and the irradiated case and indicates a strong irradiation effect.*

are compared to the corresponding fits (solid lines) that include the contributions ΔT_I described by Eq. (6.2) and ΔT_S from Eq. (6.4). Suitable fitting is achieved if the thermal boundary resistance R_{bd}, the heat conductivity K and the thermal diffusion constant D of the substrate are chosen as summarized in table 6.1. The obtained parameters are in agreement with the reported values

Table 6.1: *Heat propagation characteristics of the pristine and an irradiated stripline. The underlying model is fitted to the experimental results in Fig. 6.4. The model curve matched the experimental results if the listed values for the thermal boundary resistance R_{bd} of the film/substrate interface as well as the heat diffusion constant D and the heat conductivity K are used.*

	pristine	irradiated
R_{bd} (K cm^2/W)	$26.3 \cdot 10^{-3}$	$36.5 \cdot 10^{-3}$
K (W/(cm K))	0.13	0.125
D (cm^2/s)	0.25	0.40

for the propagation properties. For the thermal boundary resistance a value $R_{\mathrm{bd}} = 10 \cdot 10^{-3}$ (K cm^2/W) was reported [169], even if the majority of the results are of the order of $R_{\mathrm{bd}} = (1 \pm 0.5 \cdot 10^{-3}$ (K cm^2/W) [170,172–176]. The reported value for the thermal conductivity is $K = 0.1$ (W/cm K) for SrTiO$_3$ [177] and $D = 0.25$ (cm^2/s) [178] for the diffusion constant in LaAlO$_3$.

Table 6.1 indicates that the thermal boundary resistance is increased by approximately 40% after the introduction of columnar defects. Additionally, the fitting of the experimental data with Eq. (6.4) reveals a change of the heat diffusion constant in the substrate in the presence of columnar defects. It was mentioned in the context of the applied heat propagation model that irradiation effects are not considered so that the following discussion will be concentrated particularly on the irradiation effects on the structure of the YBa$_2$Cu$_3$O$_{7-\mathrm{x}}$/SrTiO$_3$ interface.

Figure 2.2 illustrates that the electronic energy loss S_e in YBa$_2$Cu$_3$O$_{7-\mathrm{x}}$ is constant on length scales that oversize the typical film thickness so that the ions reach the interface with an energy which is of the order of the initial ion energy. It is therefore realistic to assume the creation of columnar defects across the film/substrate interface and in the substrate. Due to the thickness of the SrTiO$_3$ ($d \approx 1.1$ mm) the ions will be stopped in the substrate yielding the generation of columnar defects within a "defect layer" of thickness $d_{\mathrm{CD}} \ll d$. TEM investigations showing hat the columnar defects reach deep into the substrate [35,79] prove the correctness of this assumption. Heat propagation in insulators is mainly carried by phonons and a perfect crystalline structure promotes heat conduction. An epitaxial YBa$_2$Cu$_3$O$_{7-\mathrm{x}}$ thin film on a SrTiO$_3$ substrate has nearly no mismatch between the lattice constants of both materials in the crystallographic ab-plane and therefore phononic excitations can propagate nearly undisturbed across the film/substrate interface. Heavy ions generate columnar tracks of amorphous material and the perfect crystalline structure is destroyed locally. This reduces the phononic coupling between film and substrate and increases the interface thermal boundary resistance. In addition, Fig. 2.2 shows that the projected range for ^{238}U ions with an energy of 11.4 MeV/u is approximately 60 μm. Au ions with the same energy generate similar tracks and at the end of the ion trajectories deep in the substrate the nuclear energy loss will generate a amorphous defect layer that separates crystalline and distorted regions of the substrate. Therefore the effective film/substrate interface region is extended and the boundary between crystalline and distorted substrate additionally contributes to R_{bd}.

Within this context an additional ion irradiation effect at interfaces between film and substrate or between subsequent layers of heterostructures should be mentioned. If the swift ions traverse these regions this often results in the inter-mixing of the atoms forming the interfaces and sometimes even in the formation of new phases in the interfacial region. This effect and the underlying atomic transport is called *ion beam mixing* and was first recognized in 1972 by Lee *et al.* [179]

and by Van der Weg *et al.* [180]. Such effects gained a widespread interest because of its technological potential for preparation and processing of new materials with novel properties [181,182] and are based on the thermal spike model discussed in section 2.2. The high local temperatures that are achieved in the vicinity of the projectile ion when passing through the target yield a transient diffusion process in the molten material, which give rise to the atomic intermixing. With respect to the heat propagation process, atomic mixing is implicitly contained in the thermal boundary resistance R_{bd}, but a quantitative analysis is rather difficult. XRD, together with cross-section transmission electron microscopy (XTEM) are commonly used for the phase analysis of ion mixed samples. Another non-destructive way to determine the concentration profiles across the interfaces of the pristine and the irradiated samples is carried out by using beam analysis techniques like Rutherford backscattering or resonant nuclear reactions analysis. A detailed description of these techniques can be found in Ref. [183]. Although these analyzing methods were not applied in this work, the characterization of the samples with regard to the described effects remains interesting for future investigations.

6.5   Consequences of Heat Propagation

The described experiments were initiated in order to check heating effects within the context of the vortex instability at high dissipation levels. Due to correlations between the detection of the characteristic voltage jump and the vortex-glass transition at low currents in $YBa_2Cu_3O_{7-x}$, both effects should be modified in the same way in the presence of columnar defects if no opposite irradiation effects must be included. But the above discussed results show that there is a competition between enhanced pinning and reduced heat propagation properties. The reduced heat transfer across the film/substrate interface considerably influences temperature dependent quantities, provided that the heat propagation properties do not change drastically in the superconducting state $T < T_c < T_0$.

Pulsed measurements of the voltage drop across microbridges at high current densities are an efficient method to detect the temperature difference of the film with respect to a fixed bath temperature. If the temperature of the resistivity at low current densities shows a monotonous behavior, it is possible to extract the true temperature for any power dissipated into the sample from this $R(T)$ behavior. A brief discussion of the heat propagation process in $YBa_2Cu_3O_{7-x}$ thin films on $SrTiO_3$ substrates at $T_0 = 100$ K shows a strong influence of heavy ion induced columnar defects on the heat propagation properties of the system. Mainly the thermal boundary resistance describing the heat propagation across the film/substrate interface is affected by the columnar tracks and yields an enhanced value after irradiation. This effect can be understood in terms of the

locally destroyed phononic coupling at the interface due to the amorphous material in the tracks. To what extend an ion beam mixing effect contributes to enhancement of R_{bd} could not be quantified, but this mechanism should be taken into account.

Further experiments are required to get a more detailed image of the effects which are important at high dissipation levels and the method presented here is only one experimental access. TEM studies combined with energy dispersive X-ray analysis at a high lateral resolution could provide additional information about the local structure of the film/substrate interfaces, in the center of the columnar tracks and within the amorphous defect layer of the substrate. In Addition, the use of other substrates, which have different heat conduction properties and a higher mismatch to the lattice parameters of $YBa_2Cu_3O_{7-x}$ in the crystallographic *ab*-plane like MgO and $LaAlO_3$ instead of $SrTiO_3$, is one possible way to illuminating answers. Apart from this, a systematic investigation of the ion dose and temperature dependence of the heat propagation quantities would be helpful.

Conclusions

Collective vortex pinning mechanisms of high-temperature superconductor (HTSC) thin films in the presence of heavy ion induced columnar defects were investigated in this work. The dynamics of magnetic flux lines was probed by the use of electronic transport measurements in various irradiation geometries in order to study the interaction between vortices and correlated pinning centers and to obtain information about the typical length scales of the interaction between flux lines.

In a first part, the temperature and magnetic field dependence of the current-voltage characteristics (CVCs) was determined and the experimental results were scaled within the framework of the Bose-glass model. This ansatz describes the universal critical behavior of the vortex system at the second order transition from a flux line liquid to a glass phase in the presence of correlated disorder. The use of long microbridges allowed to measure the CVCs with a high electric field sensitivity. Scaling analysis reveal a strong dependence of the dynamic critical exponent on the electric field range and the applied external magnetic field. These results are conform to the results on unirradiated samples from which a similar analysis for quenched point disorder was performed within the framework of the vortex-glass model. The observed behavior is inconsistent with the predictions of the underlying glass scaling ansatz, independent from the pinning properties. Investigations of the current dependence of the activation energy additionally casted doubts on the existence of a Bose-glass phase. The barrier height should diverge in the limit of low currents, but the experimental data showed no evidence for this feature. In this context the increase of the electric field sensitivity will be the great challenge, because this is considered as *the* key for a successful solution of the problem. The results presented here are a small contribution on this way, but cannot give a decisive answer.

It could also be shown that the scaling analysis of the CVCs can be used to identify the glass phases in the (H,T)-plane. In comparison to the pristine sample, the irreversibility lines of the irradiated sample exhibits two regimes. For low magnetic fields, the interaction between flux lines and columnar defects dominates the vortex dynamics, whereas collective vortex creep mechanisms play an important role at high fields.

Interactions between flux lines in confined geometries have been the topic

of the second part of this work. It could be shown that the spatially resolved heavy ion irradiation through Ni-masks is an effective method to create geometric arrangements of strong and weak pinning with sharp interfaces between both regions. Two different experiments were carried out in such restricted pinning geometries.

At first, magnetoresistive measurements were performed on a Hall-structure irradiated periodically with strong and weak pinning channels that form an angle of 45° with respect to the symmetry axis of the photolithographycally patterned structure. The magnetic field dependence of the even transverse voltage shows a striking resemblance to the results observed in $YBa_2Cu_3O_{7-x}$ single crystals containing an array of unidirected twin boundaries which are interpreted as a guided vortex motion. The use of two additional test bridges allowed to determine in parallel the resistivities of the irradiated and unirradiated parts as well as the CVCs. These measurements provided the input parameters for a numerical simulation of the potential distribution of the Hall-patterning. The experimentally observed magnetic field dependence of the transverse voltage vanishes faster than expected from the numerical calculation. These results were interpreted within the framework of a *Bose-glass contact* that describes the hydrodynamic interaction between a Bose-glass phase and a vortex liquid. The positions of the characteristic features of the magnetic field dependent even transverse voltage in the (H, T)-phase diagram that was constructed with the irreversibility lines resulting from the scaling analysis of the test bridge CVCs support this interpretation. In addition, the numerical simulation shows that the electrical current is directed perpendicular to the weak pinning channels in the presence of an external magnetic field. The induced anisotropic Lorentz-force density supports the existence of a *Bose-glass contact*. In the discussion of the guided vortex motion effect in the twin boundary experiments this fact was not taken into account because guiding is a consequence of the anisotropic pinning force density of the twin boundaries in this case.

It is the interaction between vortices pinned by columnar defects in the strong pinning channels and the weakly pinned flux lines in the unirradiated channels that influences the dynamics of the vortex system. Particularly at the interface between strong and weak pinning regions this effect yields a freezing of flux lines in the absence of columnar defects and a strongly varying vortex velocity profile in the weak pinning channels. The direct measurement of such a profile was realized for the first time in a second step. A *Bose-glass contact* was prepared for $Bi_2Sr_2CaCu_2O_{8+\delta}$ thin films and the local variation of the electric field in a 115 μm wide weak pinning channel embedded in a strong pinning environment was measured with the use of 10 voltage probes. In the presence of an external magnetic field the detected electric field profile shows a lateral structure that is caused by interactions of vortices on the strong/weak pinning interfaces. In the

hydrodynamic approach of the *Bose-glass contact*, the local electric field depends on a viscous length that describes the range of interaction between strongly and weakly pinned vortices. The described experiment allows to extract this typical length scale which is of long range order.

The quintessence of the confined pinning geometry experiments can be summarized as follows: the typical length scale of the vortex-vortex interaction at the interfaces between strong and weak pinning regions is in the order of the width of the weak pinning channel, in accordance with recent results reported in literature. As the channel width in the described experiments was in the order of 100 μm, these results indicate correlations which sustain over many intervortex distances. Direct measurements of the vortex flow profile in $YBa_2Cu_3O_{7-x}$ thin films are still missing and a systematic investigation of the magnetic field and temperature dependence of the viscous length should be carried out. The theory predicts that this correlation length is the Bose-glass length $l_\perp$ and therefore the divergence of the viscous length would be a supplementary proof for the existence of a Bose-glass phase, together with the scaling analysis of the CVCs. The perfect measurement geometry for such an experiment would consist of a sample that contains a completely irradiated long measurement bridge and a stripline with as many as possible voltage probes on a small length scale in order to measure *in parallel* the CVCs with a high electric field sensitivity and the electric field profile with a high lateral resolution. This work has shown that this is a nontrivial task.

For the first time microprobe irradiations were performed on HTSC thin films. Even if this technique must be improved with respect to the desired irradiation pattern, the first results on $YBa_2Cu_3O_{7-x}$ thin films revealed that the use of the microprobe opens new perspectives. Apart from the reproduction and the improvement of experiments described in this work, the microprobe can be used to generate any irradiation pattern with dimensions in the micrometer range would lead to various fascinating new results. Experiments in the DC flux transformer geometry are only one example for such an application of the microprobe.

In addition to the discussed effects on vortex dynamics that appear at the interface between strong and weak pinning regions, the heat propagation across the film/substrate interface was one topic of this work. A method allowing to extract the true sample temperature from the $\rho(T)$ characteristics was used in this context. It could be shown that it is possible to modify the thermal boundary resistance of this interface via heavy ion irradiation. The swift ions create continuous columnar tracks of amorphous material across the whole HTSC thin film, across the film/substrate interface and inside the substrate. In comparison to an unirradiated sample, this effect reduces the thermal coupling between substrate and film as well as in the damaged layers of the substrate, visible as an increased thermal boundary resistance in comparison to the unirradiated sample.

The pulsed measurements performed in this context were intended to prepare the investigation of flux flow instabilities at high dissipation levels in the presence of columnar defects. It was expected that an enhanced pinning would shift the characteristic voltage jumps towards higher current densities provided that heating effects in irradiated samples remain unaffected. The latter assumption does not hold up in the studied $YBa_2Cu_3O_{7-x}/SrTiO_3$ system. The competition between both effects has to be considered for a further investigation of the vortex instability in the presence of columnar defects.

These experiments reveal the importance and the efficiency of heavy ion induced columnar defects for the investigation of vortex dynamics in HTSCs. This work pointed out new concepts for the use of columnar pins and in particular their application in confined geometries has proved to be a powerful tool in this field of research. The questions that raised during the interpretation of the results motivate to continue the microprobe irradiation experiments as well as to carry out a systematic study of the flux line dynamics in the *Bose-glass contact* geometry. These investigations are a key for a better understanding of the collective effects and vortex-vortex interaction.

This work is one contribution to it.

Appendix A

Preparation Parameters

A.1 Target

For a 2 inch diameter target of $Bi_{2.05}Sr_2CaCu_2O_{8+\delta}$ approximately 20 g of the basic product is necessary. The surplus of the Bi-compound in the original target composition results from the high vapor pressure of Bi and a relatively high loss of this compound during the deposition process. A stoichiometric value of 2.05 was determined as the optimum value where the best films could be prepared [65]. Table A.1 summarizes the different basic compounds. The target composition for $YBa_2Cu_3O_{7-x}$ is found elsewhere [184].

Table A.1: *Composition of the $Bi_{2.05}Sr_2CaCu_2O_{8+\delta}$ targets. High purity base compounds were used in order to get 20 g of the initial target material.*

Compound	Mass (g)
Bi_2O_3	9.2556
$SrCO_3$	5.7218
$CaCO_3$	1.9396
CuO	3.0830

The well mixed composition was filled in a combustion tray made of (Al_2O_3). The calcination and sintering, respectively were performed in a furnace ($UAF15/5$) of *Lenton Thermal Designs Ltd.* as listed in table A.2. In addition, table A.2 contains the parameters for mortaring, milling and molding of the target. During this preparation step it is important to observe the constitution of the target material. If the chosen temperatures for calcination and/or sintering are too high, the target will melt partially yielding a loss of Bi and a non-stoichiometric composition. The preparation of thin films with such a target will result in samples with a reduced superconducting transition temperature and a bad homogeneity of the films.

Table A.2: *Sinter parameters for* $Bi_2Sr_2CaCu_2O_{8+\delta}$ *targets. The sweep rates for heating and cooling of furnace were set to* 15 °C/min *for the calcination and* 10 °C/min *for the sintering, respectively.*

Step	Parameters
Calcination 1	at 760 °C for 12 h
Mortaring	Fine powder, free of grains
Calcination 2	at 760 °C for 12 h
Ball Milling	Level 8 for 30 h
Molding	approx 15 g with 20 tons
Sintering	at 790 °C for 24 h

In a last step the new target is glued into a target holder made of copper using a two component polymer based silver glue (*Ecobond 56 C* and *Catalyst 9* of *Grace Company* with a ratio of 20:1). In order to obtain a good thermal and electric coupling between target and holder the system is finally heated for 2 h at a temperature of 110 °C.

A.2   HTSC Thin Films

The parameters for the preparation of $YBa_2Cu_3O_{7-x}$ and $Bi_2Sr_2CaCu_2O_{8+\delta}$ thin films are listed tables A.4 and A.3, respectively. These values correspond to the optimized values that were obtained during several preparation cycles. $SrTiO_3$ substrates with a thickness $d \approx 1.3$ mm were used for the preparation of both HTSC systems. If other substrates are used, the deposition temperatures T_{Dep} must be re-optimized. For example, $T_{Dep} = 810$ °C for $Bi_2Sr_2CaCu_2O_{8+\delta}$ on $LaAlO_3$ substrates.

Table A.3:   *Optimized parameters for the deposition of epitaxial* $Bi_2Sr_2CaCu_2O_{8+\delta}$ *thin films.*

Step	T (°C)	p (hPa)	t (min)
Pre-sputtering	$600 \mapsto 835$	3.3	15
Deposition	835	3.3	120
Post-annealing 1	835	3.75	30
Post-annealing 2	500	0.45	30

Table A.4: *Optimized parameters for the deposition of epitaxial* $YBa_2Cu_3O_{7-x}$ *thin films.*
*) *Pressure in an* $Ar : O_2 = 2 : 1$ *atmosphere.*
†) $\Delta T = -30\,°C/min.$

Step	T (°C)	p (hPa)	t (min)
Pre-annealing	895	3	30
Pre-sputtering	840	3*)	15
Deposition	840	3*)	120
Post-annealing 1	$680 \overset{\Delta T^{†)}}{\mapsto} 550$	900	
Post-annealing 2	550	900	30
Post-annealing 3	$550 \overset{\Delta T^{†)}}{\mapsto} 20$	900	

A.3 Contact Pads

In a first step Au ($YBa_2Cu_3O_{7-x}$) or Ag ($Bi_2Sr_2CaCu_2O_{8+\delta}$) contact pads with a diameter of ≈ 1 mm were evaporated onto the respective films in a vacuum chamber through metal masks. The basic pressure of this chamber was 10^{-4} hPa.

Low Contact resistances are required if electrical transport measurements are carried out at high current densities in order to avoit heating effects. Therefore the evaporated contact pads were diffused into the HTSC thin films before the photolithographic patterning in a second step.

The diffusion process for $YBa_2Cu_3O_{7-x}$ thin films is summarized in table A.5. It is important to note that the sample must be heated to $T = 650$ °C within a short time ($t < 4$ min) at a pressure of approximately 10^{-5} hPa. This fast processing reduces the oxygen losses in the film due to high temperatures and low pressures.

Table A.5: *Parameters used for the evaporation of Au contact pads in* $YBa_2Cu_3O_{7-x}$ *thin films. The annealing steps are carried out in an oxygen atmosphere.*

Step	T (°C)	p (hPa)	t (min)
Diffusion	$30 \mapsto 650$	10^{-5}	4
Annealing	650	900	0
	$650 \mapsto 550$	900	6.5
	550	900	30
	$550 \mapsto 30$	900	36

For $Bi_2Sr_2CaCu_2O_{8+\delta}$ thin films, the diffusion process of Ag contact pads is described in Ref. [49]. However, the application of this parameters yielded a

drastical reduction of T_c due to a high loss of oxygen during the heating procedure. Attempts to optimize in particular the subsequent annealing steps failed. In consequence, the Ag contact pads were not diffused into the film and the relatively high contact resistance of these systems was accepted. This procedure can be applied for electrical transport measurements at relatively low current densities.

A.4   Photolithography

Photolithographic steps were applied in the way summarized in table A.6 in order to generate the measurement structures described in this work. The listed parameters were applied under cleanroom conditions. The light for the exposure step was provided by a mercury lamp. A detailed experimental review of the use of other photoresists as well as alternative micropatterning techniques is found in previous works [185,186].

Table A.6:   *Photolithographic parameters for* $Bi_2Sr_2CaCu_2O_{8+\delta}$ *and* $YBa_2Cu_3O_{7-x}$ *thin films using chemical wet etching.*

Step	$YBa_2Cu_3O_{7-x}$	$Bi_2Sr_2CaCu_2O_{8+\delta}$
Photoresist	*AZ* 6612	*AZ* 6612
Spin Coating	30 s at 6000 t/min	30 s at 6000 t/min
Light Exposure	29 s	15 s
Developing Agent	NaOH, 0.1 M	$\frac{2}{3}$ NaOH, 0.1 M; $\frac{1}{3}$ NaOH, 0.5 M
Developing Time	35 s	25 s
Etching	21 s in $HNO_3(1:400)$	30 s in $HNO_3(1:400)$

Appendix B

Network Calculation

The following program developed with the Matlab (v 5.1) software was used for the network calculations described in chapter 4. All comments in this algorithm are in German language. Figure B.1 shows a small part of the matrix representation of the 1:4 ratio structure. The original 280×160 matrix representation of the 2×7 mm^2 Hall-structure must be inserted instead of **NETWORK**.

```
% Netzwerkanalyse
% Matrizen in Sparse

% Zu berechnende Widerstandsverhältnisse
% Nur Potentiale am oberen Rand werden berechnet!
% Volle Rechnung siehe Netzwerk.m
% hier so modifiziert, das Randwiderstaende links und rechts
% =0 sein müssen!

% Die Rohdaten sollten in der folgenden Form aufbereitet werden:
% 1.  Spalte:  Temperatur oder Widerstand
% 2.  Spalte:  Spannung des bestrahlten Teststeges
% 3.  Spalte:  Spannung des unbestrahlten Teststeges
%
% In die Berechnungen sollte auch die Geometrie der Teststege eingehen
% Vorgehensweise:
% Geometrie des Teststeges an die der Hall-Struktur anpassen
%       Hall:  1 Matrixelement == 25 µm in diesem Fall
%       => für Teststeg:   200 × 2000µm² <=> 8 × 80 Matrix
%
%       Berechnung des Widerstandes
%       R = (d/l) * (U/I) = (8/80) * (V/I_ test) = V/(10*I_ test)
%       I_ test:  Stromstärke für Teststege
%
%       Später muss dann der normierte Strom mit der Stromstärke der
%       Hall-Struktur multipliziert werden!!!
```

```
% Stromstärken definieren

% Teststege in Ampere
I_ test=1E-4
% Hall-Struktur in Ampere
I_ hall=1E-3

load export.dat;

T_ vektor=export(:,1); %Temperaturen
A_ vektor=export(:,2); % bestrahlter Referenzsteg
B_ vektor=export(:,3); % unbestrahlter Referenzsteg

% Schleife
for counter=1:length(T_ vektor),

% Zweigwiderstaende A,B, wie in Skizze
T=T_ vektor(counter); % Temperatur
A=A_ vektor(counter); n=A/(10*I_ test); % Bestrahlter Teil!
B=B_ vektor(counter); W=B/(10*I_ test); % Unbestrahlter Teil
K=1; % K wird nicht benutzt

netzwerk=[NETWORK];

[n,m] =size(netzwerk);
NLoops=((n-1)/2)*(m-1)+1; % Anzahl unabhaengiger Maschen
NRows=(n-1)/2;            % in NRows Reihen
NColumns=m-1;             % und NColumns Spalten
                         % (+1 umlaufende Masche)
Masche=sparse(NLoops,NLoops); % Mit Nullen initialisieren
V=sparse(NLoops,1,1); % Spannungsquellen im Netzwerk
%V(NLoops,1)=1; % Spannung nur in letzter Masche
tic
for k=1:NLoops-1,

    currentRow=mod(k,NRows);
    if currentRow==0, currentRow=NRows; end
    currentColumn=floor(k/NRows)+1;
    if (mod(k,NRows)==0), currentColumn=floor(k/NRows); end

    leftNachbar=k-NRows;
    leftNachbarexists=(leftNachbar>0);
    if leftNachbarexists
        Masche(k,leftNachbar)=-netzwerk(currentRow*2,currentColumn);
    else
        Masche(k,NLoops)=+netzwerk(currentRow*2,currentColumn);
                %Beitrag der Randmasche zu dieser Loop am linken Rand
        Masche(NLoops,k)=+netzwerk(currentRow*2,currentColumn);
                %Beitrag dieser Loop zur Randmasche
```

```
             Masche(NLoops,NLoops)=Masche(NLoops,NLoops)+
              +netzwerk(currentRow*2,currentColumn);
                    %Eigenbeitrag der Randmasche
        end /
        rightNachbar=k+NRows;
        rightNachbarexists=(rightNachbar<NLoops);
        if rightNachbarexists
            Masche(k,rightNachbar)=-netzwerk(currentRow*2,currentColumn+1);
        else
            Masche(k,NLoops)=+netzwerk(currentRow*2,currentColumn+1);
                    %Beitrag der Randmasche zu dieser Loop am rechten Rand
            Masche(NLoops,k)=+netzwerk(currentRow*2,currentColumn+1);
                    %Beitrag dieser Loop zur Randmasche
            Masche(NLoops,NLoops)=Masche(NLoops,NLoops)+
             +netzwerk(currentRow*2,currentColumn+1);
                    %Eigenbeitrag der Randmasche
        end %(if rightNachbarexists)

        topNachbar=k-1;
        topNachbarexists=(currentRow>1);
        if topNachbarexists
            Masche(k,topNachbar)=-netzwerk(currentRow*2-1,currentColumn);
        end %(if topNachbarexists), kein Beitrag der Randmasche oben

        bottomNachbar=k+1;
        bottomNachbarexists=(currentRow<NRows);
        if bottomNachbarexists
            Masche(k,bottomNachbar)=-netzwerk(currentRow*2+1,currentColumn);
        else
            Masche(k,NLoops)=+netzwerk(currentRow*2+1,currentColumn);
                    %Beitrag der Randmasche zu dieser Loop am unteren Rand
            Masche(NLoops,k)=+netzwerk(currentRow*2+1,currentColumn);
                    %Beitrag dieser Loop zur Randmasche
            Masche(NLoops,NLoops)=Masche(NLoops,NLoops)+
             +netzwerk(currentRow*2+1,currentColumn);
                    %Eigenbeitrag der Randmasche
        end %(if bottomNachbarexists)

    Masche(k,k)=+netzwerk(currentRow*2-1,currentColumn)...
                +netzwerk(currentRow*2,currentColumn+1)...
                +netzwerk(currentRow*2+1,currentColumn)...
                +netzwerk(currentRow*2,currentColumn); if (mod(k,500)==0), k, end
end % (for k=1:NLoops-1)
% Ecke links unten, ist hat Beitraege von/zur Randloop von  leftNachbarexists
% die von  bottomNachbarexists ueberschrieben wurden
% Korrektur (hier schneller als in Schleife)
% Beitraege von  leftNachbarexists wieder dazuaddieren
Masche(NRows,NLoops)=Masche(NRows,NLoops)+netzwerk(NRows*2,1);
              %Beitrag der Randmasche zu dieser Loop am linken Rand
```

```
Masche(NLoops,NRows)=Masche(NLoops,NRows)+netzwerk(NRows*2,1);
              %Beitrag dieser Loop zur Randmasche
% analog
% Ecke rechts, ist hat Beitraege von/zur Randloop von  rightNachbarexists
% die von  bottomNachbarexists ueberschrieben wurden
% Korrektur (hier schneller als in Schleife)
% Beitraege von  rightNachbarexists wieder dazuaddieren
Masche(NLoops-1,NLoops)=Masche(NLoops-1,NLoops)+netzwerk(NRows*2,NColumns+1);
              %Beitrag der Randmasche zu dieser Loop am rechten Rand
Masche(NLoops,NLoops-1)=Masche(NLoops,NLoops-1)+netzwerk(NRows*2,NColumns+1);
              %Beitrag dieser Loop zur Randmasche
toc
SetupBeendet=1;
A % zur Anzeige

I=Masche/V;

Ptop=zeros(NRows+1,1);
              %Initialisierung der oberen Netzwerkknoten mit Potential 0
Pbottom=zeros(NRows+1,1);
              %Initialisierung der unteren Netzwerkknoten mit Potential 0

%Potentiale am oberen Rand
forh=1:NColumns-1,
   Ptop(h+1)=Ptop(h)-I((h-1)*NRows+1)*netzwerk(1,h);
end %(for h=1:NColumns-1)
Ptop(NColumns+1)=Ptop(NColumns)-I((NColumns-1)*NRows+1)*netzwerk(1,NColumns);
% Potentiale am oberen Rand

%Potentiale am unteren Rand
for h=1:NColumns-1,
   Pbottom(h+1)=Pbottom(h)+(I(h*NRows)+I(NLoops))*netzwerk(NRows*2+1,h);
end %(for h=1:NColumns-)
Pbottom(NColumns+1)=Pbottom(NColumns)+(I(NColumns*NRows)+I(NLoops))*
   *netzwerk(NRows*2+1,NColumns);
% Potentiale am oberen Rand

PotentialeBerechnet=1
RandPotential=[Pbottom Ptop];

% V war 1 gegeben; I(NLoops)=gesamtstrom;
% auf Strom 1 normieren
% Diese normierten Randpotentiale sind dann noch
   mit der Stromstärke I_ hall zu multiplizieren!
RandPotentialnormiert=RandPotential*I_ hall/I(NLoops);

%Abspeichern
dummy=num2str(T,'[ganz,punktbruch]=strtok(dummy,'.');
bruch=punktbruch(2:length(punktbruch));
```

```
filename=['RPot' ganz '_ ' bruch '.dat'];
save(filename,'RandPotentialnormiert','-ascii')

end;
```


Figure B.1:   *Matrix representation of the irradiated Hall-structure used for the network calculation described in chapter 4. The variable n (W) represents the irradiated (unirradiated) parts of the structure.*

Appendix C

Current Source for Time Resolved Measurements

For the measurement of the time dependent voltage drop across the microbridges at high current densities discussed in chapter 6, fast pulsed currents that cannot be provided with a conventional current source (*Keithley 224*) were required. Therefore a fast voltage driven current source that was constructed in order to study the flux-flow instabilities [167] was used and modified.

The main principle of this current source in its modified form is sketched in Fig. C.1. The sample is connected between a voltage source (+15 V) and the collector of a transistor whose emitter terminal is grounded. The current flow through the sample is adjusted with the use on an operational amplifier (OP1) that is connected to the base of this transistor. The signal form of the current pulse is supplied from a *HP 33120A* 15MHz Function Generator that is connected to OP1. The voltage drop across the sample is measured with an instrumentation amplifier (INA110). Both input signals of this amplifier are divided with the use of a voltage divider that consists of two 100 kΩ resistors. In order to measure in parallel the current flowing through the microbridge, the voltage drop across a 10 Ω metal-film resistor was probed. The signal was processed in the same way as the voltage drop across the sample. The time dependence voltage and current signals were measured on two different channels of a *Tektronix TDS 420* digital storage oscilloscope. A more detailed description of the measurement circuit as well as of the principle of the pulsed and time resolved measurements is found in earlier publications [166,167].

Compared to the original construction of this electronic circuit, two main changes were implemented in this set-up. First, the 10 Ω metal-film resistor that is connected between the sample and the collector of the transistor is used to monitor the current instead of a 50 Ω resistor connected between emitter of the transistor and the mass connection. Due to this change the current can be measured more subjectively because the influence of an additional base-emitter
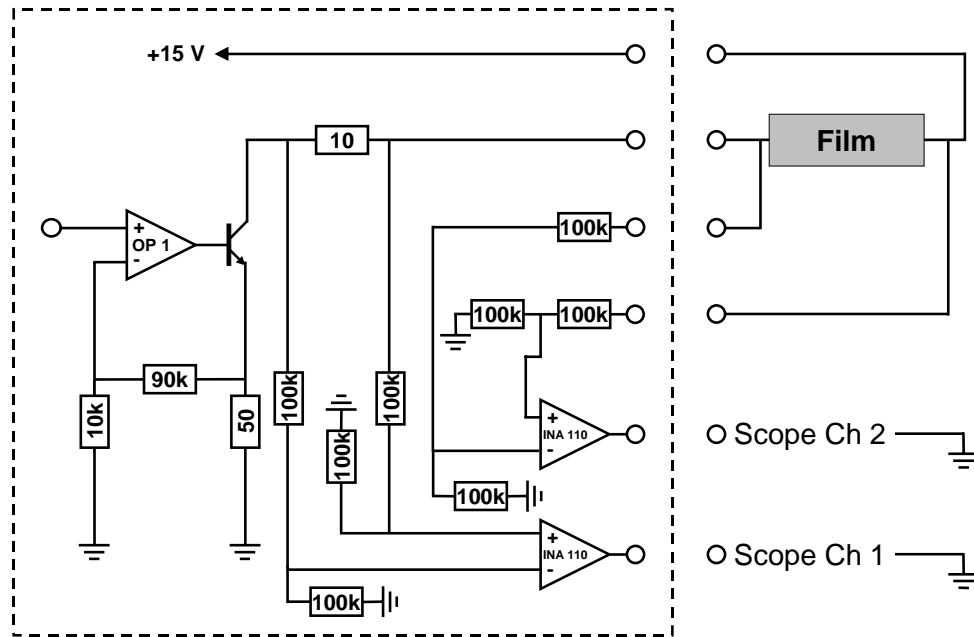
131

Figure C.1:   *Layout of the modified current source used for the generation of current pulses. Compared to the original construction [167], the resistor of the current monitor was changed from 50 Ω to 10 Ω and was connected to the collector side of the transistor.*

current of the transistor disregarded. The second change concerns the installation of two additional voltage dividers that reduce the input signals of the second instrumentation amplifier that processes the voltage drop across the 10 Ω metal-film resistor. This modification was necessary because the input of the INA110 requires voltage that is different to its supply voltage of (±15 V). In the superconducting state of the sample ($T \ll T_c$) this condition in the new configuration only holds if this additional voltage divider is used.

Appendix D

Summary of all irradiated films

Tables D.1 and D.2 summarize the thin films that have been irradiated during this work. All listed samples are still available and can be used for further measurements. In particular the sample Y081 is a good candidate for the realization of pulsed measurements at high current densities (cf. chapter 6). In addition, Fig. D.1 sketches further measurement structures of the irradiated films.

Table D.1: *List of all* $Bi_2Sr_2CaCu_2O_{8+\delta}$ *films irradiated during this work. Apart from the film name, the used ions as well as their corresponding energies (in* MeV/u*) and the used microstructure are quoted. The comments refer to special irradiation features.*

Film	Ion	Energy	Pattern	Dose	Comment
T1-009	^{129}Xe	3.6	D.1.a)	0.5 T	Stripline 4: fully irradiated
					Stripline 2: Microprobe, 65 channels ($w = 10~\mu$m, $d = 20~\mu$m)
T2-009	^{129}Xe	3.6	D.1.b)	0.5 T	1:7 ratio structure as in chapter 4
T2-010	^{129}Xe	3.6	D.1.b)	1.0 T	1:7 ratio structure as in chapter 4
T1-012	^{129}Xe	3.6	D.1.a)	1.0 T	Bridge 2: with C-foil
	^{129}Xe	3.6	D.1.a)	1.0 T	Bridge 3: without C-foil
	^{208}Pb	3.6	D.1.a)	1.0 T	Bridge 4: with C-foil
J1-011	^{208}Pb	3.6	4.3	1.0 T	1:7 ratio irradiation
J2-004	^{208}Pb	3.6	4.3	0.3 T	1:7 ratio irradiation
J2-008	^{208}Pb	3.6	4.3	2.0 T	1:7 ratio irradiation
J3-010	^{238}U	4.8	None	3.0 T	One half irradiated
J3-011	^{238}U	4.8	None	2.0 T	One half irradiated
Bi100800	^{132}Xe	5.9	None	1.0 T	1:4 irradiation
Ak19	^{238}U	11.4	5.1	1.0 T	see chapter 5

Table D.2:   *List of all* $YBa_2Cu_3O_{7-x}$ *films irradiated during this work. Apart from the film name, the used ions as well as their corresponding energies (in MeV/u) and the used microstructure are quoted. The comments refer to special irradiation features.* [1]   *The structure is described in Ref. [21].*

Film	Ion	Energy	Pattern	Dose	Comment
Y-010	^{129}Xe	3.6	D.1.b)	1.0 T	1:7 ratio structure as in chapter 4
Y151098	^{209}Bi	3.6	3.1.b)	0.6 T	fully irradiated
Y121098	^{209}Bi	3.6	3.1.b)	0.6 T	fully irradiated
	^{208}Pb	3.6	3.1.b)	1.0 T	$\Sigma B_\phi = 1.6$ T
	^{238}U	4.8	3.1.b)	1.6 T	$\Sigma B_\phi = 3.0$ T
Y131098	^{208}Pb	3.6	3.1.b)	0.3 T	fully irradiated
Y140199	^{208}Pb	3.6	4.3	1.0 T	1:7 ratio irradiation
Y081	^{238}U	4.8	D.1.a)[1]	1.0 T	Bridge 1 and 2
Y240998	^{238}U	4.8	4.3	1.0 T	1:4 ratio irradiation with left test bridge
Y090198	^{238}U	4.8	None	2.0 T	One half irradiated
Y280700	^{132}Xe	5.9	4.16	1.0 T	Test bridge and micro-probe
Y130199	^{238}U	11.4	5.1	1.0 T	see chapter 5
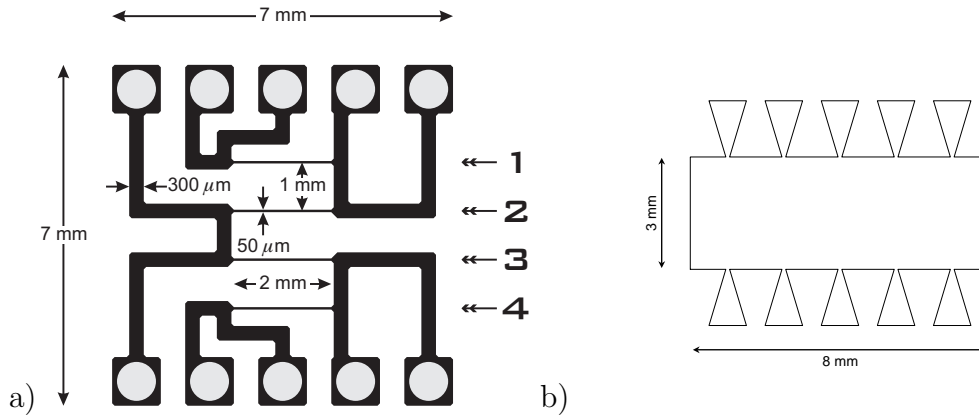
Figure D.1:   a) *Pattern of the films containing four identical microbridges of 2 mm $\times$ 50 μm. The single striplines are differentiated according to the numbering on the right side. b) Hall-structure without test bridges. Both structures were generated on 10×10 mm^2 thin films.*

Bibliography

[1] J. G. Bednorz and K. A. Müller, Z. Phys. B **64**, 189 (1986).

[2] M. K. Wu, J. R. Ashburn, C. J. Torng, P. H. Hor, R. L. Meng, L. Gao, Z. J. Huang, Y. Q. Wang, and C. W. Chu, Phys. Rev. Lett. **58**, 908 (1987).

[3] H. Maeda, Y. Tanaka, M. Fukutomi, and T. Asano, Jpn. J. Appl. Phys. **27**, L209 (1988).

[4] M. P. A. Fisher, Phys. Rev. Lett. **62**, 1415 (1989).

[5] D. S. Fisher, M. P. A. Fisher, and D. A. Huse, Phys. Rev. B **43**, 130 (1991).

[6] K. Harada, O. Kamimura, H. Kasai, T. Matsuda, A. Tonomura, and V. V. Moshchalkov, Science **274**, 1167 (1996).

[7] L. Civale, Supercond. Sci. Technol. **10**, A11 (1997).

[8] G. Wirth, F. Hillmer, G. Jakob, E. Jäger, E. Schimpf, and H. Adrain, Nucl. Instrum. Methods B **146**, 581 (1998).

[9] F. Hillmer, G. Jakob, P. Haibach, U. Frey, T. Kluge, H. Adrain, G. Wirth, E. Jäger, and E. Schimpf, Physica C **311**, 11 (1999).

[10] J. R. Clem, Phys. Rev. B **43**, 7837 (1991).

[11] D. R. Nelson and M. V. Vinokur, Phys. Rev. Lett. **68**, 2398 (1992).

[12] P. Voss-de Haan, G. Jakob, and H. Adrian, Phys. Rev. B **60**, 12 443 (1999).

[13] M. C. Marchetti and D. R. Nelson, Phys. Rev. B **59**, 13 624 (1999).

[14] J. Nagamatsu, N. Nakagawa, T. Muranaka, Y. Zenitani, and J. Akimitsu, Nature (London) **410**, 63 (2001).

[15] M. Tinkham, *Introduction to Superconductivity*, 2nd ed. (McGraw-Hill International Press, New York, 1996).

[16] A. I. Larkin and Y. M. Ovchinnikov, J. Low Temp. Phys. **34**, 409 (1979).

[17] P. W. Anderson, Phys. Rev. Lett. **9**, 309 (1962).

[18] P. W. Anderson and Y. B. Kim, Rev. Mod. Phys. **36**, 39 (1964).

[19] G. Blatter, M. V. Feigel'man, V. B. Geshkenbein, A. I. Larkin, and V. M. Vinokur, Rev. Mod. Phys. **66**, 1125 (1994).

[20] P. H. Kes, J. Aarts, J. van den Berg, C. J. van der Beek, and J. Mydosh, Supercond. Sci. Technol. **1**, 242 (1989).

[21] P. Voss-de Haan, Ph.D. thesis, Johannes Gutenberg-Universität Mainz, 1999.

[22] K. Binder and A. P. Young, Rev. Mod. Phys. **58**, 801 (1986).

[23] S. A. Wolf, D. U. Gubser, and Y. Imry, Phys. Rev. Lett. **42**, 324 (1979).

[24] R. H. Koch, V. Foglietti, W. J. Gallagher, G. Koren, A. Gupta, and M. P. A. Fisher, Phys. Rev. Lett. **63**, 1511 (1989).

[25] J. Kötzler, M. Kaufmann, G. Nakielski, R. Behr, and W. Assmus, Phys. Rev. Lett. **72**, 2081 (1994), and references therein.

[26] P. L. Gammel, L. F. Schneemeyer, and D. J. Bishop, Phys. Rev. Lett. **66**, 953 (1991).

[27] M. Charlambous, R. H. Koch, T. Masselink, T. Doany, C. Feild, and F. Holtzberg, Phys. Rev. Lett. **75**, 2578 (1995).

[28] D. R. Strachan, M. C. Sullivan, P. Fournier, S. P. Pai, T. Venkatesan, and C. J. Lobb, Phys. Rev. Lett. **87**, 067007 (2001).

[29] R. Griessen, Phys. Rev. Lett. **64**, 1674 (1990).

[30] E. Zeldov, N. M. Amer, G. Koren, A. Gupta, and M. W. McElfresh, Appl. Phys. Lett. **56**, 7742 (1990).

[31] H. J. Jensen and P. Minnhagen, Phys. Rev. Lett. **66**, 1630 (1991).

[32] D. R. Nelson and M. V. Vinokur, Phys. Rev. B **48**, 13 060 (1993).

[33] D. R. Nelson and M. V. Vinokur, Phys. Rev. B **61**, 5917 (2000).

[34] B. Dam, J. M. Huijbregtse, F. C. Klaassen, R. C. F. van der Geest, G. Doornbos, J. H. Rector, A. M. Testa, S. Freisem, J. C. Martínez, B. Stäuble-Pümpin, and R. Griessen, Nature (London) **399**, 439 (1999).

[35] J. Wiesner, C. Træholt, J.-G. Wen, H.-W. Zandbergen, G. Wirth, and H. Fuess, Physica C **268**, 161 (1996).

[36] D. R. Nelson, Phys. Rev. Lett. **60**, 1973 (1988).

[37] R. P. Feynman and A. R. Hibbs, *Quantum Mechanics and Path Integrals* (McGraw-Hill, New York, 1965).

[38] M. P. A. Fisher, P. B. Weichman, G. Grinstein, and D. S. Fisher, Phys. Rev. B **40**, 546 (1989).

[39] E. H. Brandt, Phys. Rev. Lett. **69**, 1105 (1992).

[40] B. I. Shklovskii and A. L. Efros, *Electronic Properties of Doped Semiconductors* (Spinger, New York, 1984).

[41] M. V. Feigel'man, V. B. Geshkenbein, A. I. Larkin, and V. M. Vinokur, Phys. Rev. Lett. **63**, 2303 (1989).

[42] W. Krauth, T. Trivedi, and D. Ceperley, Phys. Rev. Lett. **67**, 2307 (1991).

[43] E. S. Sørensen, M. Wallin, S. M. Girvin, and A. P. Young, Phys. Rev. Lett. **69**, 828 (1992).

[44] M. Wallin, E. S. Sørensen, S. M. Girvin, and A. P. Young, Phys. Rev. B **49**, 12 115 (1994).

[45] H. Safar, P. L. Gammel, D. J. Bishop, D. B. Mitzi, and A. Kapitulnik, Phys. Rev. Lett. **68**, 2672 (1992).

[46] J. Deak, M. J. Darwin, and M. McElfresh, Physica A **200**, 332 (1993).

[47] D. G. Xenikos, J.-T. Kim, and T. R. Lemberger, Phys. Rev. B **48**, 680 (1993).

[48] P. G. Debenedetti and F. H. Stilliger, Nature (London) **410**, 259 (2001).

[49] F. Hillmer, Ph.D. thesis, Johannes Gutenberg-Universität Mainz, 1999.

[50] M. Tachiki and S. Takahashi, Solid State Commun. **70**, 291 (1989).

[51] M. Tachiki and S. Takahashi, Solid State Commun. **72**, 1083 (1989).

[52] T. Koyama, N. Takezawa, and M. Tachiki, Physica C **172**, 501 (1991).

[53] A. Pruymboom, P. Kes, E. van der Drift, and S. Radelaar, Phys. Rev. Lett. **60**, 1430 (1988).

[54] H. Pastoriza and P. H. Kes, Phys. Rev. Lett. **75**, 3525 (1995).

[55] M. C. Marchetti and D. R. Nelson, Physica C **330**, 105 (2000).

[56] C. Gerthsen and H. Vogel, *Physik*, 17th ed. (Springer-Verlag, Berlin, 1993).

[57] D. López, W. K. Kwok, H. Safar, R. J. Olsson, A. M. Petrean, L. Paulius, and G. W. Crabtree, Phys. Rev. Lett. **82**, 1277 (1999).

[58] Y. Eltsev, K. Nakao, S. Shibata, and N. Koshizuka, *Advances in Super-conductivity* (Proceedings of the 12th ISS'99, Oct. 17-19, Morioka, 1999), Vol. 12, p. 317.

[59] T. Hwa, P. Le Doussal, D. R. Nelson, and V. M. Vinokur, Phys. Rev. Lett. **711**, 3545 (1993).

[60] L. Krusin-Elbaum, G. Blatter, J. R. Thompson, D. K. Petrov, R. Wheeler, J. Ullmann, and C. W. Chu, Phys. Rev. Lett. **81**, 3948 (1998).

[61] H. Frey and G. Kienel, *Dünnschichttechnologie* (VDI-Verlag, Düsseldorf, 1987).

[62] M. Basset, Master's thesis, Johannes Gutenberg-Universität Mainz, 1998.

[63] P. Haibach, J. Köble, M. Huth, and H. Adrian, Thin Solid Films **336**, 168 (1999).

[64] G. Jakob, Ph.D. thesis, TH Darmstadt, 1993.

[65] P. Wagner, Ph.D. thesis, TH Darmstadt, 1993.

[66] U. Frey, Master's thesis, TH Darmstadt, 1994.

[67] C. Tomé-Rosa, G. Jakob, M. Maul, A. Walkenhorst, M. Schmitt, P. Wagner, P. Przyslupski, and H. Adrian, Physica C **171**, 230 (1990).

[68] P. Wagner, F. Hillmer, U. Frey, H. Adrian, T. Steinborn, L. Ranno, A. Elscher, I. Heyvaert, and Y. Bruynserade, Physica C **215**, 123 (1993).

[69] T. Steinborn, Ph.D. thesis, TH Darmstadt, 1994.

[70] M. Kraus, M. Leghissa, and G. Saemann-Ischenko, Phys. Bl. **50**, 333 (1994).

[71] J. P. Biersack and L. G. Haggmark, Nucl. Instrum. Methods B **174**, 257 (1980).

[72] J. F. Ziegler, J. P. Biersack, and U. Littmark, *The Stopping and Range of Ions in Solids* (Pergamon Press, New York, 1985).

[73] G. Kraft, U. Arndt, W. Becher, D. Schardt, H. Stelzer, U. Weber, and T. Archinal, Nucl. Instr. and Meth. in Phys. Res. A **367**, 66 (1995), and references therein.

[74] B. E. Fischer and R. Spohr, Rev. Mod. Phys. **55**, 970 (1983).

[75] S. Klaumünzer, Ming-dong Hou, and G. Schumacher, Phys. Rev. Lett. **57**, 850 (1986).

[76] R. L. Fleischer, P. B. Price, and R. M. Walker, J. Appl. Phys. **36**, 3645 (1965).

[77] Y. Zhu, Z. X. Cai, R. C. Budhani, M. Suenaga, and D. O. Welch, Phys. Rev. B **48**, 6436 (1993).

[78] D. Bourgault, M. Hervieu, S. Bouffard, D. Groult, and B. Raveau, Nucl. Instr. and Meth. in Phys. Res. B **42**, 61 (1989).

[79] H. Watanabe, B. Kabius, K. Urban, B. Roas, S. Klaumünzer, and G. Saemann-Ischenko, Physica C **179**, 75 (1991).

[80] R. W. Müller, *Das UNILAC-Projekt* (GSI-Bericht 72-9, Gesellschaft für Schwerionenforschung, Darmstadt, 1972).

[81] More information about the accelerator properties, including JAVA animations is available at *http://www.gsi.de/gsi.accelerator.html*.

[82] A detailed description of the development of the HLI in 1999 is found in *GSI Scientific Report*, 173–186, 2000.

[83] W. Barth, in *XXth International Linac Conference* (Proceedings of LINAC2000, Monterrey, 2000), p. 1033.

[84] J. Wiesner, Ph.D. thesis, TH Darmstadt, 1994.

[85] M. Schlögl, Master's thesis, Johann Wolfgang von Goethe-Universität Frankfurt, 2001.

[86] Some of these images are available at *http://www-wnt.gsi.de/mr/micro_pattern.htm* .

[87] U. Frey, Ph.D. thesis, Johannes Gutenberg-Universität Mainz, 1998.

[88] D. Bourgault, S. Bouffard, M. Toulmeonde, D. Groult, J. Provost, F. Studer, N. Nguyen, and B. Raveau, Phys. Rev. B **39**, 6549 (1989).

[89] B. Roas, B. Hensel, S. Henke, S. Klaumünzer, B. Kabius, W. Watanabe, G. Saemann-Ischenko, L. Schultz, and K. Urban, Europhys. Lett. **11**, 669 (1990).

[90] B. Hensel, B. Roas, S. Henke, R. Hopfengärtner, M. Lippert, J. P. Ströbel, M. Vildić, G. Saemann-Ischenko, and S. Klaumünzer, Phys. Rev. B **42**, 4135 (1990).

[91] F. Rullier-Albenque, A. Legris, S. Bouffard, E. Paumier, and P. Lejay, Physica C **175**, 111 (1991).

[92] H. Frank, J. Lethen, L. Buschmann, B. Decker, J. Wiesner, G. Wirth, P. Wagner, H. Adrian, P. Lemmens, and G. Güntherodt, Physica C **259**, 142 (1996).

[93] A. Pomar, Z. Konstantinovic, L. Martel, Z. Z. Li, and H. Raffy, Phys. Rev. Lett. **85**, 2809 (2000).

[94] W.-K. Chu, J. R. Liu, and Z. H. Zhang, Nucl. Instrum. Methods B **59/60**, 1447 (1991), and references therein.

[95] S. I. Woods, A. S. Katz, M. C. de Andrade, J. Herrmann, M. B. Maple, and R. C. Dynes, Phys. Rev. B **58**, 8800 (1998).

[96] C. Houpert, M. Hervieu, D. Groult, F. Studer, and M. Toulemonde, Nucl. Instrum. Methods B **32**, 393 (1988).

[97] T. T. Palstra, B. Batlogg, L. F. Schneemeyer, and J. V. Waszczak, Phys. Rev. B **43**, 3756 (1991).

[98] C. Tomé-Rosa, Ph.D. thesis, TH Darmstadt, 1992.

[99] V. B. Geshkenbein, M. V. Feigel'man, A. I. Larkin, and V. M. Vinokur, Physica C **162-164**, 239 (1989).

[100] C. Goupil, A. Ruyter, V. Hardy, and C. Simon, Physica C **278**, 23 (1997).

[101] M. Wallin and S. M. Girvin, Phys. Rev. B **47**, 14 642 (1993).

[102] S. A. Grigera, E. Morré, E. Osquiguil, G. Nieva, and F. de la Cruz, Phys. Rev. Lett. **81**, 2348 (1998).

[103] W. K. Kwok, R. J. Olsson, G. Karapetrov, L. M. Paulius, W. G. Moulton, D. J. Hofman, and G. W. Crabtree, Phys. Rev. Lett. **84**, 3706 (2000).

[104] G. L. Bhalla and U. Divakar, Physica C **355**, 103 (2001).

[105] U. Divakar and G. L. Bhalla, Physica C **355**, 341 (2001).

[106] T. Sueyoshi, N. Ishikawa, A. Iwase, Y. Chimi, T. Kiss, T. Fujiyoshi, and M. Miyahara, Physica C **309**, 79 (1998).

[107] P. J. M. Wöltgens, C. Dekker, R. H. Koch, B. W. Hussey, and A. Gupta, Phys. Rev. B **52**, 4536 (1995).

[108] L. Radzihovsky, Phys. Rev. Lett. **74**, 4923 (1995).

[109] K. M. Beauchamp, T. F. Rosenbaum, U. Welp, G. W. Crabtree, and V. M. Vinokur, Phys. Rev. Lett. **75**, 3942 (1995).

[110] A. Sawa, H. Yamasaki, Y. Mawatari, H. Obara, M. Umeda, and S. Kosaka, Phys. Rev. B **58**, 2868 (1998).

[111] S. N. Coppersmith, M. Inui, and P. B. Littlewood, Phys. Rev. Lett. **64**, 2585 (1990).

[112] H. H. Wen, X. X. Yao, R. L. Wang, H. C. Li, S. Q. Guo, and Z. X. Zhao, Physica C **282-287**, 351 (1997).

[113] P. Minnhagen, B. J. Kim, and H. Weber, Phys. Rev. Lett. **87**, 037002 (2001).

[114] M. Tinkham, Phys. Rev. Lett. **61**, 1658 (1988).

[115] L. Civale, A. D. Marwick, T. K. Worthington, M. A. Kirk, J. R. Thompson, L. Krusin-Elbaum, Y. Sun, J. R. Clem, and F. Holtzberg, Phys. Rev. Lett. **67**, 648 (1991).

[116] A. I. Larkin and V. M. Vinokur, Phys. Rev. Lett. **75**, 4666 (1995).

[117] Y. Yeshurun and A. P. Malozemoff, Phys. Rev. Lett. **60**, 2202 (1988).

[118] L. Krusin-Elbaum, L. Civale, G. Blatter, A. D. Marwick, F. Holtzberg, and C. Feild, Phys. Rev. Lett. **72**, 1914 (1994).

[119] L. Civale and L. Krusin-Elbaum, Phys. Rev. Lett. **78**, 1829 (1997).

[120] L. Miu, T. Noji, Y. Koike, E. Cimpoiasu, and C. C. Almasan, Phys. Rev. B **62**, 15 172 (2000).

[121] L. Miu, M. Basset, H. Rodriguez, G. Jakob, and H. Adrian, (accepted for publication in Phys. Rev. **B**).

[122] T. Nattermann, Phys. Rev. Lett. **64**, 2454 (1990).

[123] T. Giamarchi and P. Le Doussal, Phys. Rev. Lett. **72**, 1530 (1994).

[124] B. Maiorov and E. Osquiguil, Phys. Rev. B **64**, 052511 (2001).

[125] S. Fleshler, W. K. Kwok, U. Welp, V. M. Vinokur, M. K. Smith, J. Downey, and G. W. Crabtree, Phys. Rev. B **47**, 14 448 (1993).

[126] A. A. Prodan, V. A. Shklovskij, V. V. Chabanenko, A. V. Bondarenko, M. A. Obolenskii, H. Szymczak, and S. Piechota, Physica C **302**, 271 (1998).

[127] H. Pastoriza, S. Candia, and G. Nieva, Phys. Rev. Lett. **83**, 1026 (1999).

[128] V. V. Chabanenko, A. A. Prodan, V. A. Shklovskij, A. V. Bondarenko, M. A. Obolenskii, H. Szymczak, and S. Piechota, Physica C **314**, 133 (1999).

[129] G. D'Anna, V. Berseth, L. Forró, A. Erb, and E. Walker, Phys. Rev. B **61**, 4215 (2000).

[130] V. Berseth, Ph.D. thesis, École Polytechnique Fédérale, Lausanne, 1999.

[131] G. A. Jorge and E. Rodríguez, Phys. Rev. B **61**, 103 (2000).

[132] J. A. Herbsommer, G. Nieva, and L. Luzuriaga, Phys. Rev. B **61**, 11 745 (2000).

[133] G. W. Crabtree, G. K. Leaf, H. G. Kaper, V. M. Vinokur, A. E. Koshelev, D. W. Braun, D. M. Levine, W. K. Kwok, and J. A. Fendich, Physica C **263**, 401 (1996).

[134] E. B. Sonin, Phys. Rev. B **48**, 10 487 (1993).

[135] E. B. Sonin, Phys. Rev. B **55**, 485 (1997).

[136] Y. Mawatari, Phys. Rev. B **56**, 3433 (1997).

[137] Y. Mawatari, Phys. Rev. B **59**, 12 033 (1999).

[138] V. A. Shklovskij, A. K. Soroka, and A. A. Soroka, Sov. Phys. JETP **89**, 1138 (1999).

[139] A. K. Niessen and C. H. Weijsenfeld, J. Appl. Phys. **40**, 384 (1969).

[140] M. C. Marchetti and D. R. Nelson, Phys. Rev. B **42**, 9338 (1990).

[141] A. K. Soroka, M. Huth, J. Oster, V. A. Shklovskij, and H. Adrian, to be published.

[142] E. B. Sonin and A. L. Kholkin, Sov. Phys. Solid State **34**, 610 (1992).

[143] V. A. Shklovskij, Low Temp. Phys. **23**, 853 (1997).

[144] T. R. Chien, T. W. Jing, N. P. Ong, and Z. Z. Wang, Phys. Rev. Lett. **66**, 3075 (1991).

[145] D. R. Nelson and B. I. Halperin, Phys. Rev. B **19**, 2457 (1979).

[146] E. van der Drift, S. Radelaar, A. Pruymboom, and P. Kes, J. Vac. Sci. Technol. B **6**, 297 (1988).

[147] M. H. Theunissen, E. V. der Drift, and P. H. Kes, Phys. Rev. Lett. **77**, 159 (1996).

[148] L. Miu, P. Wagner, A. Hadish, F. Hillmer, H. Adrian, J. Wiesner, and G. Wirth, Phys. Rev. B **51**, 3953 (1995).

[149] T. K. Worthington, F. H. Holtzberg, and C. A. Feild, Cryogenics **30**, 417 (1990).

[150] A. Rydh and O. Rapp, Phys. Rev. Lett. **86**, 1873 (2001).

[151] D. E. Farrell, S. Bonham, J. Foster, V. C. Chang, P. Z. Jiang, K. G. Vandervoort, D. J. Lam, and V. G. Kogan, Phys. Rev. Lett. **63**, 782 (1989).

[152] P. Olsson and S. Teitel, Phys. Rev. Lett. **82**, 2183 (1999).

[153] A. I. Larkin and Y. M. Ovchinnikov, Sov. Phys. JETP **41**, 960 (1975).

[154] P. Voss-de Haan, G. Jakob, M. Basset, Z. Xiao, and H. Adrian, in *Superconducting and Related Oxides: Physics and Nanoengeneering IV*, edited by D. Pavuna and I. Bozov (Proceedings of SPIE, Orlando, 2000), Vol. 4058, p. 110.

[155] L. E. Musienko, I. M. Dmitrenko, and V. G. Volotskaya, JETP Lett. **31**, 567 (1980).

[156] W. Klein, R. P. Huebner, S. Gauss, and J. Parisi, J. Low Temp. Phys. **61**, 413 (1985).

[157] A. V. Samiolov, M. Konczykowski, N. Yeh, S. Berry, and C. C. Tsuei, Phys. Rev. Lett. **75**, 4118 (1995).

[158] B. J. Ruck, J. C. Abele, H. J. Trodahl, S. A. Brown, and P. Lynam, Phys. Rev. Lett. **78**, 3378 (1997).

[159] S. G. Doettinger, R. P. Huebner, R. Gerdemann, A. Kühle, A. Anders, T. G. Täuble, and J. C. Villégier, Phys. Rev. Lett. **73**, 1691 (1994).

[160] Z. L. Xiao and P. Ziemann, Phys. Rev. B **53**, 15 265 (1996).

[161] S. G. Doettinger, R. P. Huebner, and A. Kühle, Physica C **251**, 285 (1995).

[162] Z. L. Xiao, P. Voss-de Haan, G. Jakob, and H. Adrian, Phys. Rev. B **57**, R736 (1998).

[163] Z. L. Xiao, P. Voss-de Haan, G. Jakob, T. Kluge, P. Haibach, H. Adrian, and E. Y. Andrei, Phys. Rev. B **59**, 1481 (1999).

[164] A. I. Bezuglyi and V. A. Shkllovskij, Physica C **202**, 234 (1992).

[165] M. N. Kunchur, D. K. Christen, and J. M. Phillips, Phys. Rev. Lett. **70**, 998 (1993).

[166] M. N. Kunchur, Mod. Phys. Lett. B **9**, 399 (1995).

[167] M. Wagner, Master's thesis, Johannes Gutenberg-Universität Mainz, 1998.

[168] V. A. Shklovskij, private communication.

[169] S. Zeuner, H. Lengfellner, and W. Prettl, Phys. Rev. B **51**, 11 903 (1995).

[170] M. Nahum, S. Verghese, P. L. Richards, and K. Char, Appl. Phys. Lett. **59**, 2034 (1991).

[171] M. S. Carslaw and J. C. Jaeger, *Conduction of Heat in Solids*, 2nd ed. (Oxford University Press, London, 1959).

[172] G. L. Carr, M. Quijada, D. B. Tanner, C. J. Hirschmugl, G. P. W. S. Etemad, B. Dutta, F. DeRosa, A. Inam, T. Venkatesan, and X. Xi, Appl. Phys. Lett. **57**, 2725 (1990).

[173] C. D. Marshall, I. M. Fishman, R. C. Dorfmann, C. B. Eom, and M. D. Fayer, Phys. Rev. B **45**, 10 009 (2000).

[174] S. Zeuner, H. Lengfellner, J. Betz, K. F. Renk, and W. Prettl, Appl. Phys. Lett. **61**, 973 (1992).

[175] A. D. Semenov, I. G. Gogidze, G. N. Gol'tsman, A. V. Sergeev, and E. M. Gershenzon, Appl. Phys. Lett. **63**, 681 (1993).

[176] A. V. Sergeev, A. D. Semenov, P. Kouminov, V. Trifonov, I. G. Gogidze, B. S. Karasik, G. N. Gol'tsman, and E. M. Gershenzon, Phys. Rev. B **49**, 9091 (1994).

[177] Y. S. Touloukian, R. W. Powell, C. Y. Ho, and P. G. Klemens, *Thermophysical Properties of Matter* (IFI/Plenum, New York, 1970), Vol. 2.

[178] M. N. Kunchur, D. K. Christen, C. E. Klabunde, and J. M. Phillips, Phys. Rev. Lett. **72**, 752 (1994).

[179] D. H. Lee, R. R. H. amd D. A. Kiewit, and O. J. Marsh, Phys. Stat. Sol. **15a**, 645 (1973).

[180] W. F. Van der Weg, D. Sigurd, and J. W. Mayer, in *Applications of Ion Beams to Metals*, edited by S. T. Picraux (Plenum Press, New York, 1974), p. 209.

[181] W. Bolse, in *International Conference on Beam Processing of Advanced Materials* (ASM Materials Congress, Cleveland, Ohio, 1995), Vol. 4058.

[182] W. Bolse, Mat. Sci. Eng. A **253**, 194 (1998), and references therein.

[183] W. K. Chu, J. W. Mayer, and M. A. Nicolet, *Backscattering Spectrometry* (Academic Press, Orlando, 1978).

[184] T. Hahn, Master's thesis, TH Darmstadt, 1992.

[185] K. Üstüner, Master's thesis, Johannes Gutenberg-Universität Mainz, 1996.

[186] M. Maier, Ph.D. thesis, Johannes Gutenberg-Universität Mainz, 2001.

List of Publications

Transport properties and lower critical field of $Bi_2Sr_2Ca_2Cu_3O_{10+\delta}$ Josephson junctions
U. Frey, M. Blumers, M. Basset, J.C. Martínez, and H. Adrian
Proceedings of the 3rd EUropean Conference on Applied Superconductivity 1997, Twente, the Netherlands
Inst. Phys. Conf. Ser. No **158**, 563–566 (1997).

Josephson junctions and superconducting field effect transistors based on epitaxial $Bi_2Sr_2Ca_{n-1}Cu_nO_{2(n+2)}$ thin films
U. Frey, M. Basset, K.Üstüner, M. Blumers, Ch. Schwan, J.C. Martínez, and H. Adrian
Applied Superconductivity **6**, 429-436 (1998).

$Bi_2Sr_2CaCu_2O_{8+\delta}$ epitaxial thin films on silicon substrates
S. Ingebrandt, J.C. Martínez, M. Basset, M. Mauer, M. Maier, H. Adrian, S. Linzen and P. Seidel
Proceedings of the 4th European Conference on Applied Superconductivity 1999, Barcelona, Spain
Inst. Phys. Conf. Ser. No **167**, 21–24 (1999).

Einfluß kolumnarer defekte auf die Transporteigenschaften epitaktischer Hochtemperatur-Supraleiter Dünnfilme
M. Basset, G. Jakob, F. Hillmer, G. Wirth, and H. Adrian
Proceedings of the meeting "Forschung mit nuklearen Sonden und Ionenstrahlen" 1999, Berlin, Germany
HMI-B, 44–45 (1999).

Heavy ion induced anisotropic pinning force in high-temperature superconducting thin films
M. Basset, G. Jakob, G. Wirth, E. Jäger, E. Schimpf, and H. Adrian
GSI Scientific Report 1999, 146 (2000).

Vortex instability and vortex-glass transition in $Bi_2Sr_2CaCu_2O_{8+\delta}$ and $YBa_2Cu_3O_{7-x}$ thin films
P. Voss-de Haan, G. Jakob, M. Basset, Z. Xiao and H. Adrian
in *Superconducting and Related Oxides: Physics and Nano-Engeneering IV*
ed. D. Pavuna and I. Bozovic, Proc. SPIE **4058**, 110–118, Orlando,
Florida USA (2000).

Influence of heavy ion induced columnar defects on the vortex dynamics of high-temperature superconductors
M. Basset, G. Jakob, G. Wirth, B.E. Fischer, P. Voss-de Haan,
E. Jäger, and H. Adrian
GSI Scientific Report 2000, 138 (2001).

Patterned irradiation of $YBa_2Cu_3O_{7-x}$ thin films
M. Basset, G. Jakob, G. Wirth, and H. Adrian
Phys. Rev. B **64**, 024525 (2001).

Non-diverging vortex pinning barriers at low current densities across the putative elastic vortex glass – vortex liquid transition in $YBa_2Cu_3O_{7-x}$ films
L. Miu, M. Basset, G. Jakob, H. Rodriguez, and H. Adrian
Phys. Rev. B **64**, 220502(R) (2001).

Danksagung (Acknowledgements)

Einige der in dieser Arbeit untersuchten $YBa_2Cu_3O_{7-x}$ und $Bi_2Sr_2CaCu_2O_{8+\delta}$ Filme wurden von Herrn Dipl.-Phys. H. R. und Herrn Dipl.-Phys. A. S. zur Verfügung gestellt, wofür ich mich an dieser Stelle bedanken möchte.

Ein herzliches Dankeschön dafür, dass ich von ihrem großen Erfahrungsschatz profitieren durfte, geht an Herrn HD Dr. M. H., Herrn Dr. J.-C. M., Herrn Dr. P. V. und Herrn Dr. M. J.

Durch viele fruchtbare Diskussionen während ihrer Forschungsaufenthalte in Mainz hat die vorliegende Arbeit an Qualität gewonnen, wofür ich Herrn Dr. L. M. und Herrn Prof. Dr. V. A. S. danken möchte.

Herrn Dipl.-Ing. J. H. danke ich für seine fortwährende Unterstützung bei einer Vielzahl von technischen Fragen und Problemen sowie Frau A. D. für die Anfertigung unzähliger REM und AFM Aufnahmen.

Eine hervorragende Versorgung mit dem für die Experimente so wichtigen flüssigem Helium verdanke ich dem großen Engagement von Herrn G. und Herrn G.

Bei Frau K. bedanke ich mich für die Anfertigung zahlreicher Lithographiemasken und bei Herrn J. S. für das Vorbereiten vieler Targets.

Ohne die präzise und schnelle Ausfhrung der vielen Aufträge wäre die Durchführung vieler Experimente sicher nicht möglich gewesen. Stellvertretend für die Mitarbeiter der mechanischen Werkstatt möchte ich Herrn H. L. besonders danken, der die Metallmasken für die strukturierten Bestrahlungen mit sehr viel Mühe angefertigt hat.

Allen nicht namentlich erwähnten aktuellen und ehemaligen Mitgliedern des Arbeitkreises danke ich an dieser Stelle ganz herzlich. Das gute Klima in der Arbeitsgruppe hat wesentlich zum Gelingen dieser Arbeit beigetragen. In den vergangenen fünf Jahren hat es mit Euch allen zusammen sehr viel Spaß gemacht!

Schließlich möchte ich mich ganz herzlich bei meinen Eltern, die mir diese Ausbildung erst ermöglicht haben, sowie bei meiner Freundin für ihre ständige Unterstützung und das Interesse am Fortgang dieser Arbeit bedanken. Auch in schwierigen Phasen habe ich bei ihnen einen starken Rückhalt gefunden.

Curriculum Vitae

Personal data:

Name:	Michael Basset
Date of birth:	January 6, 1971
Place of birth:	Nastätten (Germany)
Nationality:	German

School education:

1977 – 1981	Primary-school in Lorch
1981 – 1991	Rheingauschule (Gymnasium) in Geisenheim
Sep. 1988 – Jun. 1989	Lycée Jean-Perrin in Lyon, France
June 1991	Abitur (school leaving exam and university entrance qualification)

Military service:

Jul. 1991 – Sep. 1992	Compulsory military service

Study of physics:

October 1992	Inscription in the department of physics at the Johannes Gutenberg-University Mainz
August 1994	Intermediate diploma
Apr. 1997 – Sep. 1998	Diploma work at the institute of Physics, supervised by Prof. Dr. H. Adrian, *'Electric Field Effect on Ultrathin $Bi_2Sr_2CaCu_2O_{8+\delta}$ Films'*
September 1998	Diploma in physics
October 1998	Beginning of Ph.D. research as academic employee at the institute of physics of the Johannes Gutenberg-University Mainz